Regulation of Motor Axon Innervation at the Neuromuscular Junction

by

Jennifer L. Shadrach

A dissertation submitted in partial fulfillment
of the requirements for the degree of
Doctor of Philosophy
(Cellular and Molecular Biology)
in the University of Michigan
2017

Doctoral Committee:

Associate Professor Brian A. Pierchala, Chair
Associate Professor Anthony Antonellis
Professor Susan V. Brooks
Professor Roman J. Giger
Professor Daniel Goldman

Jennifer L. Shadrach

jenshad@umich.edu

ORCID iD: 0000-0001-5266-8625

ACKNOWLEDGEMENTS:

First, I would like to thank Dr. Brian Pierchala for the opportunity to work in your laboratory. I have benefited greatly from your guidance and support over the past five years. Additionally, I appreciate your willingness in allowing me to explore my scientific interests and develop into an independent researcher. What I have learned from my experiences will be extremely valuable as I pursue my future scientific career.

I would also like to thank the entire Pierchala lab for their help and insights over the years. In particular, I would like thank Allison Milan for her technical assistance throughout this past year. Finally, a special thanks to Chris Donnelly – without both your scientific input and friendship over the years my graduate school experience would have not been the same.

To my committee members, thank you for your time, wisdom, and guidance throughout my graduate training. Your thoughtful comments and advice, as well as your willingness to share various protocols and reagents have been greatly appreciated.

Finally, I would like to thank the Cellular and Molecular Biology Program and all my friends and colleagues for supporting me throughout graduate school career.

TABLE OF CONTENTS

LIST OF TABLES

LIST OF FIGURES

ABSTRACT

Coordinated motor function is achieved by proper communication between motor neurons and muscle fibers at a specialized synapse called the neuromuscular junction (NMJ). Throughout life the maintenance of the NMJ is an active process that requires the coordinated function of three main players: the presynaptic motor neuron terminal, the postsynaptic muscle fiber, and terminal Schwann cells (TSCs). Both traumatic injury and neurodegenerative diseases, such as amyotrophic lateral sclerosis (ALS), can result in acute or chronic NMJ denervation, respectively. Under these conditions denervation triggers a regenerative response in which motor nerve terminals are stimulated to grow and undergo axonal sprouting as they reinnervate muscle fibers.

Previous studies have suggested that reestablishment of neuromuscular connections is mediated by various axonal guidance molecules, of which Semaphorin3A (Sema3A) may be of particular importance. Sema3A is a secreted glycoprotein that binds to a plexinA-neuropilin-1 receptor complex to initiate a downstream signaling cascade that induces axonal repulsion. Interestingly, *Sema3A* mRNA upregulation at the NMJ has been hypothesized to create an inhibitory environment that limits axonal sprouting and dampens regeneration. However, a functional role for Sema3A at the NMJ has not been fully elucidated.

Here, we established a quantitative and robust *in vivo* nerve crush model to examine NMJ reinnervation. Using this model, we examined how the ubiquitous loss of Sema3A or

Npn1 impacts regeneration of the adult NMJ. Despite efficient deletion, disruption of Sema3A-Npn1 signaling had no detectable effect on NMJ reinnervation after injury. Thus, the utility of targeting this pathway may offer more limited therapeutic potential than suggested by earlier studies. To identify other promising signaling pathways involved in nerve regeneration, we developed a rapid and unbiased method to isolate motor neuron specific transcripts from complex tissues *in vivo*. Using the RiboTag transgenic mouse model, we show that ribosomal complexes and their associated mRNA transcripts can be specifically isolated from motor neurons and analyzed to detect changes in motor neurons gene expression following injury and during neurodegeneration. Coupling this technique with RNA-seq we anticipate that this work will guide the identification and development of novel therapeutic strategies to treat traumatic nerve injury and neurodegeneration.

CHAPTER 1: INTRODUCTION

The Neuromuscular System

The production of complex and coordinated movements is governed by the neuromuscular system, which acts as a reflex arc coordinating incoming sensory information with the proper motor output. While the principles that govern sensory function have been discussed elsewhere (Lallemend and Ernfors, 2012), here we focus specifically on the motor output of the neuromuscular system. Contraction of skeletal muscle fibers generate force, forming the biological basis for movement. This is achieved when somatic motor neurons in the spinal cord receive input from higher order structures and are sufficiently depolarized to generate an action potential. That action potential then propagates down the motor neuron axon and results in the release of acetylcholine (ACh) from the axon terminal at the neuromuscular junction (NMJ). ACh within the synaptic cleft then binds to ACh receptors (AChRs) on the postsynaptic membrane of the skeletal muscle fiber, triggering depolarization of the muscle cell and resulting in fiber contraction.

The smallest building block of the neuromuscular system is defined as a motor unit. These are comprised of a single motor neuron and all the muscle fibers it innervates. The size of individual motor units can vary greatly, but there is a strong correlation with muscle mass. For example, a motor unit within a large muscle such as those in the thigh, can be composed of thousands of individual muscle fibers.

Conversely, motor neurons innervating the extraocular muscles of the eye may only innervate as few as ten muscle fibers (Feinstein et al., 1955; MacIntosh et al., 2006). Regardless of motor unit size, once a motor neuron is activated, all the muscle fibers within the motor unit are stimulated to contract.

Control of force production is regulated at the next level of organization. All the motor units within a given skeletal muscle make up a motor pool. Within motor pools, functional differences among motor unit types can be used to categorize them into three subtypes: (1) slow twitch, fatigue resistant (S); (2) fast twitch, fatigue resistant (FR); and (3) fast twitch, fatigable (FF) (Kanning et al., 2010). As the names of the different subtypes suggest, they exhibit a range of different contractile and electrical properties. For example, type S motor neurons innervate slow (type I) muscle fibers and have a tonic firing pattern with slower axon conduction velocities. Conversely, type FF motor neurons innervate fast muscle fibers (type IIa/b/x) and have a phasic firing pattern with faster axonal conduction velocities (Kanning et al., 2010). In addition to the contractile differences of their targets, the different subtypes exhibit differences in cell body size that translate into variations in excitability. Smaller type S motor neurons have high input resistance, causing them to reach activation threshold faster and fire earlier, while larger type FF motor neurons are much larger in size, have lower input resistance, and take longer to reach activation threshold (Kanning et al., 2010). Ultimately, these characteristics come together in a physiological context in what is known as the Henneman's size principle, whereby motor units are recruited according to size with the smallest (type S) motor units recruited first. When stronger contractile forces are required, there is increased recruitment of progressively larger motor units.

Compared to synapses within the central nervous system, the accessibility and relative simplicity of the NMJ has made it an important model system to understand synaptogenesis and synaptic function. As such, decades of research have greatly contributed to our understanding of how the NMJ develops and is maintained throughout adult life. Although many different molecular processes and signaling pathways have been implicated in various aspects of NMJ function, our knowledge of how these complex systems respond to injury and disease is still an active area of investigation.

Development and Maintenance of the Neuromuscular Junction

During embryogenesis, the initial development of motor neurons and skeletal muscle occur independently. All spinal motor neurons derive from a single ventral progenitor domain in the neural tube. This domain is specified early in development through inductive gradients that drive the expression of a unique combination of transcription factors (NKX6.1/2, Pax6, and Olig2) (Tanabe et al., 1998; Novitch et al., 2001; Vallstedt et al., 2001). After specification, motor neuron progenitors exit the cell cycle and differentiate into post-mitotic motor neurons. Further specification into motor neuron subtypes only occurs as motor neurons extend their axons into the periphery to innervate distinct muscle groups. Skeletal muscle, on the other hand, is derived from skeletal muscle precursor cells that arise from the somites, which are paired blocks of paraxial mesoderm (Christ and Brand-Saberi, 2002). Once specified, committed muscle precursor cells migrate into the limb buds, where they differentiate into anatomically distinct muscle groups.

Two distinct phases of synapse formation are responsible for early NMJ development. Prior to motor innervation there is a prepatterning period that concentrates synaptic proteins, including AChRs, to the central region of the muscle. In the second phase, incoming motor axons branch as they approach the prepatterned muscle and nerve-secreted factors act to form and stabilize primitive synapses (Burden et al., 2013). Research over the past 20 years has identified three key players essential for this process. Muscle-specific kinase (MuSK) and LDL receptor related protein 4 (LRP4) are two postsynaptic proteins that have been found to act in both early muscle prepatterning and in the later stabilization of early synapses (Kim and Burden, 2008), while agrin was identified as the principle factor secreted by the motor nerve (Nitkin et al., 1987). Taken together, in our current model of NMJ formation, AChR and other synaptic proteins are produced uniformly throughout the muscle fiber in a dispersed pattern as myoblasts fuse to form myotubes. MuSK activation, possibly by LRP4 and/or other muscle derived ligands, initiates muscle prepatterning of postsynaptic proteins (Weatherbee et al., 2006; Kim et al., 2008; Jing et al., 2009). Then, agrin released by the innervating motor axon binds to LRP4, strengthening the MuSK-LRP4 association and resulting in full MuSK activation (Kim et al., 2008). Phosphorylation of MuSK subsequently activates signaling cascades that result in the clustering of AChRs and other synaptic proteins, including MuSK and LRP4 themselves (Burden et al., 2013). Finally, in addition to its postsynaptic roles, LRP4 was also found to act as a retrograde signal that initiates presynaptic differentiation of the motor axon terminal (Yumoto et al., 2012).

Once primitive NMJs are formed, synaptic maturation leads to dramatic changes in NMJ structure and function. In postnatal muscle, multiple motor axons initially innervate each muscle fiber at a plaque-shaped region of postsynaptic AChRs (Sanes and Lichtman, 1999). Over time, through a process called synaptic elimination, one motor axon gradually gains territory within the synapse as other axons lose branches and ultimately withdrawal (Tapia et al., 2012; Smith et al., 2013). Concomitantly, the shape of the postsynaptic membrane matures and is sculpted into a pretzel-like formation (Balice-Gordon and Lichtman, 1993; Sanes and Lichtman, 2001). Interestingly, early studies indicate that loss of polyinnervation during synaptic elimination is specifically due to retraction of terminal axon branches as opposed to a decrease in the number of motor neurons that innervate the muscle (Brown et al., 1976; Balice-Gordon and Thompson, 1988). Therefore, while synaptic elimination reduces the overall size of motor units, the total number of motor units within a given muscle remains unchanged (Sanes and Lichtman, 1999). While the precise mechanism of synaptic elimination remains to be elucidated, it has been postulated that electrical activity, retrograde signals released from the muscle, and microtubule dynamics mediate this process (Brill et al., 2016; Tomas et al., 2017).

Following the period of synaptic elimination and postsynaptic maturation, each NMJ is occupied by a single motor axon. From here, the overall geometry of the NMJ remains largely unchanged. In subsequent phases of muscle growth, muscle fibers increase in diameter and length, but the total number of fibers remains the same. Accordingly, it has been hypothesized that, while the early stages of synaptogenesis require more extensive nerve-muscle communication, later stages may rely more

heavily upon the tight adhesion of axon terminals to the postsynaptic apparatus (Balice-Gordon and Lichtman, 1990). Importantly, this stability has been observed to exist throughout adult life. For example, time lapse imaging studies in mice have revealed that NMJs neither add nor lose branches throughout the lifespan of the animal (Lichtman et al., 1987; Balice-Gordon and Lichtman, 1990). Despite the apparent macroscopic stability of the NMJ, individual components of the NMJ require active maintenance. For example, conditional LRP4 knockout studies demonstrated that muscle produced LRP4 is required for both the structural and functional maintenance of NMJ integrity in adult mice (Barik et al., 2014). Likewise, other proteins such as alpha-1-syntrophin (αSyn) and alpha-kinase anchoring protein (αkap) have been found to be necessary for the proper maintenance of AChR recycling required for proper synaptic transmission (Martinez-Pena y Valenzuela et al., 2011; Martinez-Pena et al., 2015).

In addition to the motor neuron and muscle cells, a third cell type known as the Schwann cell is required for NMJ function. Schwann cells develop from the neural crest and become associated with motor axons near the somites where they then follow motor axons through the periphery (Sanes and Lichtman, 1999). In the adult, Schwann cells can be found along the length of the motor axon, where they produce the insulating myelin sheath that enables the high-speed propagation of action potentials to the axon terminal. In addition to the myelin-producing Schwann cells, a specialized set of non-myelinating, terminal Schwann cells have been described in the perisynaptic region of the NMJ (Griffin and Thompson, 2008). There, they form an insulating blanket over the NMJ and function to modulate synaptogenesis and synaptic transmission (Sugiura and Lin, 2011; Barik et al., 2016).

Molecular Mechanisms that Regulate Motor Neuron Pathfinding

Prior to the establishment of the NMJ, motor axons must first traverse great distances to their appropriate targets. Coordination of motor axon pathfinding during development is a highly complex process that is orchestrated by a series of intrinsic and extrinsic factors (Bonanomi and Pfaff, 2010; Stifani, 2014). Proper axon pathfinding relies on three major events: 1) motor axons must be directed to properly exit the developing spinal cord, 2) intrinsic factors must act on groups of motor neurons to produce anatomically distinct motor columns that project to different target regions in a stereotyped pattern, and 3) receptor/ligand-mediated signaling pathways must be activated to ensure proper navigation through the limb mesenchyme. First, while most motor neurons will ultimately project their axons ventrally to form the ventral roots, in the cervical spinal cord there is a small population of genetically distinct motor neurons (called dorsal motor neurons) that project axons dorsally to exit the spinal cord through the dorsal root (Shirasaki and Pfaff, 2002). While the precise guidance mechanisms underlying these path choices are unclear, there is strong evidence that the chemokine Cxcr4/Cxcl12 (Lieberam et al., 2005) and netrin1/DCC (Dillon et al., 2005) initiated signaling cascades are responsible for ventral and dorsal motor neuron projections, respectively.

Next, motor neurons organize into discrete motor columns at appropriate rostrocaudal locations in the spinal cord. The acquisition of motor column identity is a complex process involving members of the LIM homeodomain (LIM-HD) class of transcription factors, as well as the HOX family of HD proteins (Dasen et al., 2003; Bonanomi and Pfaff, 2010). In addition to the intrinsically regulated transcription factor

profile, extrinsic factors produced in the limb mesenchyme act in concert to assure that the proper axon projections occur. Although six unique motor columns are ultimately generated through this process, the medial motor column (MMC) that innervates the axial musculature and the lateral motor column (LMC) that innervates the limbs have been the most extensively studied (Stifani, 2014).

As axial muscles extend the length of the body axis, the MMC motor column also spans the entire rostrocaudal axis of the spinal cord. Mature motor neurons of the MMC column uniquely express the LIM-HD protein Lhx3 (Tsuchida et al., 1994). Importantly, Lhx3 expression was found to be necessary and sufficient for MMC axon targeting of axial muscles that develop in the dermomyotome (Sharma et al., 1998). Furthermore, there are at least two additional mechanisms responsible for MMC axon pathfinding. First, Lhx3 expression was found upregulate fibroblast growth factor receptor 1 (FGFR1), resulting in an attraction to FGF secreted by the dermomyotome (Shirasaki et al., 2006). Concomitantly, expression of two eph receptors (EphA3/A4) by MMC axons is necessary for repulsion of MMC axons from the DRG and limb buds (Gallarda et al., 2008).

While the MMC motor column spans the entire spinal cord, the LMC motor column is responsible for innervating the limb musculature and only forms at cervical and lumbar regions. Importantly, dorso-ventral patterning of the limb results from a further subdivision of the LMC into lateral (LMCl) and medial (LMCm) populations. As such, LMCl motor neurons that will innervate the dorsal extensor muscles have been found to express the LIM-HD proteins islet2 (Isl2) and lhx1, while LMCm motor neurons that will innervate the ventral flexor muscles express the LIM-HD protein Isl1 (Kania et

al., 2000). Furthermore, multiple mechanisms have been identified that help to ensure the fidelity of LMCl and LMCm targeting. First, LMC axons have been observed to pause before entering the limb bud (Lance-Jones and Landmesser, 1980; Huber et al., 2005). Interestingly, this pause was found to be dependent on the axon guidance molecule Semaphorin3A (Sema3A) and its receptor neuropilin1 (Npn1), as removal of Sema3A signaling resulted in improper LMC axon defasciculation, premature entry into the limb bud, and improper dorso-ventral axon targeting (Huber et al., 2005). Additionally, ephrin/eph repulsive signaling has been shown to be required in both LMCl and LMCl populations. More specifically, the ventral mesenchyme produces ephrinA ligands to repel LMCl axons that express EphA4 (Kania and Jessell, 2003), while the dorsal mesenchyme produces ephrinB ligands to repel LMCm that express EphB1 (Luria et al., 2008). Finally, in addition to ephrin signaling, the axon guidance molecule Semaphorin3F (Sema3F) and its receptor Neuropilin2 (Npn2) have been found to restrict LMCm axons to the ventral limb (Huber et al., 2005), while the neurotrophic factor glial cell line-derived neurotrophic factor (GDNF) and its receptor RET act to restrict LMCl axons to the dorsal limb (Kramer et al., 2006).

Neuromuscular Activity in Injury and Disease

There is a large overlap in the signaling mechanisms involved in the establishment of the NMJ and how it responds to both injury and disease. Interestingly, the central and peripheral nervous systems exhibit a well appreciated dichotomy in regenerative capability. Both intrinsic and extrinsic factors in the central nervous system actively inhibit the activation of regenerative programs, while the peripheral system is

capable of mounting robust regenerative responses after injury (Giger et al., 2010). For example, spinal cord injuries (SCI) that impede the transmission of signals required for motor neuron activation often repair poorly and ultimately results in paralysis, whereas damage to the peripheral motor nerve is usually associated with better clinical outcomes. However, it is important to note that although the peripheral nervous system is better equipped to respond to acute injuries, not all peripheral nerve injuries are repairable. In fact, patient disability and morbidity is a common consequence of peripheral nerve injuries and less than half of the patients who undergo nerve repair procedures fully regain motor or sensory function (Grinsell and Keating, 2014).

Acute injury involving either the crushing or severing of peripheral nerves can lead to disruptions of neuromuscular activity. The type and extent of the injury, however, have important consequences on the resulting repair process. Initially, the response to any type of peripheral nerve damage is similar because the axon distal to the injury site must first be cleared through a process known as Wallerian degeneration. In Wallerian degeneration, Schwann cells near the injury site dedifferentiate into non-myelinating Schwann cells where they serve to both remove myelin debris (both directly and through the recruitment of macrophages) and secrete pro-regenerative factors that act on injured motor axons (Gaudet et al., 2011; Grinsell and Keating, 2014). In the next phase of regeneration, motor axons begin to grow in an attempt to return to their original targets. Importantly, after compression injury or even with minor nerve transection, the endoneurial sheath that surrounds the myelinated fibers remains intact and serves as a conduit back to the denervated motor endplates. The returning motor axons then branch and reinnervate vacated muscle endplates with the assistance of terminal Schwann

cells (Reynolds and Woolf, 1992; Kang et al., 2003; Dalkin et al., 2016). Additionally, like NMJ innervation during development, reinnervated NMJs are initially hyperinnervated by more than one motor axon. Over a period of a few weeks, newly innervated synapses mature and synaptic elimination results in the reestablishment of a one-to-one connection (Kang et al., 2003; Magill et al., 2007).

Although regeneration in idealized circumstances like that described above can be quite robust, there are many situations in which severe trauma and/or inefficient repair leads to poor NMJ reinnervation, thereby resulting in significant deficits in motor function (Burnett and Zager, 2004). First, it has been well established that large scale nerve transections fail to regenerate because motor neuron axons become stranded without a path back to their target regions. Additionally, delayed regeneration has also been found to result in poor recovery of motor function, even though axons are able to reestablish synaptic contacts at the NMJ (Ma et al., 2011; Sakuma et al., 2016). Finally, diseases such as diabetes and normal organismal aging have been associated with poor peripheral nerve regeneration (Kennedy and Zochodne, 2000; Kawabuchi et al., 2011; Kang and Lichtman, 2013).

In addition to acute trauma caused by injury, chronic NMJ denervation resulting from neurodegeneration also has severe consequences on neuromuscular function. Motor neuron diseases (MNDs) were first described by the French neurologist Jean-Martin Charcot in 1874. Since that time, MNDs have been described as a heterogeneous group of related neurodegenerative disorders that affect the motor neurons in the brain and spinal cord. Degeneration of these motor neurons leads to weakness and wasting of skeletal muscles, resulting in paralysis. Ultimately, loss of

muscle function leads to premature death due to difficulties in swallowing and breathing (Kanning et al., 2010).

MNDs can be characterized by their pattern of onset and the type of motor neurons affected. The most common MND is amyotrophic lateral sclerosis (ALS), which involves both the upper corticospinal MNs of the motor cortex and the lower MNs in the spinal cord that innervate the skeletal muscle. However, other MNDs are known to have selective involvement of either upper MNs (primary lateral sclerosis) or lower MNs (progressive muscular atrophy and spinal muscular atrophy) (Bozzoni et al., 2016).

In recent years there has been an increasing amount of attention aimed at understanding the complex genetic etiology of MNDs. Broadly speaking, MNDs are classified into two groups: familial and sporadic. Interestingly, only about 10% of all clinical cases are classified as familial. The vast majority of the remaining MND patients have a sporadic form of the disease that is thought to be caused by a combination of genetic, environmental, and/or other unknown factors (Renton et al., 2014). Importantly, we have made significant progress in identifying some of the genes whose dysfunction lead to ALS. They include, amongst others, Superoxide Dismutase 1 (SOD1), TAR DNA-binding protein (TARDBP), Fused in sarcoma (FUS), and a hexonucleotide repeat in C9orf72 (Renton et al., 2014). Despite unmasking some of the underlying factors in MND, we still do not have a firm understanding as to how mutations in the various genes lead to ALS symptoms. Several hypotheses have been proposed including, abnormal protein function and RNA processing, mitochondrial dysfunction, motor neuron hyperexcitability, and metabolic dysfunction (Ngo and Steyn, 2015). Finally, although many mechanisms of degeneration have been attributed to ALS, one

interesting observation has been that denervation of the NMJ occurs before any detectible signs of dysfunction are seen in motor neuron cell bodies. This has led to the 'dying-back hypothesis', which suggests that neurodegeneration in ALS is primarily initiated at the motor neuron terminal and that protecting the NMJ from denervation may be a therapeutically valuable way to delay or even prevent neurodegeneration (Dadon-Nachum et al., 2011).

Leveraging Developmental Pathways for Motor Neuron Degeneration

Research from many laboratories suggest that mechanisms employed by developing motor axons are coopted by regenerating adult motor neurons in response to injury and disease. For example, several neurotrophic factors including GDNF (discussed above), brain-derived neurotrophic factor (BDNF), and ciliary neurotrophic factor (CNTF) have been studied in the context of motor nerve regeneration after injury and in neurodegeneration resulting from MND. Numerous studies have found that loss of neurotrophic factor signaling impairs the regenerative response after sciatic nerve crush (Yao et al., 1999; Chen et al., 2016). Alternatively, enhancing neurotrophic factor signaling can both improve recovery of motor function after injury (Magill et al., 2010; Zheng et al., 2016) and extend lifespan in mouse models of ALS (Ikeda et al., 1995; Li et al., 2010). Similar to the neurotrophic factors, the functions of various other growth factors including insulin-like growth factor 1 (IGF1) and vascular endothelial growth factor (VEGF) have been found to improve regeneration in response to mouse models of injury (Islamov et al., 2004; Apel et al., 2010) and ALS (Kaspar et al., 2003; Dobrowolny et al., 2005; Storkebaum et al., 2005; Zheng et al., 2007).

Finally, the role of axon guidance molecules in axon regeneration has been of immense interest (Yaron and Zheng, 2007). With specific respect to the NMJ, two families of axon guidance molecules have received the most attention. First, a genetic screen in zebrafish recently identified the ephrin receptor EphA4 as a modifier of ALS disease progression. Further studies in mice revealed that both the genetic and pharmacological blockade of EphA4 signaling improved NMJ reinnervation after a denervating injury and significantly improved motor function and lifespan in ALS mouse models (Van Hoecke et al., 2012). The second axon guidance molecule that has been proposed to play a role at the NMJ is Sema3A. In addition to the role Sema3A plays in developmental LMC motor axon projections from the spinal cord (discussed above), *Sema3A* mRNA has also been described to be upregulated at the NMJ in response to denervation and in neurodegeneration (De Winter et al., 2006). Interestingly, the production of *Sema3A* was specifically found at NMJs on fast muscle fibers that have previously been associated with poor axonal sprouting after injury and increased susceptibility to disease (Duchen, 1970; Lowrie et al., 1982; Frey et al., 2000). Given that Sema3A is a well-established axonal chemorepellent that exerts its actions through modification of the cytoskeleton (Luo et al., 1993; Messersmith et al., 1995), the authors proposed that Sema3A signaling at the NMJ might create an inhibitory environment that dampens regenerative capacity. Additionally, a more recent study has lent more support to this hypothesis as it was found that systemic inhibition of the Sema3A receptor, Npn1, improved motor function and lifespan in an ALS mouse model (Venkova et al., 2014).

Taken together, many of the findings discussed in this section demonstrate that exploiting developmental signaling pathways can lead to improvements in recovery from injury and may be protective against neurodegeneration. However, despite some provocative early studies suggesting Sema3A is a negative regulator of NMJ function, to date the functional consequences of Sema3A signaling at the NMJ remain to be elucidated. Therefore, to address this, in Chapter 2 we established a common peroneal nerve crush model that allows for the quantitative assessment of NMJ reinnervation. Using this model in conjunction with conditional knockout mice, we directly interrogated the role of Sema3A signaling in maintenance and regeneration of the adult NMJ.

Global Regulation of Motor Neuron Gene Function

Targeted approaches are useful to investigate the function of specific signaling pathways, but for rapid and unbiased identification of which pathways are most relevant, large scale screens are necessary. This is especially true when considering the challenges posed by understanding complex, heterogenous neurodegenerative diseases like MND. With the advent of increasingly sophisticated sequencing technology, the pace at which genes associated with ALS have been discovered as accelerated dramatically (Renton et al., 2014). Importantly, this has led not only to a better clinical understanding of MND, but has also highlighted new pathways and mechanisms that might be critically important to disease pathogenesis. For example, the discovery that mutations in TARDBP, FUS, and C9ORF72 can result in ALS has implicated disruptions of RNA metabolism as being central to neurodegeneration in ALS patients (Droppelmann et al., 2014; Renton et al., 2014).

In addition to the importance of RNA metabolism in maintenance of motor neuron health throughout life, over the past 20 years the role of local translation has gained increasing attention. Research in many different cell types has revealed that local translation is a widely utilized mechanism by which cells can spatially and temporally regulate where proteins are produced in response to different stimuli (Holt and Schuman, 2013). In neurons, the concept of local translation is particularly attractive given that they are a highly compartmentalized cell type with extensive dendritic arborizations and axon terminals located long distances from the cell body. Indeed, polyribosomes have been identified at the base of dendritic spines (Steward and Levy, 1982) where local translation plays key roles in synaptic plasticity and learning and memory (Sutton and Schuman, 2006). Many studies have also found that local translation in axons is involved in axon guidance and growth cone collapse (Campbell and Holt, 2001; Wu et al., 2005; Yao et al., 2006), as well as in the axonal response to injury and disease (Verma et al., 2005; Willis and Twiss, 2006). To date, the extent of local translation in motor neurons *in vivo* has not been well established. However, a wide array of axonally localized transcripts has been reported using compartmentalized cell culture systems (Briese et al., 2016) and local translation in neuronal growth cones was found to be disrupted in an *in vitro* cell culture model of spinal muscular atrophy (SMA) (Fallini et al., 2016).

While we have gained extraordinary insight into how motor neurons develop and function in regeneration and disease, established methods of assessing motor neuron gene expression *in vivo* have been hampered by the inability to isolate them from surrounding cell populations in a sufficiently pure, efficient and cost-effective manner.

Recent advances in transgenic mouse models through the development of translating ribosome affinity purification (TRAP) technology has allowed for isolation of ribosomal bound mRNA transcripts in a cell-type specific manner. In Chapter 3, we explore how this technology can be harnessed to examine motor neuron specific gene expression and local translation. Furthermore, we also provide proof-of-principle evidence that this technique is suitable for translatomic analysis that can be applied to novel gene discovery.

CHAPTER 2: SEMAPHORIN3A SIGNALING IS DISPENSABLE FOR MOTOR AXON REINNERVATION OF THE ADULT NEUROMUSCULAR JUNCTION

Summary

The neuromuscular junction (NMJ) is a specialized synapse that is formed by the innervation of skeletal muscle fibers by motor axons. Importantly, the maintenance of motor-muscle connectivity is critical for the preservation of muscle tone and generation of movement. Although motor axons can initiate a robust regenerative response to injury, severe trauma or chronic denervation brought about by neurodegenerative disease typically leads to inefficient repair and poor functional recovery. The axon guidance molecule Semaphorin3A (Sema3A) has been implicated as a negative regulator of motor innervation. Upon binding to a plexinA-neuropilin1 (Npn1) receptor complex, Sema3A initiates a downstream signaling cascade that results in axonal repulsion. Here, we established a reproducible nerve crush model to quantifiably assess motor nerve regeneration. We then used this model to investigate the role of Sema3A signaling at the adult NMJ. In contrast to previous findings, we found that *Sema3A* and *Npn1* mRNA decrease in response to denervation, suggesting that Sema3A-Npn1 signaling might play a role in reinnervation of the NMJ. To directly test that hypothesis, we used conditional knockout models to ubiquitously delete Sema3A or Npn1 from adult mice. Despite demonstrating that we could achieve highly efficient gene deletion, disruption of Sema3A-Npn1 signaling did not affect the normal maintenance of the NMJ

or alter the pattern of motor axon reinnervation after a denervating injury. Thus, the utility of targeting this pathway to improve recovery from denervating injuries may be more limited than suggested by earlier studies.

Introduction

Complex motor function is achieved by proper communication between the motor neuron and skeletal muscle at a specialized synapse called the neuromuscular junction (NMJ). Throughout life the maintenance of the NMJ requires the coordinated effort of three main structures: the presynaptic motor neuron terminal, the postsynaptic muscle apparatus, and terminal Schwann cells (TSCs). In healthy animals, a denervating injury generates a regenerative response in which both intrinsic and extrinsic factors act on motor nerve terminals to stimulate growth and axonal sprouting that allow for muscle fiber reinnervation (Kawabuchi et al., 2011). Due to their key role in establishing target innervation during development, axon guidance molecules have been broadly proposed to play roles in peripheral nerve regeneration after injury (Yaron and Zheng, 2007) and in response to neurodegenerative disease (Schmidt et al., 2009; Moloney et al., 2014).

Semaphorin3A (Sema3A) is one example of an axon guidance molecule that has been implicated in peripheral nerve regeneration. It belongs to the large family of semaphorins, which are defined by the presence of a conserved Sema domain at their amino-terminus (Fiore and Puschel, 2003). Class III semaphorins, including Sema3A, are secreted glycoproteins that signal through a multimeric receptor complex. For Sema3A, this receptor complex is composed of a class A Plexin (PlxA1-A4) and Neuropilin1 (Npn1). While PlxA receptors contain a large intracellular domain that

initiates downstream signaling, the Npn1 receptor serves as a high affinity binding partner that acts to stabilize the Plexin-Sema3 interaction (Janssen et al., 2012). Importantly, both PlxAs and Npn1 are absolutely required for Sema3A-mediated signal transduction (He and Tessier-Lavigne, 1997; Kitsukawa et al., 1997; Kolodkin et al., 1997; Takahashi et al., 1999; Gu et al., 2003; Yaron et al., 2005).

Originally discovered as a chemorepellent that promotes sensory axon growth cone collapse (Luo et al., 1993; Messersmith et al., 1995), Sema3A has since been found to play a role in motor and sensory axon fasciculation and pathfinding during development (Behar et al., 1996; Taniguchi et al., 1997; Huber et al., 2005), pruning of hippocampal axons (Bagri et al., 2003), inhibition of cortical axon collateral branching (Dent et al., 2004), and control of dendritic development (Shelly et al., 2011) and arborization (Cheadle and Biederer, 2014). In the peripheral nervous system, previous studies reported that Sema3A is elevated in response to a nerve crush injury (Scarlato, 2003; Ara et al., 2004). Furthermore, the upregulated *Sema3A* transcript was found to be specifically localized to fast type IIb/x muscle fibers, while slow type I/IIa muscle fibers did not express *Sema3A* (De Winter et al., 2006). Intriguingly, while fast and slow motor units are known to have different metabolic and contractile properties (Kanning et al., 2010), they also exhibit well documented differences in response to injury and neuropathology. Specifically, fast motor units are more susceptible to neurodegeneration resulting from amyotrophic lateral sclerosis (ALS), spinal muscular atrophy (SMA), and even normal organismal aging (Frey et al., 2000). Additionally, fast muscle fibers exhibit less axonal sprouting and tend to repair poorly, while slow fibers exhibit heightened axonal sprouting and repair more efficiently (Duchen, 1970; Lowrie et

al., 1982; De Winter et al., 2006). Taken together, this previous work suggests a model by which the presence of Sema3A at the NMJ on fast muscle fibers generates a growth-inhibitory environment that may serve to reduce axonal sprouting and repair in response to injury.

In this study, we sought to directly test whether Sema3A signaling plays a functional role during reinnervation of the NMJ. To this end, we developed and characterized a nerve crush model that is highly reproducible and allows for the quantification of distinct phases of NMJ reinnervation. To avoid deficits due to the established role of Sema3A in the development of the peripheral nervous system, we generated conditional knockout mice that allowed for the ubiquitous deletion of either Sema3A or Npn1 from adult mice. Contrary to the proposed role of Sema3A predicted by previous studies, we found that Sema3A signaling appears to be largely dispensable for normal NMJ reinnervation in response to injury.

Results

To directly examine whether Sema3A signaling plays a role in NMJ reinnervation, we needed a reproducible nerve crush model that would allow us to quantify the different phases of NMJ reinnervation. To this end, we chose to perform the nerve crush on the common peroneal branch of the sciatic nerve that innervates the anterior muscles of the distal hindlimb. The advantage of this approach is that it allows us to examine reinnervation in the extensor digitorium longus (EDL), which is a thin muscle amenable to systematic and thorough analysis. Additionally, based on previously published studies, we could also predict the approximate time course of initial muscle

denervation and subsequent reinnervation (Magill et al., 2007; Bauder and Ferguson, 2012; Dalkin et al., 2016). The experimental design we used to fully characterize this nerve crush model is illustrated in Fig. 2.1*A*. Briefly, a common peroneal nerve crush and a contralateral sham surgery were performed on wild-type mice. Injured and control EDL muscles were then collected at different time points (D2-D30) and processed to systematically collect longitudinal sections throughout the entirety of the muscle (see Materials and Methods). Finally, sections were immunostained and analyzed to quantify the extent of NMJ denervation or reinnervation.

To ensure that the nerve crush injury induced a complete withdrawal of motor axons from the EDL muscle, we utilized *Thy1*$^{CreERT2\text{-}EYFP}$ mice that exhibit strong YFP expression in peripheral nerves. Sham-injured and denervated EDLs were collected two days after nerve crush and whole mount imaging was used to broadly examine denervation after injury. As expected, intact YFP^{+} innervation was observed in sham-injured EDLs, while a dramatic and uniform loss of YFP signal was apparent two days after nerve crush (Fig. 2.1*B*). In addition to loss of innervation we also confirmed that newly reinnervating motor nerves were initially unmyelinated following common peroneal nerve crush (Fig. 2.1*C*). D4 sham-injured and denervated EDLs were stained with a combination of bungarotoxin (BTX) and βIII-tubulin (green), S100 calcium binding protein (S100b, blue) and myelin basic protein (MBP, magenta). Sham-injured endplates exhibited normal innervation and myelination patterns (Fig. 2.1*C*, left panels). More specifically, βIII-tubulin^{+} motor nerves were seen innervating BTX labeled endplates. While both S100b and MBP labeled the myelin sheath coating axons as they innervate the NMJ, only S100b was observed to extend into the endplate region. In

contrast, at D4 after nerve crush, reinnervating βIII-tubulin^{+} motor nerves exhibited a marked reduction of S100b and only fractured pockets of MBP staining was evident (Fig. 2.1*C*, right panels).

After characterizing that this injury model could yield reproducible and uniform denervation, we sought to devise a scoring system that would allow us to quantify different degrees of NMJ reinnervation. BTX (magenta) was used to identify the endplate region, while βIII-tubulin (green) and synapsin (blue) were used as markers for nerve reinnervation and presynaptic differentiation, respectively. Six different morphological categories were created to reflect the innervation status of individual NMJs (Fig. 2.1*D*): completely denervated (Score 0), motor nerve is approaching, but not yet innervating an endplate (Score 1), less than 50% of the endplate area is covered (Score 2), more than 50% of the endplate area is covered (Score 3), full coverage but immature (Score 4), and completely reinnervated (Score 5).

Next, we applied this scoring system to quantify reinnervation in C57BL/6 wild-type mice at various time points following nerve crush. Importantly, the total number of individual NMJs analyzed per mouse was consistent across all time points, with approximately 200-300 in plane NMJs analyzed per mouse (Fig. 2.1*E*). Furthermore, graphing the percent of NMJs scored 0-5 points based on βIII-tubulin (Fig. 2.1*F*) and synapsin (Fig. 2.1*G*) staining revealed that this scoring system could indeed identify unique phases of denervation and reinnervation occurring at different time points. Almost all NMJs at D2 after injury were completely denervated and received a score of zero. By D4 the motor nerve started reentering the EDL and a few endplates were beginning to be reinnervated, but no presynaptic differentiation was observed (all

synapsin based scores were zero). From D7 to D14 increasingly more NMJs became reinnervated, while from D14 to D30 maturation of the innervating motor nerve could be observed as scores shifted from 3 or 4 to an increasing number of 5s. Although innervation at D30 began to approach that observed in sham-injured EDLs, full recovery had not yet occurred. Taken together, our data demonstrates that we can use this common peroneal nerve crush model to carefully interrogate motor axon regeneration, synaptogenesis and remyelination after nerve injury.

Sema3A Signaling Family Gene Expression

Previous work examining Sema3A signaling at the NMJ found that *Sema3A* mRNA was not detectable in normally innervated muscle. However, a dramatic upregulation of *Sema3A* was observed after nerve crush injury in the fast-twitch fiber types of the gastrocnemius (GP) muscle, while the slow-twitch fibers of the soleus (Sol) muscle showed no response (De Winter et al., 2006). Like the GP, the EDL is predominately composed of fast-twitch fibers. Therefore, we reasoned that patterns of Sema3A signaling should be similar in the two muscles. To directly examine this, we isolated RNA from wild-type GP, Sol, and EDL muscles and from the spinal cord (SC). RT-qPCR was then used to analyze *Sema3A* and its signaling partners at the transcript level (Fig. 2.2). As a control for our three muscles of interest, we examined the expression of different isoforms of myosin heavy chain (Myhc) that are known to be more representative of fast- or slow-twitch fiber types (Agbulut et al., 2003). As expected, the Sol muscle exhibited a strong enrichment in the slow myosin isoforms *Myhc-I* (GP, $p = 0.006$; EDL, $p = 0.0033$) and *Myhc-IIa* (GP, $p = 0.015$; EDL, $p =$

0.0016), while the fast isoform *Myhc-IIb* was dramatically upregulated in the GP ($p < 0.0001$) and the EDL ($p < 0.0001$). Furthermore, a similar level of *Myhc-IId/x* was observed in all three muscle groups and the embryonic Myhc (*Mych-EMB)* was barely detectable in any of the adult muscles (Fig. 2.2*A*).

Once we established that proper *Myhc* isoform profiles were expressed in the different muscle groups, we examined the expression levels of *Sema3A*, *PlxA*, and *Npn* transcripts. In contrast to what had been previously reported (De Winter et al., 2006), we could reproducibly detect *Sema3A* mRNA in uninjured adult skeletal muscle (Fig. 2.2*B*). More specifically, we found that *Sema3A* was expressed at a similar level in the GP (1.00 ± 0.17), EDL (1.30 ± 0.01), and SC (2.635 ± 0.55), while a significant reduction of transcript was observed in the slow-twitch Sol (0.295 ± 0.06) muscle compared to the GP ($p = 0.014$), EDL ($p < 0.0001$) and SC ($p = 0.019$). Additionally, analysis of *PlxA1-A4* (Fig. 2.2*C*) and *Npn1-2* (Fig. 2.2*D*) family members revealed that all receptor components were generally expressed at similar levels within the different muscles examined, except for *PlxA1*, which had the highest expression in the GP and lowest expression levels in the Sol.

To examine if *Npn1* and *Sema3A* transcript levels change in response to a denervating injury, a common peroneal nerve crush was performed on wild-type mice. Uninjured (UI) and denervated EDLs were then collected at different time points (D7-D50) after injury. In some cases, a nerve cut was performed instead of a nerve crush and tissue was collected at D21 to examine how gene expression was altered in the absence of reinnervation. Several control genes were used to monitor the progression of the degenerative and regenerative response to the nerve crush. Muscle-specific

kinase (MuSK), one of the main components of the postsynaptic apparatus, and Growth-associated protein 43 (GAP43), a gene associated with regenerating axons and Schwann cells, have both previously been reported to be induced by denervating injuries (Bowen et al., 1998; Xu et al., 2008; Li et al., 2010). Conversely, myelin protein zero (MPZ) and S100b are expressed by myelinating cells and have been reported to be reduced following nerve crush (Gupta et al., 1988; Mitchell et al., 1990; Magill et al., 2007; Li et al., 2010). Overall, we observed similar trends in gene expression in response to a common peroneal nerve crush to what has been reported for other injury models. *MuSK* was significantly upregulated at D7 after nerve crush (UI, 1.00 ± 0.06; D7, 5.03 ± 0.69, $p < 0.0001$), but returned to baseline by D21 (D21, 0.84 ± .07, n.s.). Furthermore, preventing reinnervation resulted in a prolonged upregulation of *MuSK* mRNA (8.50 ± 0.69, $p < 0.0001$) at the D21 time point (Fig. 2.3*A*). Similar to *MuSK*, a strong induction of *GAP43* mRNA was observed at D7 time point (UI, 1.00 ± .07; D7, 5.57 ± 0.86, $p < 0.0001$) and when reinnervation was blocked (D21 cut, 5.39 ± 0.3654, $p < 0.0001$); however, it exhibited a slower return to baseline uninjured levels (D21, 4.77 ± 0.62; D30, 1.98 ± 0.35; D50, 1.46 ± 0.10) over the 50-day time course (Fig. 2.3*B*). We also found that *MPZ* (Fig. 2.3*C*) and *S100b* (Fig. 2.3*D*) exhibited similar changes in gene expression in response to denervation. In both cases a significant reduction in gene expression was observed at the D7 time point (MPZ: UI, 1.00 ± 0.06, D7, 0.03 ± 0.02, $p < 0.0001$; S100b: UI: 1.00 ± 0.04, D7, 0.30 ± 0.08, $p < 0.0001$) with levels normalizing to that observed in the uninjured EDL by D21 (MPZ: D21, 2.61 ± 0.83; S100b: D21, 0.93 ± 0.15). Additionally, the restoration of *MPZ* and *S100b* mRNA levels

at the D21 time point could be prevented by prolonged denervation after nerve cut (MPZ: 0.06 ± 0.06, $p < 0.0001$; S100b: 0.29 ± 0.6).

Based on previous studies (Scarlato, 2003; Ara et al., 2004; De Winter et al., 2006) and the fact that we detected similar levels of *Sema3A* transcript in GP and EDL muscles (Fig. 2.2*B*), we hypothesized that nerve crush would result in increased expression of *Sema3A* mRNA in the EDL muscle. However, we observed that at D7 after a common peroneal nerve crush, there was a significant reduction in both *Npn1* (UI, 1.00 ± 0.04, D7, 0.51 ± 0.04, $p < 0.0001$) and *Sema3A* (UI, 1.00 ± 0.04, D7, 0.24 ± 0.03, $p < 0.0001$) mRNA (Fig. 2.3E,*F*). By D30 after the initial injury, *Npn1* levels returned to baseline (0.97 ± 0.06), while *Sema3A* mRNA levels partially rebounded by D21 after injury (0.57 ± 0.08, $p = 0.0001$), but remained significantly reduced compared to the uninjured control muscle throughout the entire time course (D30, 0.59 ± 0.08, $p = 0.04$; D50, 0.50 ± 0.04, $p = 0.003$). Altogether, these results suggest that there is decreased Sema3A signaling in response to denervation. Despite these unexpected findings, whether Sema3A signaling plays a functional role in the process of reinnervation remained an unanswered question.

Direct Examination of Npn1-Sema3A Signaling during Motor Reinnervation of the NMJ.

To directly test whether Sema3A signaling is required for reinnervation of the NMJ we used conditional knockout mice to delete Npn1 in adult mice (Fig. 2.4). As the high-affinity binding receptor for Sema3a, deletion of Npn1 renders cells insensitive to secreted Sema3A (Kitsukawa et al., 1997; Gu et al., 2003). *Npn1*$^{fx/fx}$ mice were crossed

to the *Ubiquitin-C*^{CreERT2} (*UBC*^{CreERT2}) mouse line to generate *Cre*-negative littermates or *Cre*-positive conditional mutants (Npn1^{UBC}). Tamoxifen (TMX) injections were then administered to initiate Cre-mediated recombination and after a resting period of 12-15 days, a common peroneal nerve crush or contralateral sham injury were performed. The EDL muscle was then collected at various time points and the extent of reinnervation was quantified (Fig. 2.4*A*). In some cases, Npn1^{UBC} mice were treated with corn oil (CO) and used as a vehicle control. Because *Cre*-negative and CO-treated Npn1^{UBC} mice behaved similarly by all parameters examined, both groups were combined into one Npn1^{WT} control littermate group. GP muscle and spinal cord tissue were collected from all mice examined in reinnervation analyses and were used to validate that an efficient and ubiquitous deletion of Npn1 was achieved. Analysis of *Npn1* transcript levels by RT-qPCR demonstrated that Npn1^{UBC} mice had dramatically lower levels of *Npn1* expression than littermate controls (% Knockdown: GP, 93.66% ± 1.20; SC, 91.44% ± 3.69; Fig. 2.4*B*). Furthermore, immunoprecipitation of Npn1 followed by immunoblotting showed that there was no detectable Npn1 protein in Npn1^{UBC} muscle (Fig. 2.4*C*) or spinal cord (Fig. 2.4*D*).

Once efficient knockdown of Npn1 was established, we analyzed reinnervation at the various time points after nerve crush. Similar to what we observed in wild-type mice (Fig. 2.1*E*), ~200-300 NMJs were scored at the various time points in Npn1^{WT} and Npn1^{UBC} mice (Fig. 2.4*E*). Additionally, we analyzed the sham-injured EDLs at the D30 time point and found no significant differences in the observed βIII-tubulin (Fig. 2.4*F*) or synapsin (Fig. 2.4*G*) scores between Npn1^{WT} and Npn1^{UBC} mice. Together, these

results reveal that Npn1 does not appear to be integral to either the postsynaptic apparatus after injury or for the normal maintenance of the NMJ.

To determine whether Npn1 was involved in reinnervation, we examined βIII-tubulin (Fig. 2.4*H*, *I*) and synapsin (Fig. 2.4*J*, *K*) staining over the entire 50 day time course. $Npn1^{WT}$ control littermates exhibited a pattern of reinnervation that closely resembled that observed in wild-type C57BL/6 mice (see Fig. 2.1*F*, *G*). Furthermore, the deletion of Npn1 did not appear to drastically impact the process of reinnervation in $Npn1^{UBC}$ mice. However, at the D30 time point, we did observe a shift towards lower reinnervation scores with $Npn1^{UBC}$ mice exhibiting more partially innervated NMJs (Synapsin Score 3: $Npn1^{WT}$, 9.87% ± 2.50%; $Npn1^{UBC}$, 17.67% ± 2.38%) and less fully innervated NMJs (Synapsin Score 5: $Npn1^{WT}$, 60.00% ± 8.08%; $Npn1^{UBC}$, 42.03% ± 2.65%). To examine this more closely, the reinnervation data for scores 3-5 were replotted to directly compare $Npn1^{WT}$ and $Npn1^{UBC}$ genotypes (Fig. 2.4*L*, *M*). Examination of the data in this manner revealed that there is a significant reduction (**p = 0.0037) of NMJs that received a fully reinnervated score of 5 based on synapsin staining at the D30 time point. Overall, our data suggests that loss of Npn1 may slightly delay synaptic maturation of the motor nerve at the reinnervating NMJ. This delay, however, is only temporary since both $Npn1^{UBC}$ and $Npn1^{WT}$ mice exhibit similar levels of presynaptic synapsin staining at D50 after injury.

In addition to examining reinnervation following Npn1 deletion, we also assessed the effect of Sema3A deletion on NMJ reinnervation. $Sema3A^{fx/fx}$ and $UBC^{CreERT2}$ mouse lines were crossed to generate *Cre*-negative littermates or *Cre*-positive conditional mutants ($Sema3A^{UBC}$). TMX or CO injections were then administered to induce Cre-

mediated recombination prior performing a common peroneal nerve crush. RT-qPCR and immunoblotting were again used to examine Sema3A gene and protein expression. Sema3A^{UBC} mice treated with TMX exhibited significant knockdown of *Sema3A* transcript compared to *Cre*-negative control littermates (% Knockdown: GP, 94.12% ± 0.69; SC, 89.29% ± 3.71). We also observed that CO-treated Sema3A^{UBC} mice showed a consistent, but partial reduction in *Sema3A* levels (% Knockdown: GP, 57.91% ± 7.27; SC, 66.39% ± 7.74; Fig. 2.5*A*). Deletion of Sema3A protein was also demonstrated through immunoblotting. A protein band corresponding to the expected molecular weight of Sema3A (95-105 kDA) was detected in Sema3A^{WT} mice, but was absent in TMX-treated Sema3A^{UBC} GP muscle (Fig. 2.5*B*). Although the partial reduction of *Sema3A* mRNA in CO-treated Sema3A^{UBC} mice did not appear to translate into an observable reduction of Sema3A protein (Fig. 2.5*B*), we excluded that control group from subsequent reinnervation analysis. Importantly, Sema3A deletion prior to a denervating injury did not impact reinnervation of the NMJ. Loss of Sema3A did not alter the number of scored NMJs at the various time points examined (Fig. 2.5*C*). Furthermore, no differences in reinnervation were observed at any time point (Fig. 2.5*D* – 5*I*).

Loss of Npn1 does not Disrupt Remyelination

Because it has been reported that terminal Schwann cells express Sema3A (De Winter et al., 2006), we explored whether the loss of Npn1 disrupted the process of myelination on newly extended motor axons. Npn1^{WT} and Npn1^{UBC} EDL sections from the D7 and D21 time points were immunolabeled with βIII-tubulin and BTX (green) to

visualize the motor nerve and the postsynaptic endplate region, while S100b (blue) and MBP (magenta) staining were used to visualize myelin proteins. Both innervation and myelination appeared normal in sham-injured sections (Fig. 2.6*A*), while varying degrees of NMJ reinnervation can be appreciated in both $Npn1^{WT}$ (Fig. 2.6*B*) and $Npn1^{UBC}$ mice (Fig. 2.6*C*) at the D7 time point after nerve crush. Furthermore, reinnervating motor axons of both genotypes exhibited similar levels of myelination as evidenced by the reduction in S100b staining and the absence of MBP. Finally, by the D21 time point, $Npn1^{WT}$ (Fig. 2.6*D*) and $Npn1^{UBC}$ (Fig. 2.6*E*) motor axons displayed strong S100b and MBP immunofluorescence, indicating that the deletion of Npn1 did not affect the process of remyelination.

Discussion

It has long been appreciated that peripheral nerves exhibit a remarkable degree of plasticity and regenerative ability after injury. However, depending on the extent of the trauma after an acute injury and in cases of chronic denervation brought about by neurodegenerative diseases, such as amyotrophic lateral sclerosis (ALS), the capacity for peripheral nerve regeneration can be greatly limited. Consequently, failures in proper reinnervation of skeletal muscle lead to a reduction in neurotransmission, which in turn dampens the trophic support required for motor neuron and muscle fiber survival. Therefore, deciphering the molecular mechanism that underlies the regenerative response of motor axons has been a major focus within the field. Furthermore, it has been hypothesized that the exploitation of these pathways will yield improvements in

motor axon regeneration that maximize muscle reinnervation in order to prevent functional deficits resulting from long-term denervation.

Although the regenerative response produced by denervation has already proven to be complex, many studies are beginning to tease apart the various signaling molecules that are likely playing key regulatory roles (Schmidt et al., 2009). Through its role as an axonal chemorepellent during development and its pattern of expression after injury at the NMJ, Sema3A signaling has been proposed to act as a negative regulator of motor axon reinnervation of the NMJ (De Winter et al., 2006). However, the functional consequences resulting from altered Sema3A signaling had not been previously examined.

Here, we fully characterized the regenerative response following a common peroneal nerve crush and demonstrated how it allows for the analysis of motor nerve reinnervation in a reproducible and highly quantifiable manner (Fig. 2.1). Using this model, we directly examined how motor axon terminals respond to a denervating injury in the absence of Sema3A signaling by employing conditional knock-out mice to delete Npn1, the high-affinity Sema3A binding receptor (Fig 2.4), or Sema3A itself (Fig 2.5). Despite demonstrating that we could achieve a highly efficient and ubiquitous gene knock-down, perturbing Sema3A signaling did not alter the time course of muscle reinnervation or myelination after injury.

While our study indicates that Sema3A signaling is not a necessary component of motor axon regeneration, we did observe some differences in *Sema3A* expression that conflict with what has previously been reported in other studies. Using a rat sciatic nerve crush model, De Winter et al., (2006) found that *Sema3A* is not normally

expressed in uninjured skeletal muscle. However, after a denervating injury, they found a dramatic upregulation of *Sema3A* mRNA in fast-twitch gastrocnemius muscle fibers, while the same response was not observed in the predominately slow-twitch soleus muscle. In contrast, we observed the opposite pattern of *Sema3A* expression in the fast-twitch EDL muscle after a common peroneal nerve crush. Namely, we could consistently detect *Sema3A* transcript in the uninjured adult EDL (Fig 2.2*B*) and we observed a significant decrease in *Sema3A* after nerve crush injury (Fig 2.2*F*). Although it is not directly apparent what factor or factors underlie these discrepancies, it may be possible there are species-specific differences between the two models. Another possibility is that dorsoventral patterning may lead muscles of the posterior (gastrocnemius) and anterior (EDL) leg compartment to utilize different signaling pathways in different ways. Finally, it is also interesting to note that data from both studies similarly suggests Sema3A signaling may be playing a larger role in fast-twitch muscle fibers. Although we did not examine how *Sema3A* levels are altered in the soleus muscle after injury, in uninjured muscle we found ~3-4 fold lower levels of *Sema3A* mRNA compared to that observed in the fast-twitch GP and EDL muscles (Fig 2.2*B*). What accounts for differences in *Sema3A* expression in different muscle groups and the significance of those differences, if any, remains an open question.

Recently, it has been proposed that Npn1-Sema3A signaling may play a role at the postnatal NMJ (Helmbrecht et al., 2015; Saller et al., 2016). However, for those studies the authors used the *Olig2* promoter to conditionally delete Npn1 from motor neurons. Because the *Olig2* promoter turns on very early in development (Masahira et al., 2006), it is not possible resolve whether the observed phenotype is due to an earlier

axon pathfinding defect or the loss of active Npn1-Sema3A signaling at the NMJ. Therefore, to our knowledge, this is the first published study to directly examine how the adult NMJ responds to the absence of Sema3A signaling. We addressed this question by examining innervation in sham-injured EDLs at the D21 time point and overall found no effect on the NMJ histology after Npn1 deletion. Both the total number of scored NMJs and their innervation status (as scored by nerve βIII-tubulin and the presynaptic marker synapsin) were similar among $Npn1^{UBC}$ and $Npn1^{WT}$ mice (Fig.2.4*F-G*). Lastly, it is important to note that while this analysis was performed at the D21 time point, we can estimate that Npn1 was ubiquitously deleted for ~1 month (see Fig. 2.4*A*). Furthermore, from previous studies it is known that acetylcholine receptors in uninjured skeletal muscle have a half turnover rate of about 10 days (Loring and Salpeter, 1980). Therefore, enough time should have elapsed to determine if Npn1 plays a major role in the maintenance of the NMJ.

An interesting observation we made following Npn1 deletion was that at the D30 time point there was a statistically significant decrease in the number of NMJs that received the highest innervation score based on synapsin staining (Fig 2.4*M*). However, the same effect was not observed after Sema3A deletion. This, combined with our finding that *Npn1* levels decrease after nerve crush and do not return to uninjured levels until the D30 time point, suggest that signaling through the Npn1 may play a minor role in the maturation of the presynaptic motor nerve after injury. It is also noteworthy that these observations fit with recently published studies of Npn1-Sema3A signaling at the NMJ. More specifically, a pharmacological inhibition of the Npn1 receptor was shown to delay denervation and prolong lifespan in an ALS mouse model (Venkova et al., 2014),

while mice engineered to express a mutated form of Sema3A protein did not display any defects in response to denervation or the neurodegenerative disease process (Moloney et al., 2017).

Taken together, the evidence to date suggests that Sema3A signaling is dispensable in the context of adult motor nerve regeneration. However, signaling through the Npn1 receptor may play a transient role in mediating NMJ synaptic maturation. Interestingly, Npn1 contains multiple extracellular domains that have been suggested to mediate a diverse array of protein interactions (Fujisawa et al., 1997; Nakamura and Goshima, 2002). For example, the vascular endothelial growth factor (VEGF) pathway has been well established to exert its signaling actions through the Npn1 receptor (Soker et al., 1998). Additionally, VEGF signaling has also been found to be protective against neurodegeneration in ALS mouse models (Storkebaum et al., 2005; Zheng et al., 2007), suggesting that VEGF-Npn1 signaling is an avenue that warrants further exploration. Finally, one intriguing possibility is that there is a compensatory pathway activated in the absence of Sema3A-Npn1 signaling. While we cannot specifically rule out this possibility, our work suggests that direct targeting of these pathways will not be a substantial avenue for future therapeutic research on nerve regeneration after injury. However, by continuing to better understand the complex processes that regulate muscle reinnervation we move closer to uncovering new strategies to promote motor axon regeneration and prevent functional deficits associated with both injury and disease.

Experimental Procedures

Animals. All housing and procedures performed on mice were approved by the Institutional Animal Care and Use Committee (IACUC) of the University of Michigan. Wild-type C57BL/6J (000664), *Thy1*$^{CreERT2\text{-}EYFP}$ (012708), and *UBC*^{CreERT2} (007001) mice were obtained from Jackson Laboratories (Bar Harbor, ME). *Npn1*$^{fx/fx}$ (Gu et al., 2003) or *Sema3A*$^{fx/fx}$ (Riken Bioresource Center, RBRC01106) conditional mice were crossed with *UBC*^{CreERT2} mice to generate *UBC*^{CreERT2};*Npn1*$^{fx/fx}$ (Npn1^{UBC}) and *UBC*^{CreERT2};*Sema3A*$^{fx/fx}$ mice (Sema3A^{UBC}). All mice were genotyped according to publicly available protocols except for Sema3A conditional mice. New primers (forward 5'-CACTGGGATTGCCTGTCTTT-3', and reverse 5'-ACGGAGCAAGCACACAGCTA-3') were designed to detect a 363bp wild-type band and/or a 400bp mutant band. For all experiments, both male and female mice were analyzed in similar numbers.

Conditional Deletion. Tamoxifen (TMX, Sigma-Aldrich) was administered at a dose of 0.25mg/g body weight to Npn1^{UBC} or Sema3A^{UBC} mice by oral gavage once a day for 5 days. Mice were then given a resting period of 12-15 days to allow for complete Cre-mediated recombination prior to performing nerve crush experiments (see Figure 2.1). In all experiments two types of control littermates were used: 1) *Cre* wild-type (*UBC*^{CreERT2} negative mice treated with TMX) and 2) vehicle only [*UBC*^{CreERT2} mice treated with corn oil (CO)]. For the Npn1-conditional deletion, both control groups behaved similarly and therefore all results were averaged and displayed as one wild-type control group (Npn1^{WT}). For the Sema3A-deletion, CO-treated mice exhibited a

partial reduction in *Sema3A* transcript levels (see Fig. 2.5*A*), so only *Cre* wild-type mice (Sema3A^{WT}) were used.

Common Peroneal Nerve Crush. Mice were deeply anesthetized with 2-3% isoflurane mixed with oxygen and the surgical site was shaved and disinfected. A small incision was made along the lateral aspect of the distal hindlimb from just above the ankle to just below the knee. A dissecting microscope was used to expose the common peroneal nerve through a small opening between the anterior compartment (tibialis anterior) and the posterior compartment (lateral gastrocnemius). The exposed nerve was then crushed by applying pressure with a pair of forceps for 40 sec. Following the crush procedure, the site where the anterior and posterior muscles were separated was closed with a suture and then the skin was sutured at the incision site. In a small number of experiments, a nerve cut was performed instead of a nerve crush. In these instances, the same procedure was performed except that a 3-5mm piece of nerve was excised as opposed to being crushed with forceps.

RNA Isolation and RT-qPCR. Tissues were harvested and snap frozen in liquid nitrogen. Homogenization was performed in TRIzol reagent (ThermoFisher) using a TissueLyser II (Qiagen) set at 30Hz for 5 min. Samples were then centrifuged at 12,000 x g for 10 min at 4°C. RNA was isolated by phase separation with chloroform followed by isopropanol precipitation (per the manufacture's protocol). In some instances, RNA was isolated with the Direct-zol RNA MiniPrep Kit (Zymo Research) according to manufacture guidelines. The concentration of isolated RNA was determined by

NanoDrop (ThermoFisher Scientific) and 1µg cDNA was synthesized using the Superscript III First-Strand Synthesis SuperMix kit (Invitrogen). RT-qPCR was performed using the 7900HT Fast Real-Time PCR System (Applied Biosystems) with the appropriate primer set (Table 1) and FastStart Universal SYBR Green Master Mix (Roche). B2M was used as an internal control for all dCT calculations and gene expression was calculated relative to the control condition.

Npn1 Immunoprecipitation. Muscle or spinal cord samples were dissected and placed into immunoprecipitation buffer (10% glycerol, C0mplete protease inhibitors (Roche), and sodium vanadate in Tris buffered saline (TBS), pH 6.8). Tissues were homogenized with the Tissue Lyser II (Qiagen) set at 30 Hz for 5min. Samples were then detergent extracted by the addition of nonidet p-40 (1% final concentration) followed by constant rotation for 30 min at 4°C and insoluble material was removed by centrifugation for 5 min at maximum speed in a microfuge. Before Npn1 immunoprecipitation (IP), samples were first precleared with a mixture of protein A/G agarose beads (Roche) for 1 hr. Next, a control IP was performed in which samples were incubated with a non-specific goat control antibody and protein A/G beads for 2 hrs. Finally, the Npn1 IP was performed overnight with a Npn1 antibody (AF566, R&D Systems) and protein A/G beads. For all incubations, samples were left under constant rotation at 4°C. The next day samples were lightly centrifuged (5000 rpm, 5 min) and the supernatant was collected and denatured in 2x sodium dodecyl sulfate (SDS) sample buffer (20% glycerol, 4% SDS, 1% β-mercaptoethanol, and bromophenol blue in TBS, pH 6.8) by heating for 10 min at 100°C. Meanwhile, the immunoprecipitated product was washed

three times with immunoprecipitation buffer followed by denaturation in the same manner as described for the supernatants.

Protein Isolation for Sema3A Immunoblotting. We used many different methods of protein isolation and various Sema3A antibodies to try and demonstrate effective knockdown of Sema3A protein Sema3A^{UBC} mice. However, most methods resulted in obtaining a non-specific protein band in the reported 95-105 kDA molecular weight range. The only methodology that we found to be successful was when protein was co-purified with RNA using the Direct-zol RNA MiniPrep Kit (Zymo Research). With this kit, after RNA binds to the RNA-binding cup, protein in the flow-through was precipitated with ice-cold acetone for 30min on ice. Samples were then centrifuged for 10 min at max speed to pellet the protein precipitate. The protein was then washed with 100% ice-cold ethanol, centrifuged again, and resuspended in water. Finally, the protein was denatured by adding an equal volume of 2x SDS sample buffer and heating for 10 min at 100°C.

Immunoblotting. All samples were resolved on a 7% (SDS)-polyacrylamide gel electrophoresis (SDS-PAGE) gel and transferred to polyvinylidene fluoride (PVDF) membranes. Membranes were blocked in 4% Milk in TBS-T (Tris buffered saline, pH 7.4 and 0.1% Tween-20) for 1hr at room temperature. Primary antibodies [α-Tubulin (1:30,000, T9026, Sigma-Aldrich), Actin (1:1,000, SC-1616-G, Santa Cruz), Npn1 (1:1,000, AF566, R&D Systems), or Sema3A (1:1,000, ab23393, Abcam)] were diluted in 3% bovine serum albumin (BSA) and incubated overnight at 4°C. The following day,

membranes were washed and incubated with appropriate horseradish peroxidase (HRP)-linked secondary antibodies (1:10,000) in 3% BSA (Jackson ImmunoResearch) followed by visualization with a chemiluminescent substrate (Thermo Scientific).

Tissue Preparation. EDL muscles were fixed in 4% paraformaldehyde (Electron Microscopy Sciences) for 10min at room temperature. Tissues were then washed 3x20min in phosphate-buffered saline (PBS) and soaked overnight in 30% sucrose at 4°C. Muscles were embedded in O.C.T compound (Tissue-Tek) and frozen at -80°C. 50µm longitudinal cryosections were cut using a CM1950 cryostat (Leica Biosystems) such that 3-5 sections approximately 300µm apart were placed on one slide.

Immunostaining. Sections were rehydrated in PBS and then permeabilized/blocked in 0.3% TritonX-100, 1% BSA, 10% donkey serum (Jackson ImmunoResearch), and MOM blocking reagent (Vector Laboratories) for 1hr at room temperature. Slides were then incubated in primary antibodies [Anti-Synapsin-1 (5297S, Cell Signaling), anti-β-Tubulin III (T8578, Sigma-Aldrich), anti-S100 (RB044A0, Thermo Scientific Lab Vision), anti-Myelin Basic Protein (AB9348, EMD Millipore)] in 0.3% Triton, 1% BSA overnight at 4°C. The following day sections were washed in PBS and stained with fluorescently-conjugated α-bungarotoxin and/or appropriate secondary antibodies (Biotium) in 0.3% Triton for one hour at room temperature. After final PBS washes, slides were coverslipped with DAPI mounting medium (Southern Biotech) and imaged on a confocal microscope (Leica SP5).

Reinnervation Analysis. Endplates identified by bungarotoxin staining were imaged at 20x magnification with high resolution (2048x2048) and a z-step size of 1.5µm. Every endplate on one slide containing 3-5 sections was imaged. Maximum projection (LAS Software, Leica Biosystems) was applied to all files and every in-plane NMJ was scored from 0-5 to reflect its innervation status. Two markers were used for innervation scores: 1) β-Tubulin III to reflect nerve reinnervation and 2) synapsin to reflect presynaptic differentiation. All imaging and scoring was performed by a single blinded observer that was unaware of the strain, genotype, and time point being analyzed.

Statistical Analysis.

All statistical analyses were performed using Prism 7 software (GraphPad). One- or two-way ANOVA was used for all analyses. Significant differences among pairwise comparisons were identified by Tukey's or Sidek's *post hoc* tests (Table 2). All graphs and error bars represent the mean ± standard error (se).

Acknowledgements

This work was supported by funding from NIH NINDS R01 NS089585 (B. Pierchala); NIH/NIDCR Tissue Engineering and Regeneration Training Grant T32-DE007057; NIH Cellular and Molecular Biology Training Grant T32-GM007315 (J. Shadrach). We thank P. Macpherson and D. Goldman for technical assistance related to the common peroneal nerve crush and C. Donnelly, R. Giger, and J. Hull for critical review of this work.

Gene	Forward Primer (5' – 3')	Reverse Primer (5' – 3')	BP	Source
B2M	TTCTGGTGCTTGTCTCACTGA	CAGTATGTTCGGCTTCCCATTC	104	Tan et al., 2011
Npn1	GAGGACAGAGACTGCAAGTATG	CTGAAGACACCACAGGAGAAG	115	Primer3
Sema3A	ATATGCAAGAATGACTTTGGTGGAC	AAGGAACACCCTTCTTACATCACTC	258	Primer3
GAP43	ATAACTCCCCGTCCTCCAAGG	GTTTGGCTTCGTCTACAGCGT	201	Harvard PrimerBank
MuSK	CCTCAGCCCGAGATTTCTTGG	GTCTTCCACGCTCAGAATGGT	111	Harvard PrimerBank
P0	CATCTCTTTTACCTGGCGCTAC	TGTAAGGTTGTCCCTTGGCATA	83	Harvard PrimerBank
S100	CTTCCTGGAGGAAATCAAGGAG	CTCATGTTCAAAGAACTCATGGC	148	Primer3
PlexinA1	GAGTGCAAGGAAGCTTTTGC	TCCTCAATCCCAGGAAACAG	131	Fukuda et al., 2013
PlexinA2	TATAACTGCAGTGCCCACCA	TGGGGACAGTCCTCTGAAAC	149	Primer3
PlexinA3	AGCATTCTGTGGTTTTCATCG	CACCTGCTTCTCACTCAGGA	179	Primer3
PlexinA4	ATCTAGAGTGGCGACAAGGAAG	TGGAGACAGTGGAGTTGTTCAC	189	Fukuda et al., 2013
MYH1	CTCTTCCCGCTTTGGTAAGTT	CAGGAGCATTTCGATTAGATCCG	187	Harvard Primer Bank
MYH2	ACTTTGGCACTACGGGGAAAC	CAGCAGCATTTCGATCAGCTC	155	Harvard Primer Bank
MYH3	CCAAAACCTACTGCTTTGTGGT	GGGTGGGTTCATGGCATACA	149	Harvard Primer Bank
MYH4	CTTTGCTTACGTCAGTCAAGGT	AGCGCCTGTGAGCTTGTAAA	139	Harvard Primer Bank
MYH6	TGCACTACGGAAACATGAAGTT	CGATGGAATAGTACACTTGCTGT	204	Harvard Primer Bank
MYH7	GCTACGCTTCCTGGATGATCT	CCTCTTAGTGTTGACAGTCTTCC	248	Harvard Primer Bank

Table 2.1. Primer Sequences used for real-time RT-qPCR in Chapter 2.

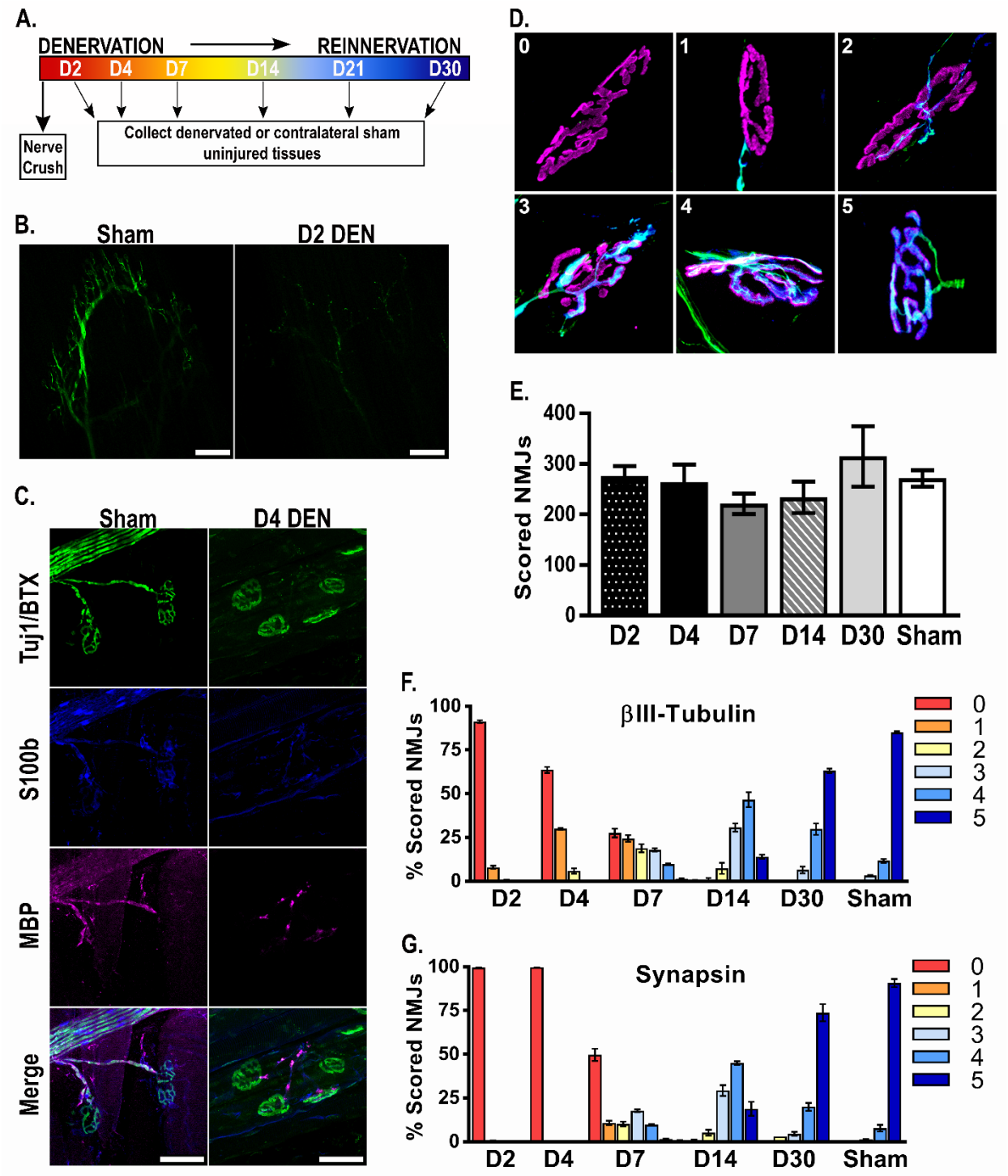

Figure 2.1. Characterization of the common peroneal crush methodology.
A, Graphical depiction of the experimental paradigm. A common peroneal nerve crush and contralateral sham operation were performed at day 0 (D0). Denervated (Den) and sham EDLs were collected at various time points following injury (n = 3 for all time points except D30, n = 2). ***B,*** Representative whole mount immunofluorescent images of sham (left) and D2 denervated (right) EDL sections from*Thy1*-YFP mice demonstrate a total loss of nerve innervation following the common peroneal nerve crush. Scale bar represents 250μm. ***C,*** Myelination at the D4 time point following nerve crush was examined by immunofluorescent staining. βIII-tubulin and acetylcholine receptors

stained with bungarotoxin (BTX) are shown in green, while the myelin markers S100 calcium binding protein B (S100b) and myelin basic protein (MBP) are shown in blue and magenta, respectively. Scale bar represents 50 μm. ***D,*** Representative images illustrate the scoring system (0-5) used to quantify NMJ reinnervation. BTX marks the endplate (magenta), βIII-Tubulin allows for visualization of the motor nerve (green), and synapsin stains the presynaptic nerve terminal (blue). ***E,*** The total number of neuromuscular junctions (NMJs) analyzed per animal was consistent across all time points analyzed (n.s., one-way ANOVA). ***F-G,*** Reinnervation was analyzed over the 30 day time course and the percent of NMJs scored as 0-5 is shown. Scoring was performed based on both nerve βIII-Tubulin staining (***F***) and presynaptic synapsin staining (***G***). Error bars represent the mean ± s.e

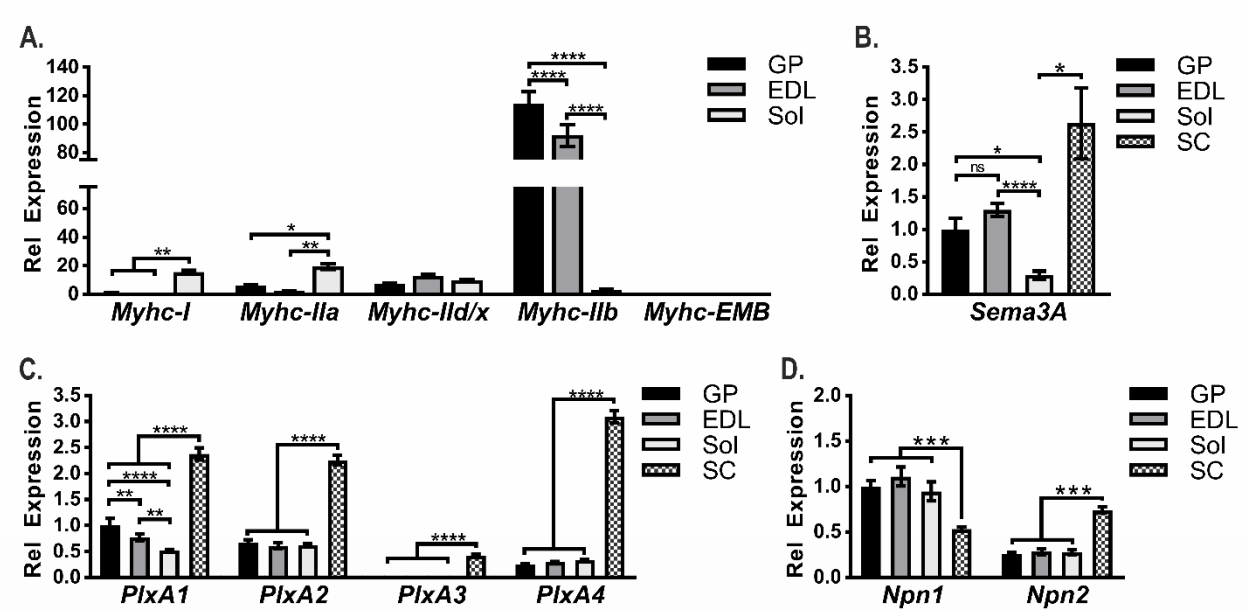

Figure 2.2. Sema3A and its receptor components are expressed in skeletal muscle and spinal cord. Quantitative real-time PCR (qRT-PCR) was performed on RNA isolated from the gastrocnemius/plantaris (GP), extensor digitorium longus (EDL), soleus (Sol), and spinal cord (SC) tissues of C57BL/6J mice (n = 6). Individual gene expression was normalized to the *β2-Microglobulin* (*B2M*) housekeeping gene. Myosin heavy chain (MyHC) isoforms (***A***), *Semaphorin3A* (*Sema3A*, ***B***), class A plexin family members (*PlxA1-4*, ***C***), and neuropilin family members (*Npn1-2*, ***D***) were examined. Error bars represent the mean ± s.e. *p ≤ 0.05, ** p ≤ 0.01, ***p ≤ 0.001, **** p ≤ 0.0001.

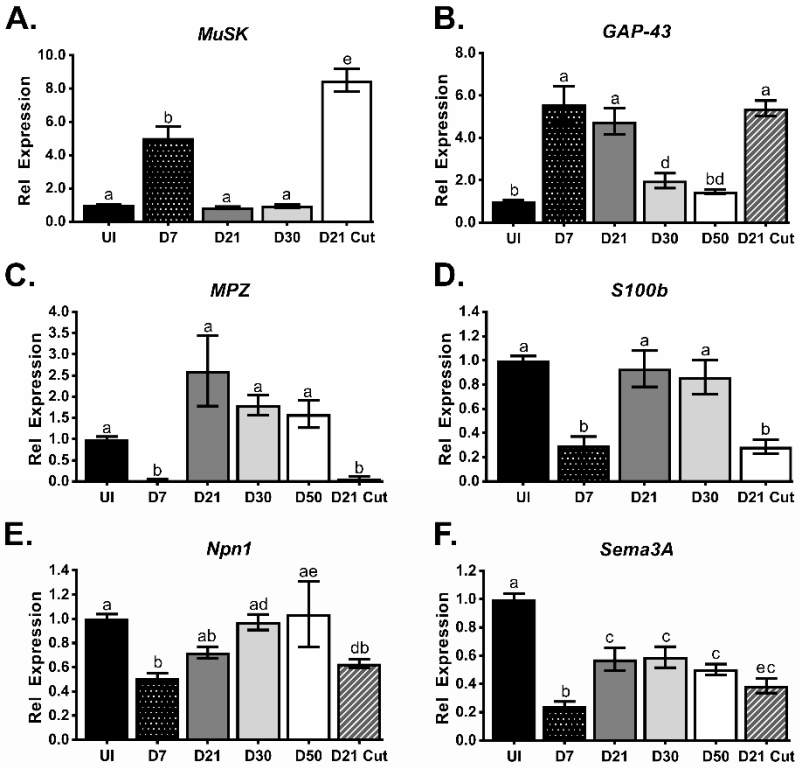

Figure 2.3. *Sema3A* and *Npn1* gene expression decrease in the EDL after common nerve peroneal crush. A common peroneal nerve crush was performed and RNA was isolated at D7 (n = 9), D21 (n = 9), D30 (n = 4) and D50 (n = 4) from denervated and the contralateral control EDL muscles. In some cases, a nerve cut was performed instead of a nerve crush and tissues were collected at the D21 time point (n = 8). ***A-D,*** Gene expression for the postsynaptic gene *Muscle-specific kinase* (*MuSK, **A***), the regeneration marker *Growth-associated protein 43* (*GAP-43, **B***), and two myelin markers *Myelin protein zero* (*MPZ, **C***) and *S100 calcium binding protein B (S100B, **D**)* were used as controls to demonstrate the effectiveness of the nerve crush and how the regenerative response changes over the examined time course. ***E-F,*** Gene expression for *Neuropilin1* (*Npn1, **E***) and *Semaphorin3A* (*Sema3A, **F**)* decrease in response to nerve crush injury. *Npn1* levels return to baseline over the time course, while Sema3A remains low even at the latest time point examined. For all graphs, error bars represent the mean ± s.e and letters represent significant differences (a-b, a-e: $p < 0.0001$; b-c: $p \leq 0.001$; a-d, b-d: $p < 0.01$; b-e, a-c: $p < 0.05$).

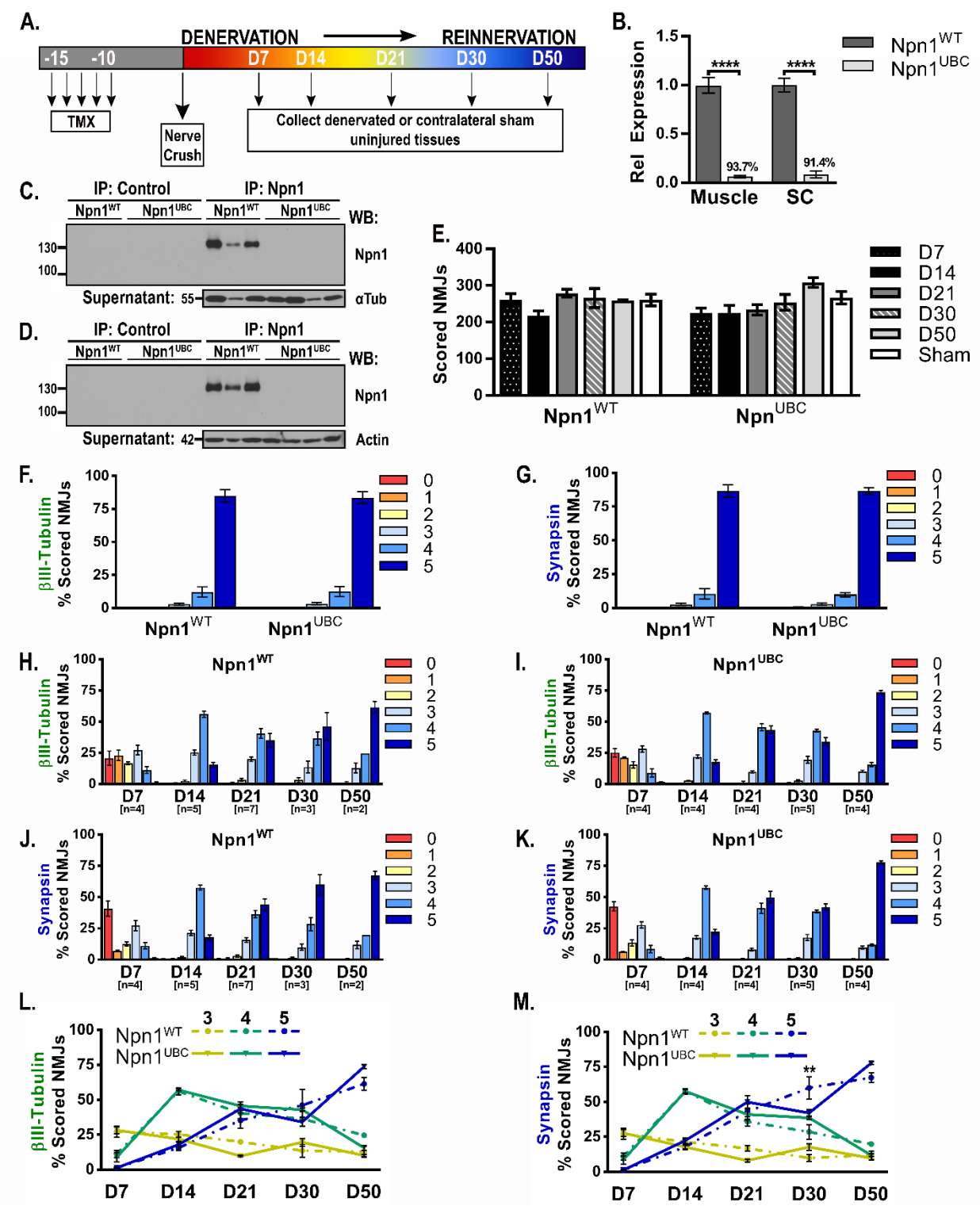

Figure 2.4. Loss of Npn1 modestly impairs NMJ reinnervation after injury.
Graphical depiction of the experimental paradigm. Tamoxifen (TMX) was administered for 5 days, followed by a 10 day rest period to allow for Cre-mediated recombination. At D0 a common peroneal crush was preformed and tissues were collected at the various time points. ***B,*** qRT-PCR was used to assess the level of *Npn1* knockdown in GP muscle and SC from all mice used to examine reinnervation in subsequent experiments. The level of *Npn1* transcript

detected in Npn1^{UBC} mice (n = 21) is graphed relative to that observed in Npn1^{WT} control littermates (n = 20) with the average percent knockdown in Npn1^{UBC} mice displayed above the bar graph. ***C-D,*** Control or Npn1 immunoprecipitation (IP), followed by immunoblotting for Npn1 was used to assess the amount of Npn1 protein in Npn1^{WT} and Npn1^{UBC} mice after TMX-mediated deletion. Representative western blots from the D30 time point demonstrate that Npn1^{UBC} mice have no detectable levels of Npn1 protein in either the GP muscle (***C***) or the whole SC (***D***). Supernatants immunoblotted for alpha-tubulin (αTub) or actin are provided as loading controls. ***E,*** Npn1 deletion does not alter the total number of scored NMJs observed at different time points after nerve crush injury (n.s., one-way ANOVA). ***F-G,*** The innervation status of sham-operated uninjured EDLs from Npn1^{UBC} (n = 4) and Npn1^{WT} (n = 4) mice was examined at the D21 time point. Scoring performed on the basis of nerve fiber (βIII-tubulin, ***F***) or presynaptic terminal (synapsin, ***G***) staining demonstrates that loss of Npn1 does not perturb the normal maintenance of the NMJ. ***H-K,*** Reinnervation following a nerve crush injury was examined in Npn1^{WT} littermate controls (***H***,***J***) and Npn1^{UBC} (***I,K***) mice. Innervation scores based on nerve βIII-tubulin staining (***H,I***) or presynaptic synapsin staining (***J,K***) produced similar trends. Despite loss of Npn1, early reinnervation (D7-D21) occurs normally. However, at D30, there appears to be a delay in motor nerve maturation as the number of NMJs scored as a '5' are decreased. This effect is only transient as reinnervation is largely complete by the D50 time point. (***L,M***) Reinnervation data was replotted using only Scores 3-5 to directly compare differences between the two genotypes. Error bars represent the mean ± s.e. **** $p \leq 0.0001$, **$p<0.01$.

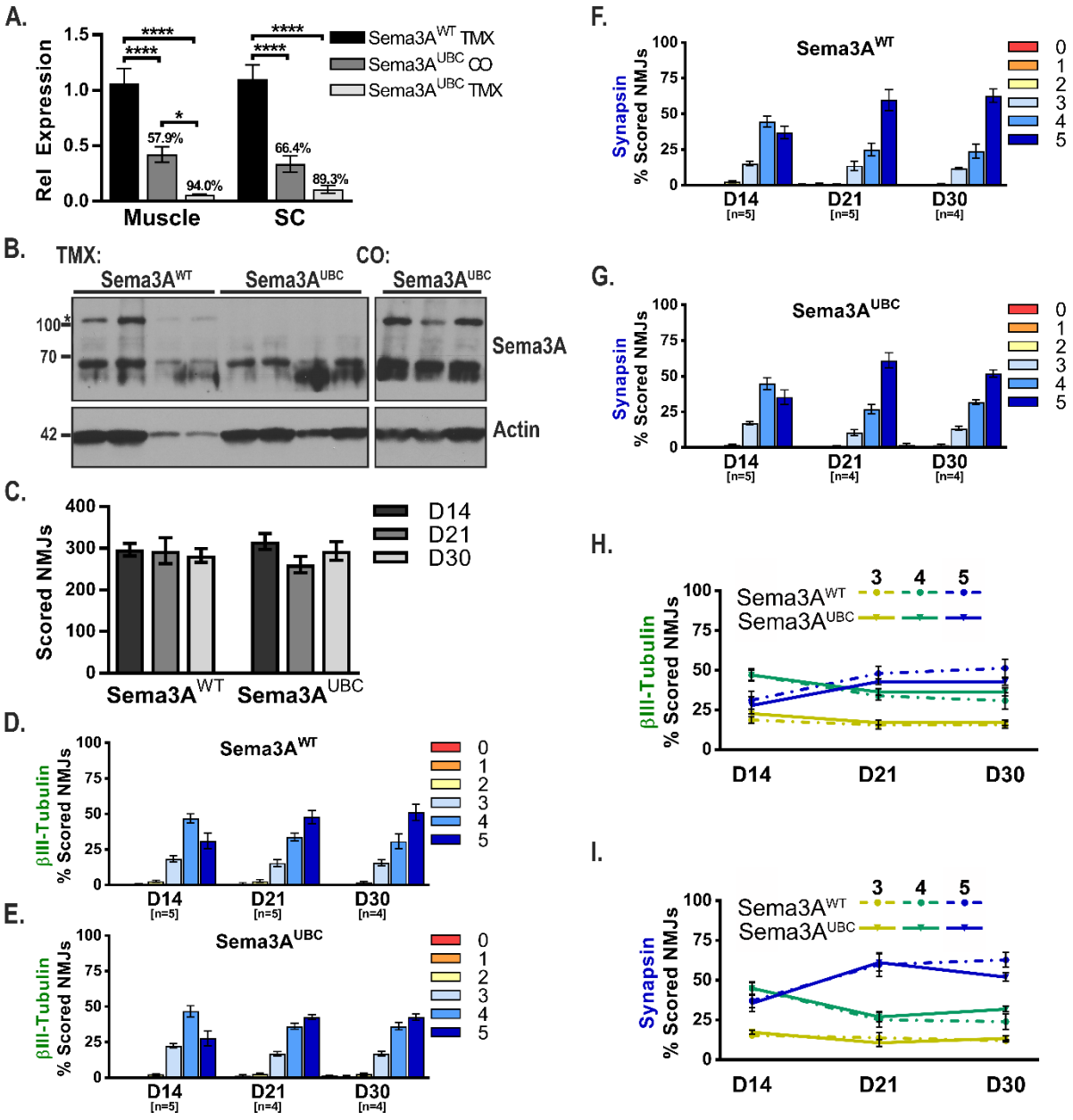

Figure 2.5. Loss of Sema3A does not impact NMJ reinnervation after injury.
A, RNA was isolated from the GP muscle and SC of mice used for subsequent reinnervation studies. The level of *Sema3A* transcript detected in Sema3A^{UBC} mice treated with corn oil (n = 10) or TMX (n = 12) is graphed relative to that observed in Sema3A^{WT} control littermates (n = 12). The average percent knockdown in Sema3A^{UBC} mice is displayed above each bar graph. ***B,*** GP muscle lysates were isolated from Sema3A^{WT} and Sema3A^{UBC} mice at various time points after nerve crush (D14-D30) and subjected to western blotting. No detectable Sema3A protein was observed after TMX-mediated deletion in Sema3A^{UBC} mice. Supernatants immunoblotted for actin are provided as a loading control. ***C,*** Loss of Sema3A does not alter the number of NMJs scored at different time points (n.s., one-way ANOVA). ***D-G,*** Reinnervation after a common peroneal crush was analyzed in Sema3A^{WT} control littermates (***D,F***) and Sema3A^{UBC} (***E,G***) mice. Innervation scores based on nerve βIII-tubulin staining (***D,E***) or presynaptic synapsin staining (***F,G***) followed similar trends. No differences in reinnervation were detected at any time point. (***H,I***) Reinnervation data was replotted using only Scores 3-5 to directly compare differences between the two genotypes. Error bars represent the mean ± s.e. **** p ≤ 0.0001, *p<0.05.

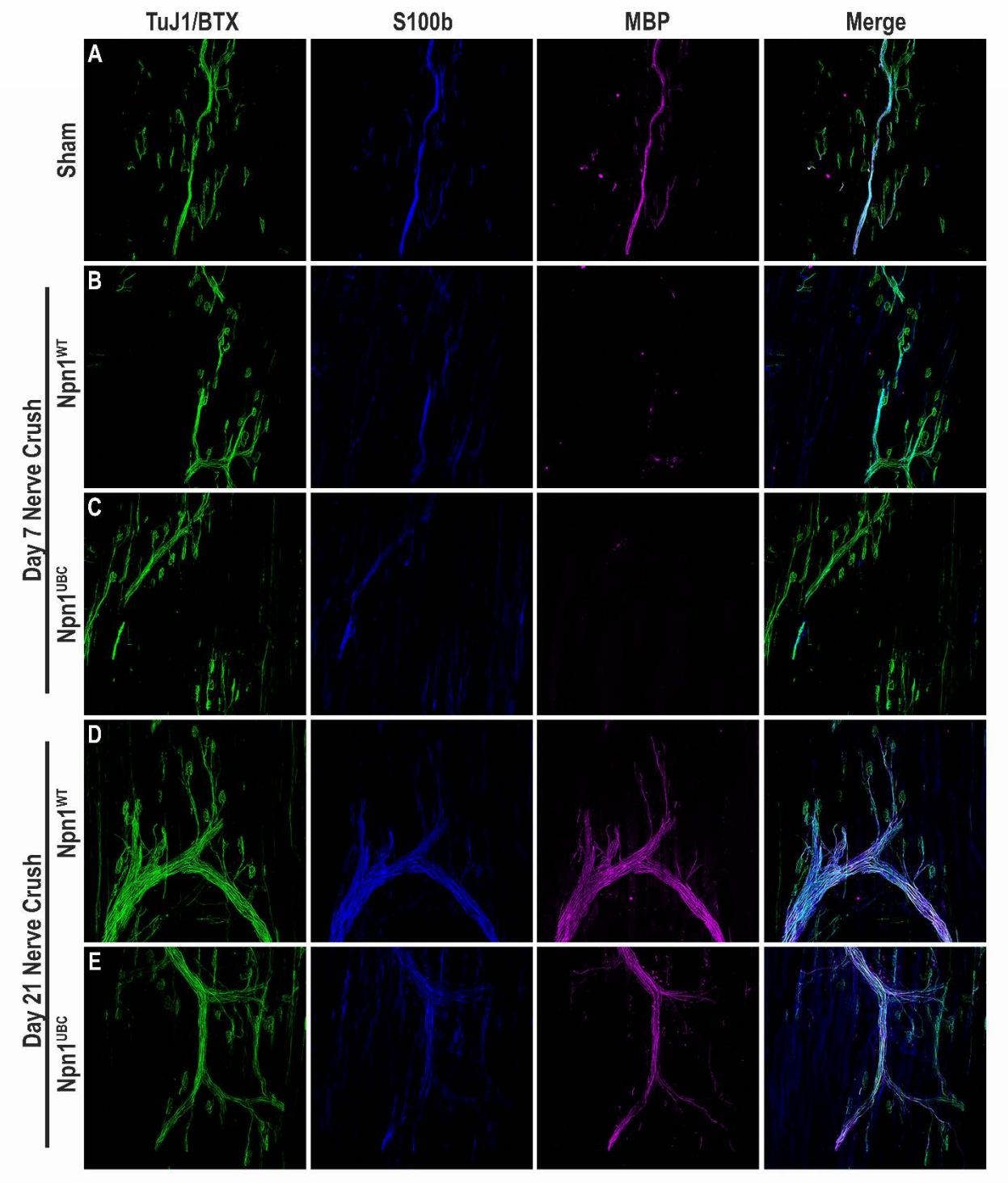

Figure 2.6. Npn1 deletion does not affect remyelination after a denervating injury.
Myelination in sham injured and denervated EDLs was examined. The nerve and endplates were visualized by staining for βIII-tubulin and BTX (green), while the myelin was visualized by staining for S100b (blue) and MBP (magenta). ***A***, Normal innervation and myelination is observed in sham injured EDL sections. ***B-C,*** At D7 after nerve crush there is a slight reduction in S100b and a near-total loss of MBP staining in both $Npn1^{WT}$ (***B***) and $Npn1^{UBC}$ (***C***) mice. ***D-E,*** Remyelination was observed to have largely taken place by the D21 time point in both $Npn1^{WT}$ (***D***) and $Npn1^{UBC}$ (***E***) mice.

CHAPTER 3: ISOLATION OF MOTOR NEURON SPECIFIC TRANSCRIPTS FROM COMPLEX TISSUES

Summary

Dysfunctions of the neuromuscular system such as spinal muscular atrophy (SMA) and amyotrophic lateral sclerosis (ALS) have complex disease etiologies. Recent evidence suggests that deficient RNA processing and trafficking may be a common mechanism underlying disease pathogenesis. Although problems associated with RNA metabolism can disrupt many different cellular processes, its impacts on local translation has gained increasing attention. Over the past 20 years, local translation in specialized compartments, such as axons, has become increasingly appreciated as a mechanism whereby proteins can be generated in a spatially and temporarily restricted manner.

To better understand the repertoire of mRNA transcripts utilized by motor neurons *in vivo*, we have utilized the RiboTag transgenic mouse model developed by Sanz et al., 2009 to specifically isolate ribosomal complexes and their associated mRNA transcripts. In this model, an HA epitope tag is encoded onto Ribosomal protein RPL22 (RPL22) in a Cre-recombinase (Cre) dependent manner. As a core member of the ribosome particle, $RPL22^{HA}$ is incorporated into the ribosome complex such that the entire complex and any associated mRNA can be immunoprecipitated with an HA antibody.

Here, motor neuron specific RPL22^{HA} expression was achieved by crossing the RiboTag mouse line with *Choline acetyltransferase* (*ChAT*)-*Cre* mice. As expected, RiboTag;*ChAT-Cre* mice exhibited strong HA^{+} immunoreactivity in motor neuron cell bodies, while immunoprecipitation of ribosomal complexes led to the enrichment of motor neuron specific transcripts. Next, we used the RiboTag model to examine local translation in motor axons. Although we could detect a low level of background RPL22^{HA} expression in *Cre*-negative mice, there was a significant Cre-dependent increase in RPL22^{HA} protein and associated RNA in motor axons that innervate the skeletal muscle. While this caveat made it more challenging to purify motor axon specific ribosomal complexes, we were able to identify genes enriched within the axonal compartment by RNA-Seq. Finally, application of this technology to models of sciatic nerve crush and neurodegeneration in ALS highlight how it can be used to interrogate motor neuron specific changes in gene expression. Taken together, this research demonstrates how future use of this model can lead to unique insights into how motor neurons respond to a changing environment.

Introduction

Traditional methods commonly used to investigate cell type specific changes in gene expression include *in situ* hybridization, laser capture microdissection (LCM), and enzymatic dissociation followed by fluorescence-activated cell sorting (FACS). Although these methodologies have provided important insights into gene regulation, there are limitations associated with their usefulness to assess gene expression in complex tissues (Jung and Jung, 2016). While *in situ* hybridization allows for the careful assessment of RNA localization, it is not amenable to high-throughput profiling to

identify novel transcripts and it is less quantitative than other methods. Conversely, LCM and FACS sorting can be used on a broader scale for gene discovery, but each of these techniques come with their own challenges. Contamination by the proximity of adjacent cells can occur with LCM and the enzymatic dissociation process required for FACS purification can alter gene expression profiles. Additionally, an added challenge posed by FACS purification of certain neuronal populations is that axotomy combined with the stress of cell sorting often greatly reduces cell survival. Finally, and perhaps most importantly, the transcript numbers for many genes are uncorrelated with protein expression or are translated in a subcellular domain specific manner. These combined limitations create a ceiling for understanding the impacts of gene expression in specific populations and within subcellular compartments.

To overcome these challenges, methods were developed to allow for the purification of ribosomal complexes from specific cell types. Translating Ribosome Affinity-Purification (TRAP) relies on genetic mouse models to introduce an epitope tag such as enhanced green fluorescent protein (eGFP) or hemagglutinin (HA) onto a ribosomal protein. When coupled with cell-type specific Cre-recombinase (Cre) expression, this provides a way to target specific cell populations (Heiman et al., 2008; Sanz et al., 2009; Jung and Jung, 2016). An antibody against the epitope tag can be used to immunoprecipitate tagged ribosomal complexes from whole tissues, thereby allowing for the isolation of actively translating mRNA transcripts. These purified RNAs can then be subjected to a wide array of downstream analyses.

Here, we used RiboTag TRAP mice to explore motor neuron-specific gene translation *in vivo*. In this model, ribosomal protein L22 (RPL22) is genetically modified

to express RPL22-HA ($RPL22^{HA}$) protein in a Cre-dependent manner (Sanz et al., 2009). As a member of the 60S ribosomal subunit, $RPL22^{HA}$ is then incorporated into actively translating ribosomal complexes and can be immunoprecipitated with an HA antibody. To restrict $RPL22^{HA}$ expression to spinal motor neurons, the RiboTag mouse line was crossed with mice that express *Cre* under the *Choline acetyltransferase* (*ChAT*) promoter (Rossi et al., 2011).

In characterizing this model, we were able to confirm that RiboTag;*ChAT-Cre* mice exhibit strong HA immunoreactivity in spinal motor neurons. Furthermore, we demonstrate that high-quality, motor neuron-specific mRNA transcripts can be isolated from HA-tagged ribosomes immunoprecipitated from spinal tissue. In addition to analyzing transcript expression from cell bodies in the spinal cord, we also asked whether this model could be used to examine local translation in motor axon terminals. Over the past decade this has emerged as a key regulatory mechanism used by a wide variety of neurons to rapidly respond to a diverse array of environmental signals (Kar et al., 2017). Although we found there is a low level $RPL22^{HA}$ expression in control mice, there is a clear *ChAT-Cre* dependent increase in $RPL22^{HA}$ protein and associated mRNA isolated from distal motor axons.

Altogether, this work demonstrates the feasibility of using this methodology for novel gene discovery and as a system to investigate how motor neurons respond to injury and neurodegeneration. As such, our data strongly suggests that this technology can be used as a powerful tool to gain a better insight into how motor neurons respond to changes in their environment.

Results

As the interface between the motor and skeletal muscle systems, the neuromuscular junction (NMJ) is principally responsible for the ability of organisms to orchestrate body movements. In this system, somatic motor neuron cell bodies located in the ventral horn of the spinal cord integrate higher-order information and, upon activation, send an action potential down the motor axon that ultimately is translated into muscle contraction. To examine somatic motor neuron gene expression, we crossed RiboTag homozygous mice ($Ribo^{HO}$) to the *ChAT-Cre* mouse line. ChAT is an enzyme necessary for the production of acetylcholine (ACh), the principle neurotransmitter utilized by somatic motor neurons. Therefore, we expected this strategy to drive strong $RPL22^{HA}$ expression in all cholinergic neurons, including motor neurons.

Spinal cords from mice heterozygous for the RiboTag allele and either *ChAT-Cre*$^{+}$ or *ChAT-Cre*^{WT} ($Ribo^{HET}$;$ChAT^{+}$ and $Ribo^{HET}$;$ChAT^{WT}$) were isolated and stained with various markers to characterize $RPL22^{HA}$ expression (Figs. 3.1 to 3.3). First, four major populations of $RPL22^{HA}$ cells were identified by staining $Ribo^{HET}$;$ChAT^{+}$ spinal cord sections with HA (red), the neuronal marker NeuN (Green), and ChAT (blue). As expected, $NeuN^{+}ChAT^{+}$ somatic motor neurons in the ventral horn were clearly observed to be HA^{+} (Fig. 3.1*E*). Additionally, two other cholinergic populations were identified through $RPL22^{HA}$ expression. HA^{+} pre-motor interneurons, previously described to play a neuromodulatory role during locomotive behavior (Zagoraiou et al., 2009), were found around the central canal (Fig. 3.1*B*), while HA^{+} preganglionic visceral motor neurons that project axons to sympathetic ganglia of the autonomic nervous system (Stifani, 2014) were found in the lateral horn (Fig. 3.1*C*). Finally, we also

observed an unexpected but rare population of $HA^{+}NeuN^{+}ChAT^{-}$ cells in the ventral horn of the spinal cord (Fig. 3.1*D*). Although the origin and function of these cells is unclear, we believe they might represent a population of interneurons that were cholinergic at some point during development, but have since stopped producing acetylcholine.

Next, we set out to more thoroughly examine $RPL22^{HA}$ expression in somatic motor neurons. Similarly to that described above, spinal cord sections from $Ribo^{HET};ChAT^{WT}$ (Fig. 3.2*A-D*) and $Ribo^{HET};ChAT^{+}$ (Fig. 3.2*E-H*) mice were stained with HA (red), the neuronal marker NeuN (Green), and ChAT (blue). Representative spinal cord hemisections demonstrate that both $Ribo^{HET};ChAT^{+}$ and control littermates exhibit strong $ChAT^{+}$ staining in the ventral horn; however, $RPL22^{HA}$ expression is only observed in $Ribo^{HET};ChAT^{+}$ mice (Fig. 3.2*G* vs. Fig. 3.2*C*).

Somatic motor neurons can further be classified into two main populations. Alpha motor neurons (αMNs) innervate extrafusal muscle fibers at the NMJ and are therefore responsible for the initiation of muscle contraction, while gamma motor neurons (γMNs) innervate intrafusal muscle fibers at the muscle spindle and are necessary for proprioceptive feedback as the muscle is stretched during contraction (Hulliger, 1984). Interestingly, these two populations can be readily distinguished from each other by size and NeuN expression (Friese et al., 2009). More specifically, αMNs are $NeuN^{+}ChAT^{+}$ and have larger somal diameters (Fig. 3.2*I-L,* arrowhead), while γMNs are $NeuN^{-}ChAT^{+}$ and exhibit smaller somal diameters (Fig. 3.2*I-L,* asterisk). To quantify the relative proportion of $RPL22^{HA}$ expression in $Ribo^{HET};ChAT^{WT}$ and $Ribo^{HET};ChAT^{+}$ mice, serial sections through the lumbar spinal cord were analyzed. Overall, mice of both genotypes contained a similar percentage of αMNs (~80%) and γMNs (~20%) in the ventral horn of

the spinal cord. Importantly, while almost every motor neuron from Ribo^{HET};ChAT^{+} mice were HA^{+}, very few cells (αMNs 2.55 ± 0.722, γMNs: 0.59 ± 0.304) were marked as HA^{-}. Additionally, no inappropriate HA expression was observed in any of the Ribo^{HET};ChAT^{-} mice (Fig. 3.2*M*).

Lastly, we co-stained spinal cord sections for RPL22^{HA} (HA antibody, red) and either glial fibrillary acidic protein (GFAP, blue, Fig. 3.3*A*-*C*) or microtubule-associated protein 2 (MAP2, green, Fig. 3.3*D*-*F*). Through the use of these two staining schemes, the absence of RPL22^{HA} staining can be appreciated in GFAP^{+} oligodendrocytes, while positive RPL22^{HA} staining can be observed extending into MAP2^{+} motor neuron dendrites (see arrowheads).

Immunoprecipitation and Isolation of Motor Neuron Specific mRNA Transcripts.

After immunohistochemical characterization of RPL22^{HA} localization in motor neuron cell bodies, we next sought to examine if RPL22^{HA} protein could be detected after immunoprecipitation from spinal tissue. Whole spinal cords were collected from RiboTag^{HO};ChAT^{+} (Ribo^{HO};ChAT^{+}), Ribo^{Het};ChAT^{+}, and various wild-type (WT) mice of different genotypes (C57BL6, RiboTag^{WT};*ChAT-Cre*$^{+}$; RiboTag^{Het};ChAT^{WT}; RiboTag^{HO};ChAT^{WT}). Since all control groups behaved similarly, the results were averaged and displayed as one WT group. Western blotting following HA immunoprecipitation was then used to examine RPL22^{HA} expression. The representative western blot (Fig. 3.4*A*) demonstrates that RPL22^{HA} protein is expressed in spinal cord lysates at a level that can be detected in whole cell lysates (WCL) prior to HA immunoprecipitation. HA immunoprecipitation greatly enhances the amount of

detected RPL22^{HA} protein in the immunoprecipitated product (IP), while simultaneously depleting the levels observed in the supernatant (SUP). In addition to HA, the amount of actin detected in the supernatant was also determined and used as a loading control for each sample (Fig. 3.4*B*). Finally, for all experiments the amount of HA detected in the IP was quantified and normalized to the amount of supernatant actin. Overall, a significant and gene dose-dependent increase in HA protein can be appreciated among the various genotypes (WT, 1.00 ± 0.594; Ribo^{Het};ChAT^{+}, 19.97 ± 4.826; Ribo^{HO};ChAT^{+}, 36.85 ± 6.56) (Fig. 3.4*C*).

With evidence of successful RPL22^{HA} protein isolation, we next examined whether RNA could be obtained from isolated ribosomal complexes. Spinal cords from WT, Ribo^{Het};ChAT^{+}, and Ribo^{HO};ChAT^{+} mice were lysed, immunoprecipitated with an HA antibody, and associated RNAs were purified. Isolated RNA was then analyzed by a Bioanalyzer to determine RNA quality (Fig. 3.5*A*) and concentration (Fig. 3.5*B*). High quality and intact RNA was routinely isolated from all mice analyzed (average RIN values for WT, 8.26 ± 0.661; Ribo^{Het};ChAT^{+}, 9.10 ± 0.280; Ribo^{HO};ChAT^{+}, 8.18 ± 0.282). Furthermore, similar to RPL22^{HA} protein, we observed a gene dose-dependent amount of RNA was isolated from immunoprecipitated ribosomes (WT, 2.24 ± 0.442; Ribo^{Het};ChAT^{+}, 17.09 ± 6.658; Ribo^{HO};ChAT^{+}, 49.15 ± 3.398).

Next, we sought to validate that immunoprecipitated RNA contained transcripts that are specific to motor neurons. To do this, RT-qPCR was used to assess the expression of positive and negative control genes expected to be enriched or absent in the IP. *ChAT* expression was used as the positive control, while the interneuron marker *calbindin* and the oligodendrocyte marker *2'3'-cyclic-nucleotide 3'-phosphodiesterase*

(*CNPase*) were used as negative controls (Lappe-Siefke et al., 2003; Merkulyeva et al., 2015). Expression data was then analyzed and displayed using two different analyses. The percent input (Fig. 3.5*C*) shows the expression of each gene in the IP as a percentage of that observed in the input. Interestingly, both $Ribo^{Het}$;$ChAT^{+}$ and $Ribo^{HO}$;$ChAT^{+}$ showed a similar level *ChAT* enrichment after $RPL22^{HA}$ IP (23.62 ± 5.147 vs. 22.9725 ± 2.738, respectively), although $Ribo^{Het}$;$ChAT^{+}$ mice exhibited a higher degree of variability. Furthermore, no enrichment of either *calbindin* or *CNPase* transcript was observed in mice of any genotype. In addition to percent input analysis, RT-qPCR data was also graphed as the fold enrichment of transcript detected in $RiboTag^{+}ChAT^{+}$ mice ($Ribo^{Het}$;$ChAT^{+}$ and $Ribo^{HO}$;$ChAT^{+}$ samples are averaged into one group) over that observed in WT mice. Accordingly, no enrichment was observed in the input sample for any gene examined, while a dramatic upregulation of ChAT transcript (117.88 ± 17.927) was observed in the IP (Fig. 3.5*D*).

Finally, after a preliminary validation that motor neuron specific mRNA transcripts could indeed be immunoprecipitated from whole spinal cords, we sought to perform a more in-depth analysis of region-specific gene expression. To this end, spinal cords were isolated from $RiboTag^{HO}$;$ChAT^{+}$ and $RiboTag^{HO}$;$ChAT^{WT}$ ($Ribo^{HO}$) littermates and dissected into cervical (SC-C), thoracic (SC-T), and lumbar (SC-L) regions. HA immunoprecipitations were then performed from each region separately and purified RNA was subjected to Bioanalyzer analysis and RT-qPCR. Genes were selected for analysis based on previously reported patterns of region-specific expression. The experimental paradigm is diagramed in Fig. 3.6*A*, with the cervical (yellow), thoracic (blue), and lumbar (orange) regions separated into segments. The colored bars in the

schematic represent the approximate location of the different motor columns interrogated for various gene expression patterns. Importantly, Bioanalyzer analysis revealed that the amount of total RNA isolated in the WCLs of Ribo^{HO} controls and Ribo^{HO};ChAT^{+} mice was similar for all spinal cord regions examined (Fig. 3.6*B*). Furthermore, following the IP, significantly more RNA was isolated from Ribo^{HO};ChAT^{+} mice (SC-C, 357.38 ± 30.734, SC-T, 117.71 ± 26.796, SC-L, 377.38 ± 19.915) than Ribo^{HO} littermates (SC-C, 12.51 ± 7.059, SC-T, 15.79 ± 8.373, SC-L, 23.39 ± 11.197) (Fig. 3.6*C*). Additionally, significantly less RNA was isolated from Ribo^{HO};ChAT^{+} IPs isolated from the SC-T region compared to the SC-C ($p = 0.0003$) and SC-L ($p < 0.0001$) regions, which was not surprising given that the cervical and lumbar segments contain enlargements to accommodate innervation of the limbs (Fig. 3.6*C*).

Gene expression enrichment in the IP compared to the average of the corresponding WCL sample for each region was then examined (Fig. 3.6*D-M*). The two negative control genes *calbindin* (Fig. 3.6*D*) and *CNPase* (Fig. 3.6*E*) demonstrate a highly significant de-enrichment of both transcripts in the IP compared to the WCL (*calbindin*, $p \leq 0.0001$; *CNPase*, $p < 0.001$). Next, we looked at *Islet1* (*Isl1*, Fig. 3.6*G*) and *ChAT* (Fig. 3.6*G*) gene expression in the different spinal cord regions. As genes known to be globally expressed in many motor column populations, we found a significant upregulation (>10 fold, $p < 0.01$) of both genes in the IP from each region compared to the corresponding WCLs. Other genes more specific to different motor columns were then examined for regional expression patterns. *Activated leukocyte adhesion molecule* (*Alcam*) is a gene previously shown to be expressed by motor neurons of the spinal accessory column (SAC), whose cell bodies originate in the

cervical spinal cord and axons extend out to innervate muscles of the head and neck (Dillon et al., 2005). *Forkhead Box P1* (*Foxp1*) expression was chosen because it is well established as a maker of lateral motor column (LMC) motor neurons that innervate the fore- and hindlimbs (Dasen et al., 2008). Three other genes were selected for analysis because of their reported expression in the thoracic spinal cord. *Homeobox C9* (HoxC9) and *ETS variant 1* (ETV1) are reported markers of the hypaxial motor column (HMC) that innervates the axial muscles of the trunk, while *Neuronal nitric oxide synthase* (nNOS) has been found to be expressed by preganglionic visceral motor neurons that innervate sympathetic ganglia (Saito et al., 1994). Generally speaking, gene expression in the different regions of the spinal cord after $RPL22^{HA}$ IP matched what was reported in the literature. Specifically, we found *Alcam* expression was significantly elevated in the SC-C (SC-T IP, $p = 0.0018$, SC-L IP, $p < 0.0001$, WCLs, $p = 0.0002$), while no enrichment was observed in the other regions of the spinal cord (Fig. 3.6*H*). Similarly, other genes predicted to be expressed in the thoracic spinal cord showed specific increases in SC-T samples. *HoxC9* (Fig. 3.6*J*) was significantly enriched in the SC-T IP compared to the SC-L IP ($p = 0.0367$) and the WCLs ($p = 0.0127$), while *ETV1* (Fig. 3.6*K*) showed significant enrichment compared to the SC-C IP ($p = 0.0019$) and the WCLs ($p = 0.007$). Additionally, there was also a trend towards increased expression of *ETV1* in the SC-T IP compared to SC-L IP ($p = 0.075$). The same pattern was also seen for *nNOS* (Fig. 3.6*L*) expression, with enrichment only observed in the SC-T (SC-C IP, $p = 0.003$, SC-L IP, $p = 0.0002$, WCLs, $p < 0.0001$). The only gene that did not match the predicted pattern of expression was *Foxp1*, which showed no difference in the IP from any of the spinal cord regions (Fig. 3.6*I*). Although *Foxp1* is a well-established marker

for LMC motor neurons during development (Dasen et al., 2008), it is possible that we did not observe any expression after $RPL22^{HA}$ IP because it is downregulated in adult motor neurons. Finally, the last gene we examined was *Paired-like homeodomain transcription factor 2* (*Pitx2*). *Pitx2* has been characterized as a specific marker for the pre-motor cholinergic interneurons that reside near the central canal at all regions of the spinal cord (see Fig. 3.1*B*) (Zagoraiou et al., 2009). As expected, we observed a significant enrichment of *Pitx2* gene expression in all regions examined compared to the corresponding WCLs, with the highest level of expression observed in the SC-T (SC-C IP, $p = 0.070$; SC-L IP, $p = 0.0008$; WCLs, $p < 0.0001$). Taken together, our data demonstrate that this RiboTag methodology can be used not only to isolate spinal motor neuron specific mRNA transcripts *in vivo*, but can also be used for the regional analysis of specific motor columns.

Isolation of Motor Neuron Specific Ribosomal Complexes from Motor Axons.

Over the past 20 years there has been an increasing appreciation for the role of local translation in many different cell types (Willis and Twiss, 2010). This has been found to be especially true in neurons, which have highly complex cellular morphologies including extensive dendritic arborization and axons that project long distances from the cell body. The ability to regulate mRNA localization and translation provides an efficient mechanism by which proteins can be produced in a spatially and/or temporally restricted manner. We now have overwhelming evidence that many types of neurons use local protein translation in dendrites (Sutton and Schuman, 2006). Additionally, while it was originally suggested that local translation does not occur in axons, recent

studies have identified translational machinery in axons (Gonzalez et al., 2016) and transcriptome-wide axonal profiling has identified an abundance of mRNA in axons (Deglincerti and Jaffrey, 2012). While the degree of local translation in motor neuron axons has not been examined *in vivo*, several studies have observed local translation in motor axons using *in vitro* systems (Briese et al., 2016; Fallini et al., 2016).

The RiboTag;*ChAT-Cre* mouse model offers a unique opportunity to examine local translation in motor axons. First, the physical distance between motor neuron cell bodies in the spinal cord and distal axons innervating skeletal muscle allows for the isolation of mRNA transcripts from distinct locations. Second, ChAT expression within skeletal muscle is restricted to cholinergic motor neuron innervation. To examine this more closely, the *ChAT-Cre* mouse line was crossed into the *R26/CAG^{mTmG}* reporter line. In the resulting mice, in the absence of Cre, all cells ubiquitously express tdTomato. However, exposure to Cre under the *ChAT* promoter results in a switch from tdTomato to enhanced green fluorescent protein (eGFP) expression (Fig. 3.7*A*). Skeletal muscles from these mice were isolated and stained to identify where GFP-reporter expression is localized. As expected, ßIII-tubulin^{+} nerve fibers innervating motor endplates labeled by bungarotoxin (BTX) demonstrated strong colocalization with GFP staining (Fig. 3.7*B*). In contrast, sympathethic nerves that follow blood vessels are clearly labeled by ßIII-tubulin but have no detectable level of GFP staining (Fig. 3.7*C*, arrowheads). In addition to characterization with reporter mice, RT-qPCR analysis of total RNA isolated from C57BL/6 wild-type skeletal muscle did not detect *ChAT* transcript (CT values ranging from 38 to undetectable, data not shown). Taken together,

these data suggest that motor axons are the only source of $RPL22^{HA}$ detected in muscles of the RiboTag;*ChAT-Cre* model.

To examine local translation in motor axons, quadriceps (Quad) or gastrocnemius/plantaris (GP) skeletal muscle was isolated from WT mice of various genotypes (as described previously for spinal cord isolations in Fig. 3.4), $Ribo^{Het}$;$ChAT^{+}$, and $Ribo^{HO}$;$ChAT^{+}$ mice. Individual muscles were lysed and subjected to HA immunoprecipitation followed by immunoblotting for $RPL22^{HA}$ protein. The representative western blot (Fig. 3.8*A*) demonstrates that while HA protein can be detected in skeletal muscle, there is an apparent leakiness in $RiboTag^{Het}$;$ChAT^{WT}$ and $RiboTag^{HO}$;$ChAT^{WT}$ ($RiboTag^{+}$) control mice. Importantly, C57BL/6 WT mice and $Ribo^{WT}$;$ChAT^{+}$ contols ($Ribo^{WT}$) controls show no HA expression, even under the longest exposures. Furthermore, there is an observable *ChAT-Cre* dependent increase in the amount of $RPL22^{HA}$ detected after immunoprecipitation in two of the three $Ribo^{HO}$;$ChAT^{+}$ mice. To quantify results across multiple experiments, the amount of $RPL22^{HA}$ protein in the IP was then normalized to the amount of α-tubulin (αTub) in the corresponding supernatant. Although there is a degree of variability in the amount of $RPL22^{HA}$ present in motor axons innervating the Quad (Fig. 3.8*B*) and GP (Fig. 3.8*C*) muscles, there is a specific and significant increase in $Ribo^{HO}$;$ChAT^{+}$ mice compared to the other genotypes examined.

Next, we asked whether associated RNA could be isolated from $RPL22^{HA}$ tagged ribosomal complexes from motor axons innervating muscle tissue. Similar to that described above, RNA was purified after HA immunoprecipitation and subjected to Bioanalyzer analysis. Although RIN values were slightly reduced compared to what was

observed in the spinal cord (Fig. 3.5*A*), high quality RNA was routinely isolated from all genotypes examined ($Ribo^{+}$, 7.44 ± 0.556; $Ribo^{HET}$;$ChAT^{+}$, 7.314 ± 0.503; $Ribo^{HO}$;$ChAT^{+}$, 7.36 ± 0.260, Fig. 3.9*A*). Additionally, differentiating between the two different control groups ($Ribo^{WT}$ and $Ribo^{+}$) revealed that there were significantly lower RIN values observed in the absence of the RiboTag allele.

Finally, similar to that observed for $RPL22^{HA}$ protein isolated from motor axons, the amount of RNA enriched by immunoprecipitation was only apparent in $Ribo^{HO}$;$ChAT^{+}$ mice. The amount of isolated RNA across various experiments was analyzed as the raw concentration given by the Bioanalyzer (Fig. 3.9*B*) and as the fold enrichment of RNA in $Ribo^{HET}$;$ChAT^{+}$ and $Ribo^{HO}$;$ChAT^{+}$ mice over WT samples run on the same day (Fig. 3.9*C*). Graphing the fold enrichment helps to control for trial to trial variability in the amount of RNA associated with control IPs and demonstrates there is indeed a significant enrichment of RNA associated with isolated ribosomal complexes in $Ribo^{HO}$;$ChAT^{+}$ mice.

Novel Gene Discovery from Motor Neuron Cell Bodies and Axons

We next wanted to determine whether RNA sequencing (RNA-Seq) could be performed on RNA isolated from $RPL22^{HA}$ immunoprecipitated ribosomes to identify novel transcripts produced by motor neuron cell bodies and/or axons. To this end, RNA associated with ribosomal complexes was isolated from $Ribo^{HO}$ and $Ribo^{HO}$;$ChAT^{+}$ spinal cord or muscle tissues (Fig. 3.10*A*). After limited rounds of cDNA amplification, sequencing was performed using the Illumina Hi-Seq platform. Raw sequencing data then underwent alignment and differential expression analysis. HTSeq Count

Assignments and Star Alignment Scores were used to demonstrate that samples contained good quality reads that aligned to the reference sequence (data not shown). For differential gene expression analysis, conditions were set to remove genes with less than 10 read counts in all conditions. Next, limits on the adjusted p-value (<0.01), false discover rate (<0.01), and log2FoldChange (>2) were imposed. Differential gene expression comparing 100 transcripts found after HA IP in the $Ribo^{HO}$;$ChAT^{+}$ group (IP) and the $Ribo^{HO}$ group (Ctl IP) are displayed in the heat maps (Fig. 3.10*B*-*C*). In addition to IP samples, WCL RNA was isolated before the HA immunoprecipitation and was also used as a control group. Heat maps comparing transcripts isolated from cell bodies in the spinal cord (SC, Fig. 3.10*B*) and axons from the GP muscle (Fig. 3.10*C*) illustrate a hierarchical clustering among sample types, with the IP and WCL appearing more similar to one another than to the Ctl IP. Additionally, in samples isolated from the SC, there is a clear enrichment of genes expressed in the IP (dark blue) that are not observed in the Ctl IP (light green). Furthermore, while some genes enriched in the IP are detected at lower levels in the WCL, there is also evidence that $RPL22^{HA}$ immunoprecipitation allowed for the detection of motor neuron specific transcripts that were not observed in the WCL (see black bar in Fig. 3.10*B*). While patterns of enrichment in transcripts isolated from the GP muscle (Fig. 3.10*C*) are not as dramatic in the heat map, volcano plots were also used to examine enrichment in the IP versus the Ctl IP (Fig. 3.11*A*-*B*). In analysis from the SC (Fig. 3.11*A*) and GP (Fig. 3.11*B*), genes enriched in the Ctl IP have a negative log2FoldChange (skewed to the left), while genes enriched in the IP have a positive log2Fold Change (skewed to the right). Importantly, more transcripts with lower p-values (more significant) were observed

skewing to the right, indicating that the IPs from both tissue types were enriched relative to that observed in the Ctl IPs. Lastly, the total number of genes found to be enriched in motor neuron cell bodies verses axons was compared. Overall, 1066 genes were found to be specific to motor neurons in the spinal cord, while 114 axonally located genes were identified from the muscle (Fig. 3.11*C*). Of the two groups of transcripts identified, 24 were found to be expressed by both compartments.

After differential gene expression, gene ontology (GO) and Kyoto Encyclopedia of Genes and Genomes (KEGG) analyses were performed to further characterize genes expressed by motor neuron cell bodies and axons. First, transcripts enriched in motor neuron cell bodies over the Ctl IP were analyzed. GO enrichment analysis (Fig. 3.12) demonstrates that many of the overrepresented categories belong to metabolic processes, while axon development and axonogenesis were also represented. KEGG pathways analysis was also performed to show higher-order relationships (Fig. 3.13*A*-*B*). The top represented pathways are displayed by significance (Fig. 3.13*A*) and relationally to one another in a network diagram (Fig. 3.11*B*). Interestingly, genes associated with oxidative phosphorylation and with different forms of neurodegeneration (Huntington's, Parkinson's, and Alzheimer's disease) were over represented within the data set. Furthermore, the relational analysis demonstrates that each of those categories are directly interrelated with each other. Taken together, the GO enrichment and KEGG pathways analyses highlight metabolic processes as one the core biological pathways integral to proper motor neuron function. Additionally, the finding that motor neuron specific genes are associated with various forms of neurodegenerative disease is also intriguing as pathogenesis in motor neuron diseases such as amyotrophic lateral

sclerosis (ALS) has been linked to oxidative stress and mitochondrial damage (Sas et al., 2007; Johri and Beal, 2012).

Next, the KEGG pathways analysis was performed on transcripts identified from motor neuron cell bodies versus axons. This relational analysis identified significantly overrepresented pathways from both data sets, where genes enriched in cell bodies are shown in green and axonally localized genes are shown in red (Fig. 3.14). Similar to that observed in motor neuron cell bodies alone, oxidative phosphorylation and various neurodegenerative pathways were found to be overrepresented. However, comparing genes between the cell body and axonal compartments also led to the identification of other KEGG categories including the synaptic vesicle cycle, cholinergic synapse, and various signaling pathways. Furthermore, from this analysis cell bodies were observed to express many genes known to be expressed by motor neurons (i.e. the cholinergic markers *ChAT* and *VAChT* (*Slc18a3*) and neurofilament proteins like *Nefm*, *Prph*, *Nefh* and *Nefl*). Finally, some genes specific to the axonal compartment were also identified, including *Dynein axonemal intermediate chain 1* (*Dnaic1*), *Wnt7b*, a voltage-gated potassium channel (*Kcnq3*), the opioid receptor *Oprm1*, and a gene associated with the cytoskeleton *Profilin 4* (*Pfn4*). Importantly, future localization studies will be required to explicitly determine whether these are indeed locally translated in motor axons.

Applying the RiboTag Technology to Investigate How Motor Neurons Respond to Injury and Disease.

After demonstrating that this RiboTag methodology can be applied to investigate motor neuron specific gene expression, we next asked whether it was sensitive enough

to detect changes associated with either an acute injury or in chronic neurodegeneration. First, a sciatic nerve crush model was used to examine if an acute trauma could trigger detectable gene expression changes in spinal motor neuron cell bodies. To this end, the sciatic nerve of Ribo^{HO} control littermates and Ribo^{HO};ChAT^{+} mice were crushed at the mid-thigh level, while the contralateral leg was left uninjured (UNI). The lower 2/3 of the lumbar spinal cord was then isolated 7 days (D7) after the nerve crush and the injured and contralateral uninjured hemispheres were separated. D7 and UNI lumbar cords were then processed for RPL22^{HA} IP separately and the isolated RNA was analyzed by Bioanalyzer and RT-qPCR. Like that observed in our earlier experiments, a similar amount of total RNA was isolated from UNI and D7 spinal cord WCLs regardless of genotype (Fig. 3.15*A*). Furthermore, RPL22^{HA} IP only resulted in the isolation of an appreciable amount of RNA from Ribo^{HO};ChAT^{+} mice but not Ribo^{HO} controls ($p < 0.01$, Fig. 3.15*B*). Next, RT-qPCR was used to analyze how various genes changed in the WCL (left column, Fig. 3.15*C,E,G,I*) or after IP enrichment (right column, Fig. 3.15*D,F,H,J*). Interestingly, apart from the *p75 neurotrophin receptor* (*P75*, Fig. 3.15*G*), no injury-induced changes in gene expression could be detected in the WCL 7 days after nerve crush. However, the enrichment of motor neuron specific transcripts following RPL22^{HA} IP allowed for the sensitive detection of injury induced changes in gene expression. More specifically, a significant reduction in *ChAT* transcript was detected at the D7 time point compared to the UNI control ($p = 0.0038$, Fig. 3.15*D*), while *GAP43* (Fig. 3.15*F*), *P75* (Fig. 3.15*H*), and *brain derived neurotrophic factor* (*BDNF*, Fig. 3.15*J*) were all specifically increased at the D7 time point (*GAP43*, $p = 0.0001$; *P75*, $p = 0.0015$; *BDNF*, $p = 0.0016$) in accordance with previously published

studies that used *in situ* hybridization (Chong et al., 1992; Hayes et al., 1992; Ikeda et al., 2001; De Winter et al., 2006; Meeker and Williams, 2014).

In addition to assessing injury-induced changes in motor neuron cell bodies, we also asked whether sciatic nerve crush injury could alter local translation in motor axons. Interestingly, in other neuronal cell types it has been widely appreciated that there is a low, basal level of local translation in uninjured axons that can be dramatically upregulated in response to injury (Twiss and Shooter, 1995; Willis and Twiss, 2010). To investigate changes in local translation after sciatic nerve crush we used $RPL22^{HA}$ protein expression as a readout for changes in translational activity. $Ribo^{HO}$ controls and $Ribo^{HO}$;$ChAT^{+}$ mice underwent a common peroneal nerve crush (see Chapter 2 for description of this injury model). Tibialis anterior (TA) muscles were collected at D7 after crush and $RPL22^{HA}$ IPs were performed from injured and UNI muscles. Supernatant (SUP) samples were immunoblotted for αTub and synapsin as a control (Fig. 3.16*A*). The expression of both proteins was found to be regulated by nerve crush injury, with injury resulting in increased αTub and decreased synapsin expression. Next, the amount of immunoprecipitated $RPL22^{HA}$ in $Ribo^{HO}$ and $Ribo^{HO}$;$ChAT^{+}$ was examined. Most uninjured TA muscles from $Ribo^{HO}$;$ChAT^{+}$ showed little to no $RPL22^{HA}$ expression; however, at D7 after crush, the amount of $RPL22^{HA}$ protein detected in denervated TAs was dramatically upregulated compared to all other groups examined (Fig. 3.16*B-C*). Finally, in addition to assessing the amount of $RPL22^{HA}$ in the IP, we also asked if phospho-S6 Ribosomal Protein (p-S6) could be detected in the co-IP. Ribosomal protein S6 is a member of the 40S ribosomal subunit that is known to result in increased protein translation upon phosphorylation of key residues (Dufner and Thomas, 1999).

Interestingly, we found that p-S6 protein did indeed co-IP with RPL22^{HA} after nerve crush injury (Fig. 3.16*B*). Taken together, these results indicate that RiboTag technology can be used to detect small changes in motor neurons in response to peripheral injury with high sensitivity. Furthermore, an injury-induced increase in RPL22^{HA} expression, coupled with the observation that p-S6 is specifically observed in the co-IP, supports the notion that acute injuries result in an upregulation of local translation in motor axons.

Finally, to examine how motor neuron gene expression changes in the context of neurodegenerative disease, the RiboTag;*ChAT-Cre* line was crossed into the SOD1^{G93A} mouse model of ALS. The time course of disease progression in this model has been studied extensively in the past (Hegedus et al., 2007; Acevedo-Arozena et al., 2011). Briefly, young SOD1^{G93A} mice are categorized as presymptomatic because there are no signs of muscle atrophy or motor neuron cell death, although early bouts of denervation can be detected at the NMJ. As mice approach 3 months of age, they enter a symptomatic disease phase in which chronic denervation leads to increased muscle wasting and motor neuron cell death. Ultimately, by 4.5 to 5 months of age, SOD1^{G93A} mice reach a terminal phase in which they experience total hindlimb paralysis and eventual death.

In crossing the SOD1^{G93A} and RiboTag;*ChAT-Cre* mice, four genotypes were generated: SOD1^{G93A};Ribo^{HO};ChAT^{+} (ALS Ribo^{HO};ChAT^{+}), SOD1^{WT};Ribo^{HO};ChAT^{+} (WT Ribo^{HO};ChAT^{+}), SOD1^{G93A};Ribo^{HO} (ALS Ribo^{HO}), and SOD1^{WT};Ribo^{HO} (WT Ribo^{HO}). Mice were then aged to either an early symptomatic (P90) or terminal (P150) time point. While some of the work fully characterizing this line is ongoing, early studies investigating RNA isolation from motor neuron cell bodies illustrate the sensitivity of this

technique. First, lumbar spinal cords were lysed, RPL22^{HA} was immunoprecipitated, and associated RNAs were isolated and subjected to Bioanalyzer analysis. At both time points, the specificity of the RPL22^{HA} IP was demonstrated by the significant enrichment of RNA in ALS and WT Ribo^{HO};ChAT^{+} mice compared to Ribo^{HO} controls ($p < 0.01$, Fig. 3.17*A-B*). Interestingly, at the P90 early symptomatic time point we also observed a statistically significant increase in the amount of RNA isolated from ALS Ribo^{HO};ChAT^{+} mice compared to WT Ribo^{HO};ChAT^{+} controls ($p = 0.04$, Fig. 3.17*A*). Conversely, because extensive motor neuron cell death was expected at the terminal P150 time point, we hypothesized that ALS Ribo^{HO};ChAT^{+} mice would have less isolated RNA following immunoprecipitation. However, in contrast to our hypothesis, no difference in the amount of RNA isolated was observed (Fig. 3.17*B*).

Lastly, for the experiments described above, protein samples were also co-purified from the WCL and IP samples that were processed for RNA. Isolated protein from ALS and WT mice was then examined for RPL22^{HA} and p-S6 expression by immunoblotting. WCLs were analyzed for αTub and ChAT expression as loading controls (Fig. 3.18*A-B*). Additionally, HA expression in WCLs at the P90 (Fig. 3.18*C*) and the P150 (Fig. 3.18*D*) time points demonstrated that RPL22^{HA} was only detected in Ribo^{HO};ChAT^{+} mice and not Ribo^{HO} controls; however, there were no appreciable differences between ALS Ribo^{HO};ChAT^{+} and WT Ribo^{HO};ChAT^{+} mice. We also examined the levels of p-S6 in the WCL and the co-IP. While, p-S6 protein was detected in the WCLs of all mice at both time points (Fig. 3.18*E-F*), a dramatic increase in p-S6 protein was detected in ALS Ribo^{HO};ChAT^{+} mice at the P90 time point (Fig. 3.18*G*) and almost no p-S6 was found associated with RPL22^{HA} at the terminal stage (Fig. 3.18*H*).

Discussion

In this Chapter we characterized and validated the RiboTag;*ChAT-Cre* mouse model as a means of isolating spinal motor neuron specific ribosome-associated RNAs. As expected, we found that RPL22^{HA} protein was produced in a *ChAT-Cre* dependent manner by spinal motor neurons (Figs. 3.1 to 3.2) and that it could be efficiently immunoprecipitated from whole spinal cord lysates with an HA antibody (Figs. 3.4). Additionally, after HA IP, high quality RNA could be isolated from immunoprecipitated ribosome complexes (Figs. 3.5*A*-*B*). Although RPL22^{HA} protein and RNA could be isolated from RiboTag^{Het};ChAT^{+} and RiboTag^{HO};ChAT^{+} mice, we found that the total amount observed corresponded to genotype in a gene-dosage dependent manner. Furthermore, we used RT-qPCR to characterize the specificity of the mRNAs associated with the RPL22^{HA} IP (Figs. 3.5 to 3.6). Using positive (*ChAT*) and negative (*Calbindin* and *CNPase*) control genes we demonstrated that there was indeed a significant enrichment of motor neuron specific genes after RPL22^{HA} IP, but not in the WCL or RiboTag^{HO} control littermates (Figs. 3.5*C*-*D*). Finally, taking advantage of the fact that populations of motor neurons within specific motor columns are characterized by different genes, we demonstrated that region specific gene expression patterns could be analyzed using this methodology (Figs. 3.6).

Cholinergic neuron populations in the spinal cord have been described in detail and are known to include pre-motor neurons (Figs. 3.1*B*) (Zagoraiou et al., 2009) and preganglionic visceral motor neurons (Figs. 3.1*B*) (Stifani, 2014) in addition to somatic motor neurons (Figs. 3.1*E*) that innervate skeletal muscle. Therefore, it is not a surprise the *ChAT-Cre* mouse line does not provide a pure analysis of somatic motor neuron

specific gene expression. Importantly, we selected the *ChAT-Cre* mouse line because it drives strong Cre expression in somatic motor neurons while excluding most interneuron populations. To date, other methods to target Cre expression in motor neurons have included using the *Homeobox gene HB9* (*Hb9*) or *Vesicular Acetylcholine Transporter* (*VAChT*) promoters. Although *Hb9-Cre* mice have been extensively used in the past as a motor neuron specific *Cre* line, Hb9 is also involved in the specification of preganglionic visceral motor neurons (Arber et al., 1999) and more importantly is known to be expressed in a population of premotor glutamatergic interneurons (Hinckley et al., 2005). Furthermore, a recent paper has shown that using *Hb9-Cre* to drive the expression of a fluorescent reporter labeled both ventral and dorsal neurons throughout the laminae of the spinal cord (Caldeira et al., 2017). Another alternative would be to use the *VAChT* promoter, but reporter expression under *VAChT* would be expected to mirror *ChAT*. Furthermore, Cre expression in these mice has a delayed onset (at postnatal day 7) and is only detected in 40-60% of motor neurons (Misawa et al., 2003).

We could potentially bypass collection of non-somatic motor neurons by limiting tissue collection to the caudal lumbar spinal cord. This capitalizes on the fact that preganglionic visceral motor neurons are well established to only extend into the L1-L2 regions of the lumbar cord (Stifani, 2014). Additionally, pre-motor interneurons are mostly cholinergic at the more rostral levels of the lumbar spinal cord, but increasingly become glutamatergic at more caudal positions (Zagoraiou et al., 2009). Therefore, limiting isolation to lower regions of the lumbar cord would not only be more representative of motor neurons that innervate the distal hindlimb (which corresponds to

muscles that are most often used for analysis), but would also limit the contribution of other cholinergic populations.

In addition to the expected cholinergic populations, we were also able to detect a rare population cells that were RPL22^{HA+}ChAT^{-}. Although their origin is unclear, the most likely explanation for their presence is that they are an interneuron population that transiently expresses ChAT during development. Future studies to characterize their presence in regions other than the lumbar cord and determine their population sizes, locations, and function could be of interest. Altogether, given the current limitations, it will be important to supplement future analyses that identify gene expression changes in motor neurons with localization studies using *in situ hybridization* or immunostaining. Furthermore, our data highlights the need for new methods to improve Cre targeting accuracy in more defined ways (see Chapter 4).

We also observed gene expression patterns in different spinal cord regions that largely matched previously reported expression profiles used as the basis for motor column identity (Fig. 3.6). However, it is interesting to note that one gene (*Foxp1*, Fig. 3.6*I*) showed no enrichment, while some others (most notably *HoxC9* [Fig. 3.6*J*], and *ETV1* [Fig. 3.6*K*]) showed significant, but relatively low levels of enrichment. This might reflect the fact that much of our knowledge about motor column specific gene expression comes from studies of development. Therefore, genes expressed during the early specification of motor column identity may be turned off or downregulated in the adult. However, another interpretation of our results involves considering the RiboTag methodology itself. The RPL22^{HA} IP only enriches for genes that are actively associated with ribosomes. Therefore, while the total transcript abundance of a gene may be high,

if the rate of translation is low it might not appear to be greatly enriched. To distinguish between these two possibilities, future work using the RiboTag model to examine gene expression profiles during motor column specification could be performed.

After characterizing isolation of motor neuron specific transcripts from cell bodies in the spinal cord, we next asked if the RiboTag technology could be used to examine local translation in motor axons. Although our goal was to use the RiboTag mice to define an “axonal translatome” for motor neurons, limitations associated with leakiness of $RPL22^{HA}$ made this analysis challenging. Importantly, HA protein was not detected in mice that were wild-type for the $RPL22^{HA}$ knock-in allele ($Ribo^{WT}$). However, in the absence of Cre, low levels of HA protein could be detected in mice with either one or two copies of $RPL22^{HA}$ (Fig. 3.8). The likely explanation for these results is that transcriptional machinery is bypassing the stop codon intended to prevent expression of $RPL22^{HA}$ in the absence of Cre, resulting in low levels of ubiquitous $RPL22^{HA}$ transcript.

In addition to HA protein expression in the muscle in the absence of Cre, two other lines of evidence support this idea. First, analysis of the quality of mRNAs associated with ribosomal IPs in the muscle (Fig. 3.7*A*) demonstrates that transcripts isolated from $Ribo^{WT}$ mice had lower RIN values compared to the other genotypes, indicating that more of the associated RNA was fragmented and non-specifically associating with the IP. Second, we also observed the same phenomenon of a low level of HA protein expression in $Ribo^{HET}$ and $Ribo^{HO}$ after immunoprecipitation from spinal cord tissue (data not shown). This observation indicates that $RPL22^{HA}$ production in *Cre*-negative mice is not tissue specific and is likely to be inherent to all tissues of the RiboTag mouse. Taken together, the evidence presented here suggests that the

RiboTag mouse model is highly efficient at isolating tissue-specific transcripts from populations of cells in which the Cre-driven $RPL22^{HA}$ signal is expressed at high levels relative to background (i.e. for isolation of transcripts from motor neuron cell bodies). However, in situations where the expected level of transcripts is minute relative to total size (i.e. isolation of transcripts from motor axons in skeletal muscle), detecting the specific signal over noise becomes increasingly challenging.

Despite finding these limitations in the RiboTag methodology, we were able to detect significant *ChAT-Cre* dependent increases in $RPL22^{HA}$ protein (Fig 3.8) and mRNA (Fig 3.9) from muscle. Furthermore, bioinformatic analysis demonstrated that by using $Ribo^{HO}$ mice as a control (Ctl IP), an enrichment of transcripts from the $Ribo^{HO}$;$ChAT^{+}$ IP group could be detected (Fig. 3.11*B*). In total, we identified 114 transcripts as enriched in motor axons, compared to 1069 enriched in motor neuron cell bodies. Importantly, these genes do not likely reflect the entire repertoire of axonally localized transcripts, but were genes significantly enriched to a level that allowed detection over the noise associated with the control IP. Furthermore, any gene identified through bioinformatic analysis (Fig. 3.14) must be validated by *in situ* hybridization to determine if transcript is actually localized within motor axons. To that end, some of the genes enriched in axons represent particularly interesting candidates for future validation. For example, *Dnaic1* and *Pfn4* are genes associated with axon transport and the cytoskeleton, which are both processes crucial to motor neuron health and survival (Williamson and Cleveland, 1999; Willis and Twiss, 2006; Maximino et al., 2014). Furthermore, another member of the Profilin family (Pfn1) has recently been linked to ALS (Wu et al., 2012; Figley et al., 2014).

Although RT-qPCR was used to demonstrate the specificity of select genes, bioinformatic analysis showed more globally that many transcripts were significantly enriched in motor neuron cell bodies after $RPL22^{HA}$ IP (Fig. 3.10 - 3.11). Both GO (Fig. 3.12) and KEGG (Fig. 3.13) analyses pointed to metabolic processes and oxidative phosphorylation as the most highly represented pathways in motor neurons. These findings are not all that surprising given that motor neurons are metabolically demanding cells and mutations that disrupt metabolism have been linked to motor neuron disease (Sas et al., 2007; Johri and Beal, 2012; Ngo and Steyn, 2015). Furthermore, among the most highly enriched transcripts were genes that have been well-associated with motor neuron identity, including: *Hb9*, *Isl1*, *Isl2*, *Lhx3*, *Lhx4*, *ChAT*, *VAChT*, and *Acetylcholine esterase* (*AChE*). Additionally, many other genes including those important for regulation of the cytoskeleton and neurotransmission were also significantly enriched.

After characterizing the RiboTag;*ChAT-Cre* mouse model, we demonstrated that it can be applied for the sensitive detection of gene expression changes after nerve crush injury (Fig. 3.15). Interestingly, apart from *p75* (Fig. 3.15*G*), changes in response to nerve crush could not be detected in the whole cell lysates. However, enrichment of motor neuron specific transcripts demonstrated that genes were both up- and down-regulated 7 days after injury. In accordance with previous studies, *GAP43*, *p75*, and *BDNF* (Fig. 3.15*F*, *H*, *J*) were all observed to increase after injury (Chong et al., 1992; Hayes et al., 1992; Ikeda et al., 2001; De Winter et al., 2006; Meeker and Williams, 2014). Furthermore, the extent of *BDNF* upregulation was comparatively small, which potentially matches previous studies that found the highest levels of *BDNF* expression

occur within one day of the initial injury during the acute phase of the response. On the other hand, *ChAT* expression levels were found to significantly decrease after injury (Fig. 3.15*D*). This finding is consistent with previous studies that have found a reduction in *ChAT* expression following nerve crush (Armstrong et al., 1991) and in ALS patients (Nagata et al., 1982). Finally, given that our gene expression analysis at the D7 time point suggests this model works effectively, future analyses including more time points will likely reveal mechanisms that govern how motor neurons respond to a peripheral injury. Another particularly interesting comparison would be between the nerve crush and nerve cut injuries. By understanding the molecular mechanisms that underlie successful and unsuccessful nerve regeneration, such a comparison might reveal novel ways to combat peripheral nerve injury to improve regenerative outcomes.

Lastly, we applied the RiboTag;*ChAT-Cre* model to neurodegeneration by crossing the RiboTag^{HO};*ChAT-Cre*$^{+}$ line with the SOD1^{G93A} mouse model. Although we have not yet examined specific gene expression alterations, early evidence suggests that we can detect more global changes in translational activity during the early symptomatic phase (P90). Specifically, there is an increase in both the amount of RNA isolated after RPL22^{HA} IP (Fig. 3.17*A*) and in the association of p-S6 with immunoprecipitated ribosomes (Fig. 3.18*G*). While it might not be surprising that there is an increase in translational activity during disease onset when motor neurons are actively trying to compensate for loss of innervation at the NMJ, our data does not match a recent study using the *ChAT*-BAC-TRAP model with SOD1^{G37R} mice (Sun et al., 2015). Interestingly, the authors found that there was a significant reduction in overall gene expression of both ribosomal components and translational machinery in

SOD1^{G37R} mice. Furthermore, in spinal cord sections, they observed an increase in phosphorylated eIF2α (p-eIF2α), which is associated with inhibition of translational activity (Raven and Koromilas, 2008).

Although we did not see signs of reduced translation at the early P90 time point, translational defects were more apparent at the terminal time point (P150). While there were no differences in the amount of isolated RNA (Fig. 3.17*B*) or RPL22^{HA} protein (Fig. 3.18*D*) detected in ALS and WT mice, we did observe a specific decrease in co-immunoprecipitated p-S6 (Fig. 3.18*H*). Though it might be expected that motor neuron cell death at the terminal time point would lead to a general decrease the amount of isolated RNA and RPL22^{HA} protein in motor neurons, our results might be interpreted in a few ways. One intriguing idea is that RPL22^{HA} protein is caught within toxic aggregates common to many models of ALS. In support of this idea, such aggregates are known to sequester protein factors that are needed for normal cell function and have been characterized to be translationally active themselves (Yasuda et al., 2013). On the other hand, our results might reflect that there are increasingly more stalled transcripts on RPL22^{HA}-tagged ribosomes. Future studies to investigate changes in motor neuron gene expression at the P90 and P150 time points, in addition to histological studies looking at the level of RPL22^{HA}, p-S6, and eIF2α will aid in deciphering how translational activity is altered in the face of neurodegeneration.

Taken together, the work presented in this chapter represents a detailed characterization and demonstration of how the RiboTag model can be applied to the *in vivo* study of motor neuron gene expression. Furthermore, by pushing the detection limits of this model, we have found that low levels of nonspecific RPL22^{HA} are produced

in a Cre-independent fashion. Despite this limitation, by using appropriate controls we identified putative motor axon transcripts that can be characterized in future experiments. Finally, by applying the RiboTag;ChAT system to models of nerve crush injury and neurodegeneration we highlight the value that this model can serve in increasing our understanding of how motor neurons respond to changes in their environment. Furthermore, through this process, we hope to uncover novel mechanisms that can be exploited to provide new therapeutic strategies for the treatment of peripheral nerve injuries and MND.

Experimental Procedures

Animals. All housing and procedures performed on mice were approved by the Institutional Animal Care and Use Committee (IACUC) of the University of Michigan. Wild-type C57BL/6J (000664), RiboTag (B6N.129-*Rpl22*$^{tm1.1Psam}$/J, 011029), *ChAT-IRES-Cre* (B6;129S6-*Chat*$^{tm(cre)Lowl}$/J, 006410), *R26/CAG*^{mTmG} (B6;129S6-*Gt(ROSA)26Sor*$^{tm1(CAG-tdTomato*,-EGFP*)/Ees}$/J, 023035) and B6.SOD1-G93A (B6.Cg-Tg(SOD1*G93A)1Gur/J, 004435) mice were obtained from Jackson Laboratories (Bar Harbor, ME). RiboTag conditional mice were crossed with *ChAT-Cre* mice to generate Ribo^{Het};ChAT^{+} and Ribo^{HO};ChAT^{+} experimental mice. Additionally, C57BL/6J mice and Ribo^{WT};ChAT^{+} mice were used as Ribo^{WT} controls, while Ribo^{Het};ChAT^{WT} and Ribo^{HO};ChAT^{WT} littermates were used as Ribo^{+} controls. Finally, for some experiments, B6.SOD1-G93A mice were crossed into the RiboTag;*ChAT-Cre* line to create a triple-transgenic line. All mice were genotyped according to publicly available protocols and both male and female mice were analyzed in similar numbers for all experiments.

Nerve Crush. Mice were deeply anesthetized with 2-3% isoflurane mixed with oxygen and the surgical site was shaved and disinfected. Two sciatic nerve crush sites were used for different experiments. In some instances, the common peroneal branch of the sciatic nerve was crushed (as described and characterized in Chapter 2), while for other experiments the sciatic nerve was injured at the mid-thigh level to denervate a larger region of the hindlimb. For both crush sites, a small incision was made through the skin and overlying musculature to expose the sciatic nerve. The exposed nerve was then crushed by applying pressure with a pair of forceps for 40 sec. Following the crush procedure, the muscle was closed with a suture and the skin was sutured at the incision site. In a small number of experiments, a nerve cut was performed instead of a nerve crush. In these instances, the same procedure was performed except that a 3-5mm piece of nerve was excised as opposed to being crushed with forceps.

HA Immunoprecipitation and RNA Isolation. Tissues were harvested and snap frozen in liquid nitrogen. Homogenization and HA immunoprecipitation (IP) were largely performed as previously described by Sanz et al., 2009. Briefly, tissues were placed into IP buffer (50 mM Tris, pH 7.4, 100 mM KCl, 12 mM $MgCl_2$, 1% Nonidet P-40 [NP-40] supplemented with 200 U/mL Promega RNasin, 1 mg/mL heparin, 100 µg/mL cycloheximide, and protease inhibitor mixture [Sigma-Aldrich]) and subjected to Dounce homogenization. Samples were then rotated at 4°C for 15-20 minutes followed by centrifugation at 10,000 x g for 10 min at 4°C to generate a postmitochondrial supernatant. A 50 µl aliquot of the whole cell lysis (WCL) was saved and processed

separately for protein and/or RNA analysis. The remainder of the sample was precleared with Protein G magnetic beads (25 µl of beads per 200 µl of supernatant, New England Biolabs) for 1 hour under constant rotation at 4°C. After preclearing, samples were separated from magnetic beads and incubated with HA antibody (1:150 dilution, MMS-101P, BioLegend) and toppled for 4 hours 4°C. Finally, Protein G magnetic beads were added and allowed to incubate under rotation overnight. The following day, samples were placed on a magnetic rack and supernatants were collected. The IP product associated with the magnetic beads was then washed three times in a high salt buffer (50 mM Tris, pH 7.4, 300 mM KCl, 12 mM $MgCl_2$, 1% NP-40 supplemented with 100 µg/mL cycloheximide). RNA associated with the HA IP was then isolated using the RNeasy Plus Micro Kit (Qiagen) per manufacturer instructions.

Bioanalyzer Analysis, cDNA Preparation, and qRT-PCR. The concentration of isolated RNA was determined by running samples on a 2100 Bioanalyzer Instrument (Agilent Genomics). cDNA was then synthesized with the remainder of the RNA sample (~12 µl) using the Superscript III First-Strand Synthesis SuperMix kit (Invitrogen) and subsequent RT-qPCR was performed using a 7900HT Fast Real-Time PCR System (Applied Biosystems) with the appropriate primer set (Table 3-1) and FastStart Universal SYBR Green Master Mix (Roche).

HA Immunoprecipitation for Western Blotting. Muscle or spinal cord samples were dissected and placed into immunoprecipitation buffer (10% glycerol, C0mplete protease inhibitors (Roche), and sodium vanadate in Tris buffered saline (TBS), pH 6.8). Tissues

were homogenized with the Tissue Lyser II (Qiagen) set at 30 Hz for 5min. Samples were then detergent extracted by the addition of nonidet p-40 (1% final concentration) followed by constant rotation for 30 min at 4°C and insoluble material was removed by centrifugation for 5 min at maximum speed in a microfuge. Before HA immunoprecipitation (IP), samples were first precleared with Protein G agarose beads (Roche) for 1 hr before the HA IP was performed overnight with HA antibody (1:150 dilution, MMS-101P, BioLegend) and Protein G beads. For all incubations, samples were left under constant rotation at 4°C. The next day samples were lightly centrifuged (5000 rpm, 5 min) and the supernatant was collected and denatured in 2x sodium dodecyl sulfate (SDS) sample buffer (20% glycerol, 4% SDS, 1% β-mercaptoethanol, and bromophenol blue in TBS, pH 6.8) by heating for 10 min at 100°C. Meanwhile, the immunoprecipitated product was washed three times with immunoprecipitation buffer followed by denaturation in the same manner as described for the supernatants.

Protein Isolation after RNA Lysis and Processing. In some instances, protein was co-purified with RNA isolated using the RNeasy Plus Micro Kit (Qiagen). Once RNA binds to the RNA-binding cup, protein in the flow-through was precipitated with ice-cold acetone for 30 min on ice. Samples were then centrifuged for 10 min at max speed to pellet the protein precipitate. The protein was then washed with 100% ice-cold ethanol, centrifuged again, and resuspended in water. Finally, the protein was denatured by adding an equal volume of 2x SDS sample buffer and heating for 10 min at 100°C.

Immunoblotting. All samples were resolved on a 12 or 14% (SDS)-polyacrylamide gel electrophoresis (SDS-PAGE) gel and transferred to polyvinylidene fluoride (PVDF) membranes. Membranes were blocked in 4% Milk in TBS-T (Tris buffered saline, pH 7.4 and 0.1% Tween-20) for 1hr at room temperature. Primary antibodies [α-Tubulin (1:30,000, T9026, Sigma-Aldrich), Actin (1:1,000, SC-1616-G, Santa Cruz), HA (1:1,000, #3724, Cell Signaling), Synapsin-1 (1:1,000, #5297, Cell Signaling), ChAT (1:1,000, AB144P, Millipore), and Phospho-S6 Ribosomal Protein (p-S6, 1:1,000, #4858, Cell Signaling)] were diluted in 3% bovine serum albumin (BSA) and incubated overnight at 4°C. The following day, membranes were washed and incubated with appropriate horseradish peroxidase (HRP)-linked secondary antibodies (1:10,000) in 3% BSA (Jackson ImmunoResearch) followed by visualization with a chemiluminescent substrate (Thermo Scientific). Western blot quantification was performed by densitometric analysis in ImageJ (NIH). The signal intensity in arbitrary units was determined for the amount of HA protein in the IP and the amount of loading control in the supernatant. After normalization to the loading control, data was also normalized to the average value calculated for the wild-type controls.

Tissue Preparation. Mice were transcardially perfused with phosphate-buffered saline (PBS) followed by 4% paraformaldehyde (PFA, Electron Microscopy Sciences). The lumbar spinal cord was then carefully dissected and post-fixed in 4% PFA at 4°C overnight. The next day tissues were washed 3x20min in PBS and soaked for at least one day in 30% sucrose at 4°C. Spinal cords were then embedded in O.C.T compound

(Tissue-Tek) and frozen at -80°C. 30µm transverse cryosections were cut using a CM1950 cryostat (Leica Biosystems).

Immunostaining. Sections were rehydrated in PBS and then antigen retrieval was performed by incubating slides in boiling 10 mM sodium citrate buffer, pH 6.0 for 3 min. After cooling slides briefly in PBS, sections were permeabilized/blocked in 0.3% TritonX-100, 1% BSA, 10% donkey serum (Jackson ImmunoResearch), and MOM blocking reagent (Vector Laboratories) for 1hr at room temperature. Slides were then incubated with primary antibodies [HA (1:100, #3724, Cell Signaling), ChAT (1:100, AB144P, Millipore), NeuN (1:100, MAB377, Millipore), Glial fibrillary acidic protein (GFAP, 1:200, ab4674, Abcam), and Microtubule-associated protein 2 (MAP2, 1:100, ab3096, Abcam)] in 0.3% Triton, 1% BSA overnight at room temperature. The following day sections were washed in PBS and stained with the appropriate secondary antibodies (Biotium) in 0.3% Triton for one hour at room temperature. After final PBS washes, slides were coverslipped with DAPI mounting medium (Southern Biotech) and imaged on a confocal microscope (Leica SP5).

cDNA Library Construction and RNA-Seq.

The purity and quality of isolated RNA was checked by Bioanalyzer. Samples were then submitted to the University of Michigan Sequencing Core for cDNA Library construction and Sequencing. Briefly, ribosomal depletion was performed with the RiboGone Mammalian Kit (#634847, Clontech). Due to differences in the quantity of isolated RNA, 60 ng of total RNA from $Ribo^{HO}$;$ChAT^{+}$ mice and 15 ng of total RNA from $Ribo^{HO}$ mice

were input into the RiboGone Kit. After ribosomal depletion, cDNA synthesis was performed with 13 rounds of amplification using the SMARTer® Universal Low Input RNA Kit for Sequencing (#634940, Clontech). Samples were then sequenced using single-end, 50 bp reads on the HiSeq 2500 System to obtain 50 to 100 reads.

Bioinformatic Analysis.

Quality was assessed with FastQC and Cutadapt was used to remove barcodes. Sequence reads were aligned to the mouse genome (mm10) using Star Aligner (version 2.5). Align statistics were then assessed with RSeQ. Reads falling inside genes were quantified with htseq-count, while reads at splice junctions were quantified by DEXseq. Differential gene expression analysis was then performed with DESeq2 and plotted with ggplot2. Heatmaps and Venn diagrams were generated using heatpmap3 and Venerable packages, respectively. Finally, GO and KEGG enrichments were performed with GO.db and ClusterProfiler.

Statistical Analysis.

All statistical analyses were performed using Prism 7 software (GraphPad). One- or two-way ANOVA was used for all analyses. Significant differences among pairwise comparisons were identified by Tukey's *post hoc* tests.

Acknowledgements

This work was supported by funding from NIH NINDS R01 NS089585 (B. Pierchala); NIH/NIDCR Tissue Engineering and Regeneration Training Grant T32-DE007057; NIH

Cellular and Molecular Biology Training Grant T32-GM007315 (J. Shadrach). We thank the University of Michigan Sequencing Core for preparing cDNA libraries and performing RNA-seq. Additionally, bioinformatic analysis was performed by Dr. Igor Ruiz de los Mozos in the laboratory of Dr. Jernej Ule. We also thank C. Donnelly and J. Hull for critical review this work.

Gene	Forward Primer (5' – 3')	Reverse Primer (5' – 3')	BP	Source
Actin	GGCTGTATTCCCCTCCATCG	CCAGTTGGTAACAATGCCATGT	154	Harvard PrimerBank
ChAT	CCATTGTGAAGCGGTTTGGG	GCCAGGCGGTTGTTTAGATACA	136	Harvard PrimerBank
Calbindin	GGCTTCATTTCGACGCTGAC	ACGTGAGCCAACTCTACAATTC	184	Harvard PrimerBank
CNPase	ACGAGTGCAAGACGCTATTC	CCGCTCGTGGTTGGTATC	242	(Sanz et al., 2009)
Isl1	TACGTGCTTTGTTAGGGATGGG	CTGCACTTGGCGCATTTGAT	81	Harvard PrimerBank
Alcam	ATGGCATCTAAGGTGTCCCCT	CTGAGTTGACAGTGTACCATCC	100	Harvard PrimerBank
Foxp1	CACCTCAGGTTATCACTCCTCA	AGCTGCAACTGTTCCTGTTGT	157	Harvard PrimerBank
HoxC9	GCAGCAAGCACAAAGAGGA	CGTCTGGTACTTGGTGTAGGG	113	(Jespersen et al., 2013)
Etv1	GGTCTGCTTGCAGTCAAGAG	GGTTTCGGAGTATGAGCTGTGT	184	Harvard PrimerBank
nNOS	AGCACCTACCAGCTCAAGGA	ATAGTGATGGCCGACCTGAG	209	Primer3
Pitx2	GAGGTGCATACAATCTCCGATA	TGCCGCTTCTTCTTGGAC	113	(Kahr et al., 2011)
GAP43	ATAACTCCCCGTCCTCCAAGG	GTTTGGCTTCGTCTACAGCGT	201	Harvard Primer Bank
P75	CAACCAGACCGTGTGTGAAC	GGAGAACACGAGTCCTGAGC	235	Primer3
BDNF	TCATACTTCGGTTGCATGAAGG	AGACCTCTCGAACCTGCCC	137	(Arthur-Farraj et al., 2012)

Table 3.1. Primer Sequences used for real-time RT-qPCR in Chapter 3.

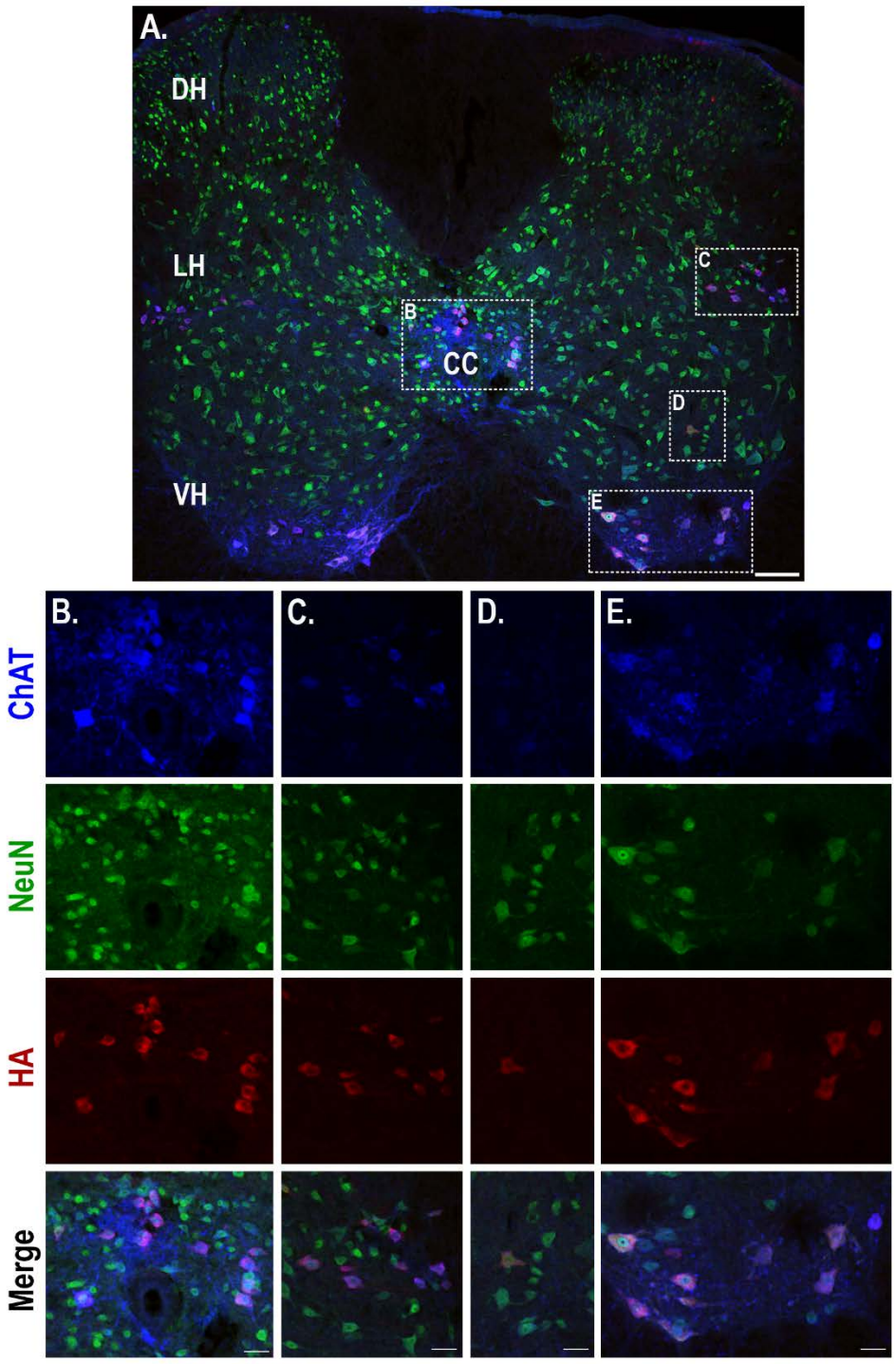

Figure 3.1. RPL22^{HA+} Cell Populations in the Lumbar Spinal Cord.
RPL22^{HA} is expressed in four major populations of cells in the spinal cord under the *ChAT-Cre* promoter. ***A,*** A representative image of a transverse section of a spinal cord is stained with ChAT (blue), NeuN (green), and RPL22^{HA} (red). The insets (B-E) illustrate regions where the different cell populations are found. ***B,*** RPL22^{HA+} cholinergic interneurons are observed around the central canal. ***C,*** Preganglionic visceral motor neurons that extend axons to the autonomic ganglia are observed in the lateral horn. ***D,*** A rare population of HA^{+}ChAT^{neg} cells are routinely observed in the upper aspect of the ventral horn. ***E,*** Somatic motor neurons are clearly observed in the ventral horn. Abbreviations: dorsal horn (DH), lateral horn (LH), ventral horn (VH), central canal (CC).

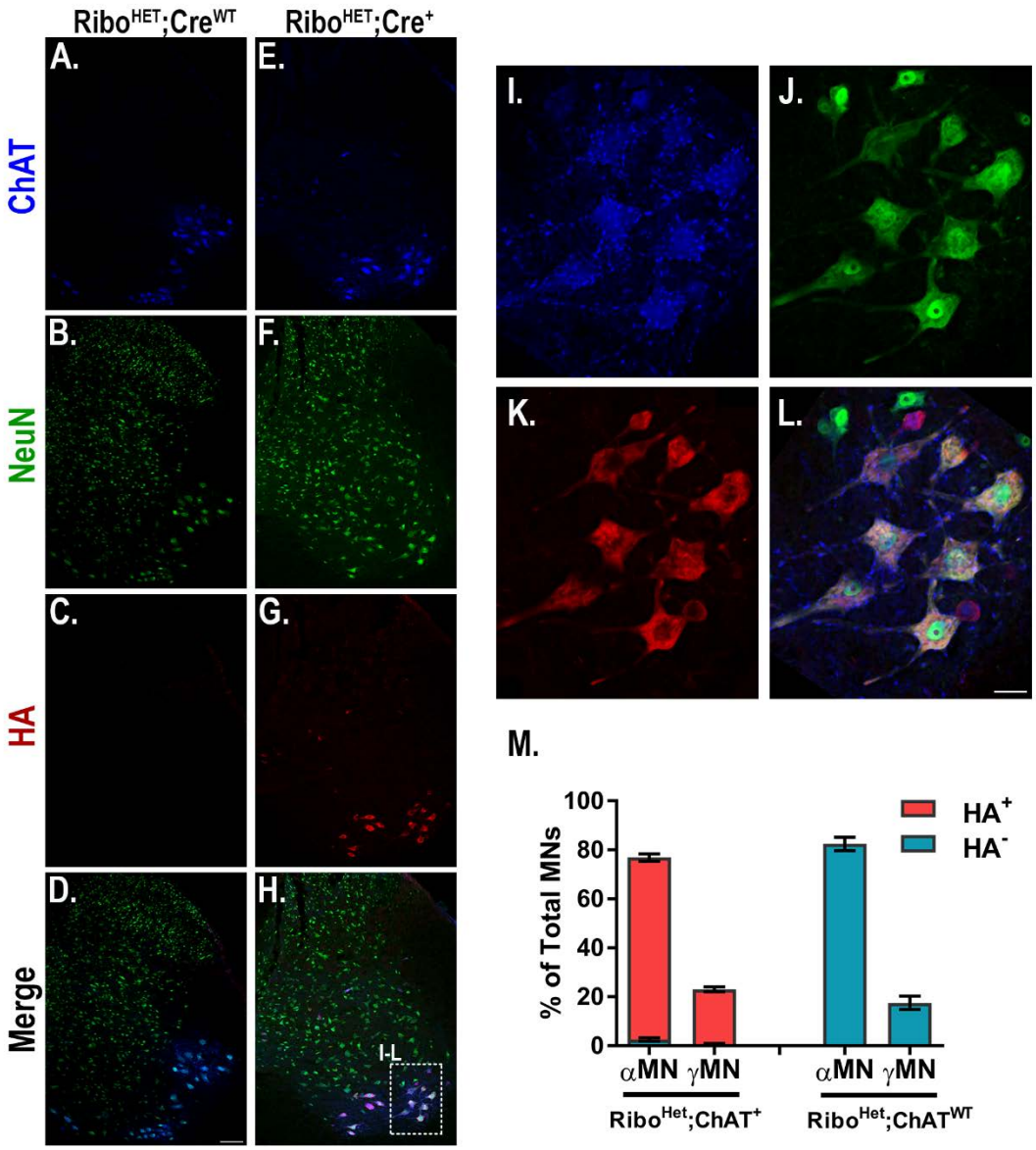

Figure 3.2. Quantification of RPL22^{HA} Expression in Somatic Motor Neurons.
Lumbar spinal cords were stained for ChAT (blue), NeuN (green), and RPL22^{HA} (red). ***A-H,*** Representative spinal cord hemisections from Ribo^{Het};ChAT^{WT} (A-D) and Ribo^{WT};ChAT^{+} (E-H) mice are shown. ChAT^{+} motor neurons in the ventral horn of the spinal cord show strong HA immunoreactivity in Ribo^{Het};ChAT^{+} (G), but not Ribo^{Het};ChAT^{WT} (C) mice. ***I-L,*** A magnified image of the cells highlighted in H illustrates the two populations of somatic motor neurons. ChAT^{+}NeuN^{+}HA^{+} alpha motor neurons (αMNs, open arrowhead) and ChAT^{+}NeuN^{-}HA^{+} gamma motor neurons (γMNs, asterisks). ***M,*** Somatic motor neurons in serial lumbar spinal cord sections were analyzed for HA expression. RPL22^{HA} was observed in nearly all αMNs and γMNs in Ribo^{Het};ChAT^{+} mice (n = 3) and no inappropriate HA staining was observed in wild-type littermates (n = 2).

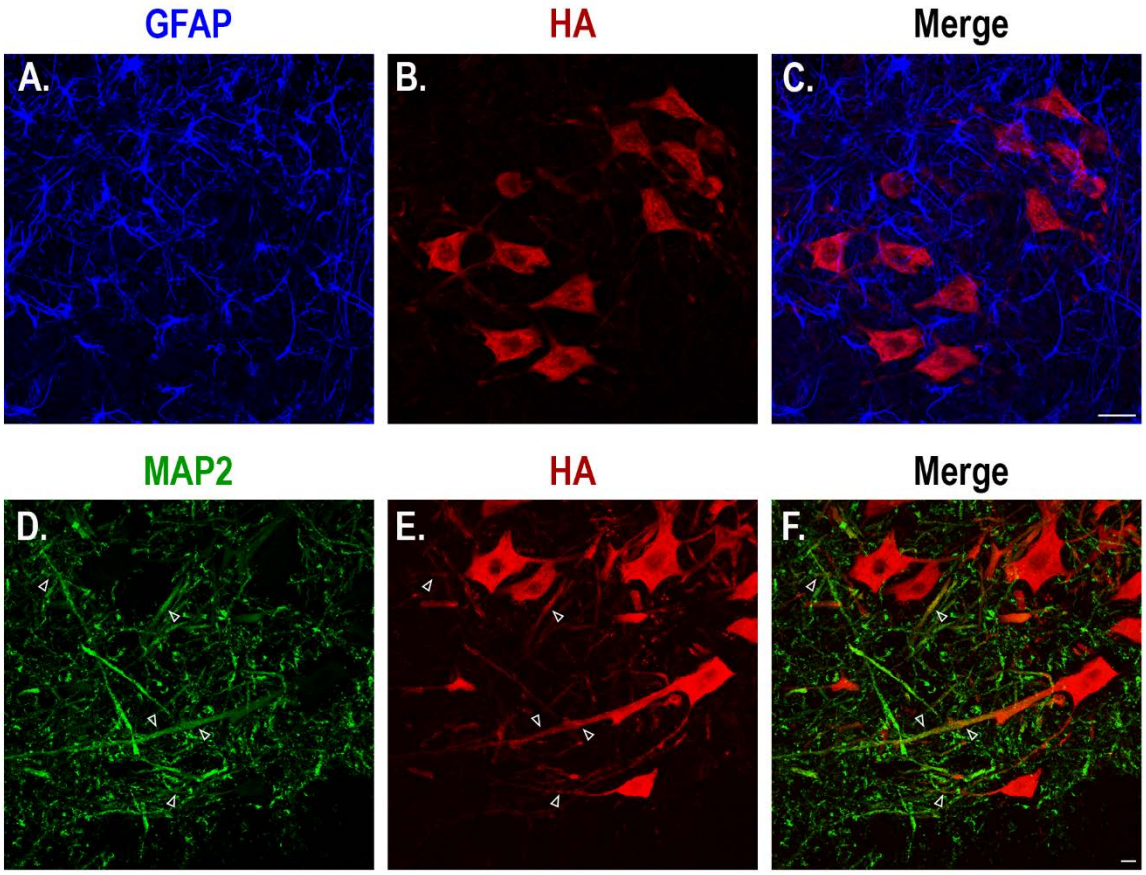

Figure 3.3. RPL22^{HA} is Observed in Motor Neuron Dendrites but not Glial Cells.
Immunostaining of lumbar spinal cord sections was performed to examine the extent of GFAP and MAP2 colocalization with RPL22^{HA} in glial cells and in motor neuron dendrites, respectively. ***A-C,*** GFAP^{+} (blue) astrocyte processes were observed in the vicinity of HA^{+} motor neurons (red), but do not express detectable levels of RPL22^{HA}. ***D-E,*** RPL22^{HA} immunostaining was observed extending outside the motor neuron cell body and colocalizing with MAP2^{+} motor neuron dendrites (arrowheads).

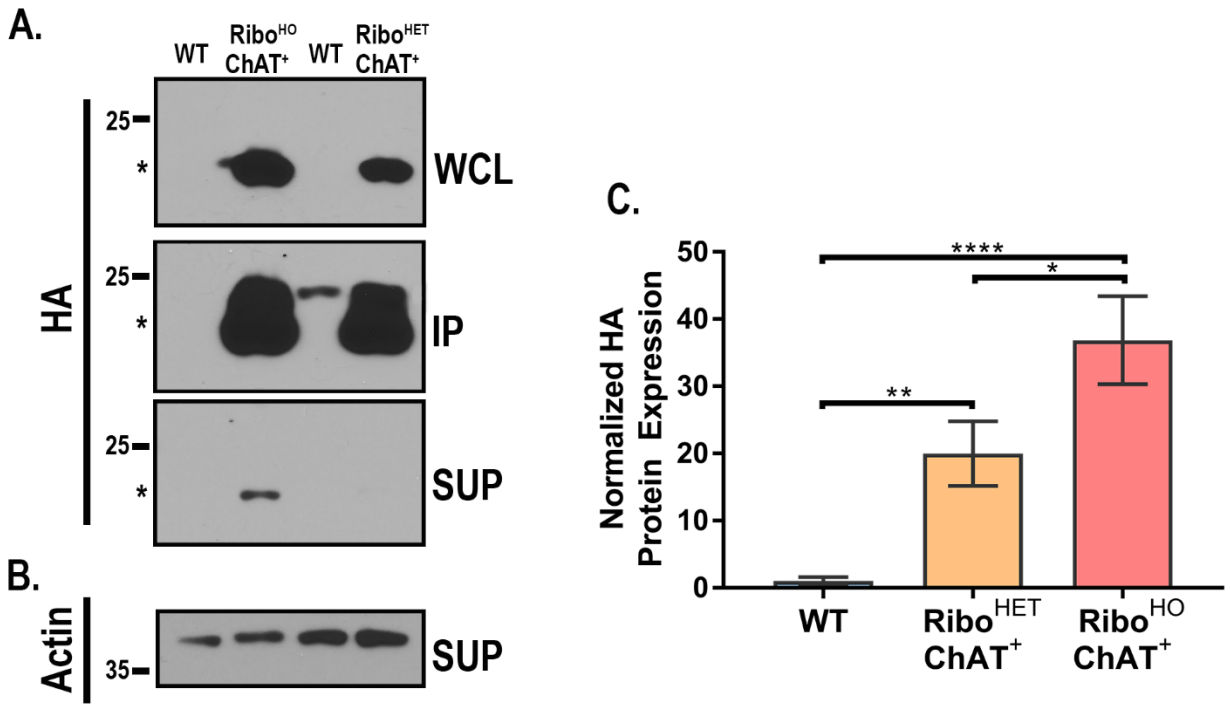

Figure 3.4. RPL22^{HA} can be Immunoprecipitated from Spinal Tissue in a Gene Dosage-Dependent Manner. Spinal cords were isolated from Ribo^{Het};ChAT^{+} (n = 9, HET), Ribo^{HO};ChAT^{+} (n =10, HO), and wild-type (n = 17, WT) littermates representing Ribo^{WT};ChAT^{+}, Ribo^{Het};ChAT^{WT}, and Ribo^{HO};ChAT^{WT} genotypes. ***A,*** Representative immunoblots demonstrate that RPL22^{HA} is readily detected in spinal cord whole cell lysates (WCLs). Additionally, after immunoprecipitation RPL22^{HA} becomes highly enriched in the immunoprecipitated product (IP) and depleted in the supernatant (SUP). ***B,*** SUPs were immunoblotted for actin as a loading control. ***C,*** The amount of immunoprecipitated RPL22^{HA} in WT, HET, and HO samples was quantified across all experiments and normalized to the amount of actin in corresponding SUP samples. Means are relative to SUP actin across experiments demonstrates there is a gene dose-dependent amount of HA protein in spinal cord lysates. Error bars represent the mean ± s.e, *p ≤ 0.05, ** p ≤ 0.01, **** p ≤ 0.0001.

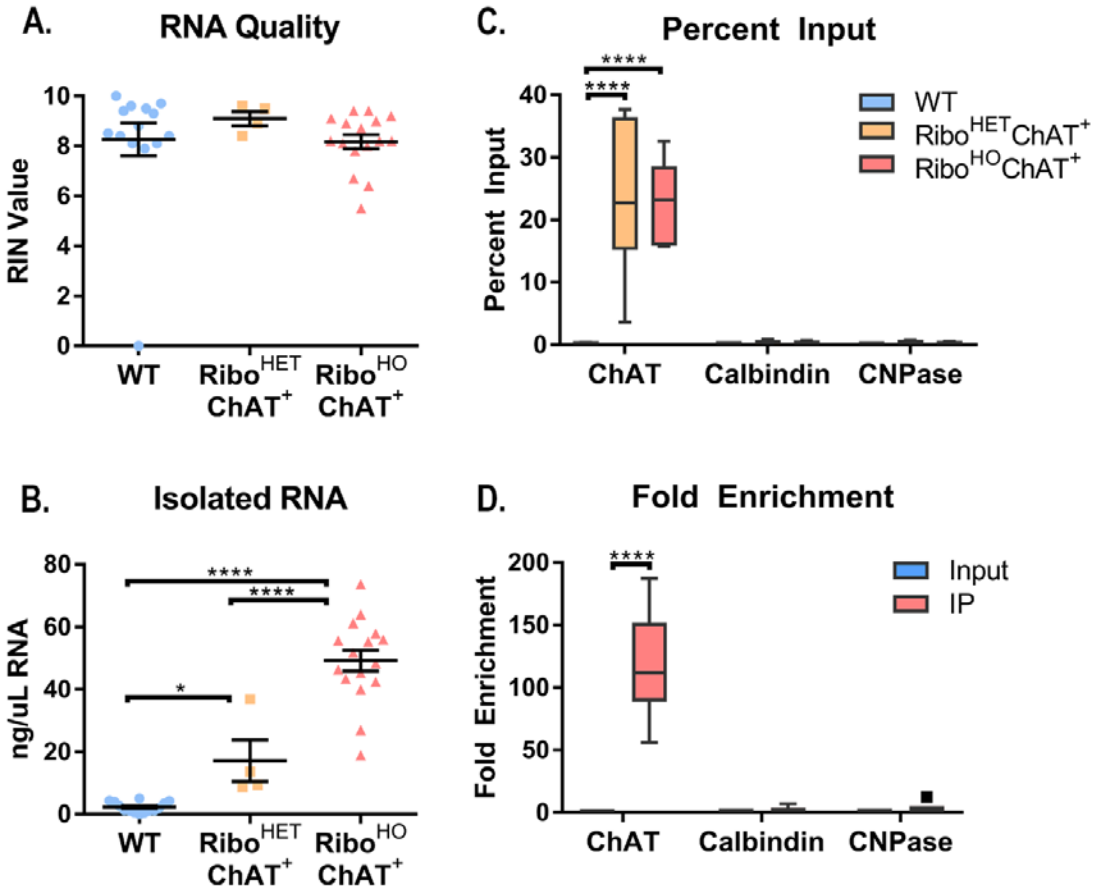

Figure 3.5. Isolation of RNA following RPL22^{HA} Immunoprecipitation from Spinal Tissue.
A-B, RNA was isolated after HA immunoprecipitation and subjected to Bioanalyzer analysis (WT, n = 14; Ribo^{HET};ChAT^{+}, n = 4; Ribo^{HO};ChAT^{+}, n = 16). RIN values demonstrate that high-quality RNA can be routinely isolated from all sample types (***A***). Similar to HA protein, the amount of isolated RNA obtained after IP occurs in a gene-dosage dependent manner (***B***). ***C-D,*** Isolated RNA from WT (n = 9), Ribo^{HET};ChAT^{+} (n = 6), and Ribo^{HO};ChAT^{+} (n = 9) mice were analyzed by RT-qPCR for positive- (*choline acetyltransferase* [*ChAT*]) and negative-control genes *(calbindin* and *2',3'-Cyclic-nucleotide 3'-phosphodiesterase* [*CNPase*] known to be expressed in interneurons and oligodendrocytes, respectively). Results are represented by both percent input (***C***) and fold enrichment of Ribo^{HET};ChAT^{+} and Ribo^{HO};ChAT^{+} mice over WT littermates (***D***). In all cases a dramatic enrichment of *ChAT* and absence of the negative-control genes demonstrate the specificity of RNA isolated after IP. For A-B, error bars represent the mean ± s.e. For C-D, data is graphed as Tukey box & whisker plots. *p ≤ 0.05, **** p ≤ 0.0001.

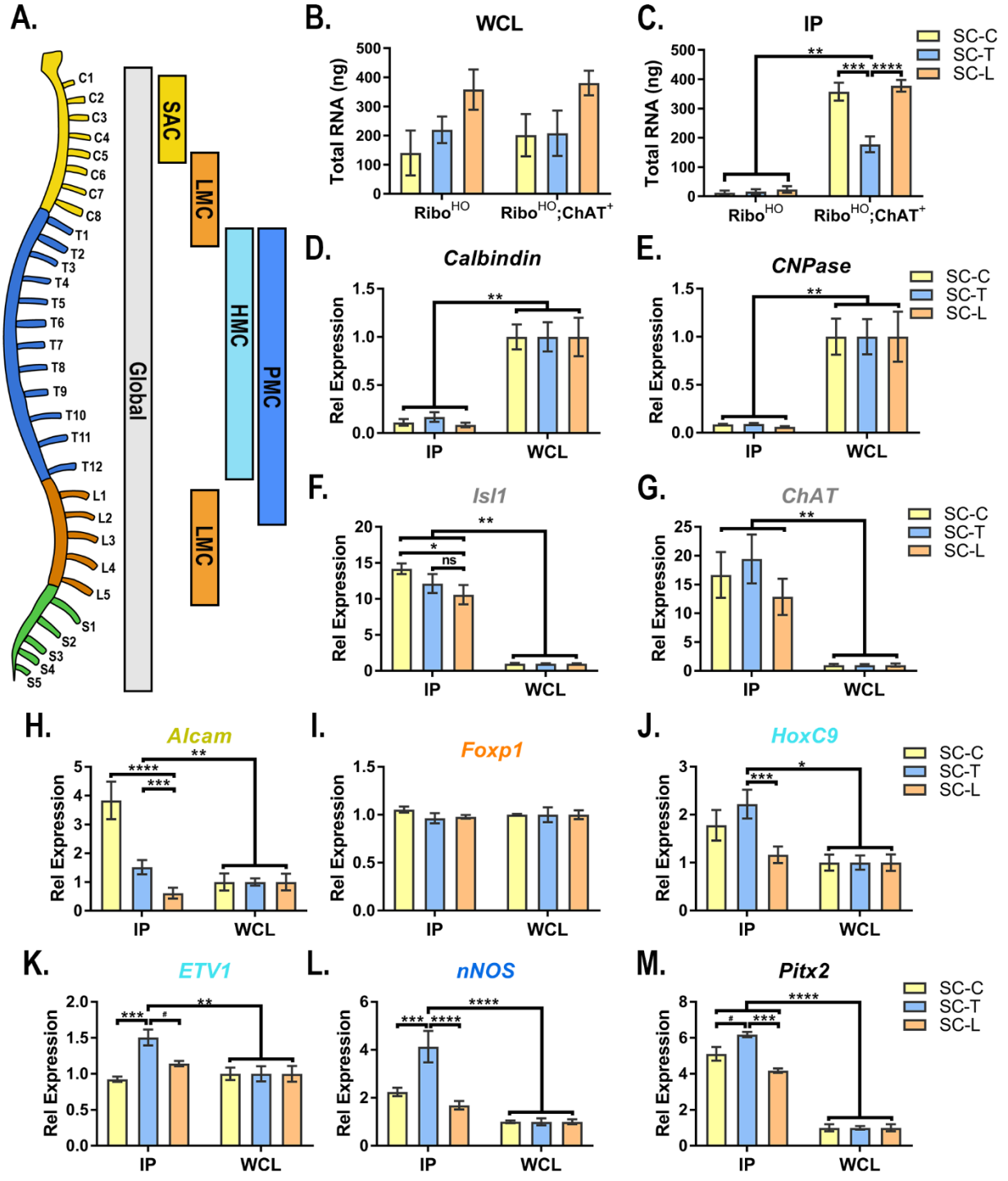

Figure 3.6. Region Specific Isolation of RNA and Transcript Analysis.
A, The schematic illustrates the four major divisions of the spinal cord (C1-C5: cervical; T1-T12: thoracic; L1-L5: lumbar; S1-S5: sacral). Additionally, the relative location of the different motor columns is depicted by the boxes to the right of the spinal cord. Some genes are known to be expressed more globally in motor neurons of many motor columns (Global, gray box). The spinal accessory column (SAC, yellow box) contains motors neurons found in the cervical spinal cord that innervate head and neck muscles, while the lateral motor column (LMC, orange boxes) contain motor neurons in the cervical and lumbar spinal cord that project to the forelimbs and hindlimbs, respectively.

Finally, the hypaxial motor column (HMC, cyan box) and preganglionic motor column (PMC, blue box) expand throughout the thoracic spinal cord and are responsible for innervating the axial muscles of the trunk (HMC) and autonomic ganglia of the sympathetic nervous system. ***B-C,*** Spinal cords were isolated from $Ribo^{HO}$;$ChAT^{WT}$ ($Ribo^{HO}$, n = 3) and $Ribo^{HO}$;$ChAT^{+}$ (n = 4) mice and separated into three regions: cervical (SC-C), thoracic (SC-T), and lumbar (SC-L). An HA IP was then performed on each region separately and RNA was isolated from a fraction of the whole cell lysis (WCL) before the IP and after the HA IP. Bioanalyzer analysis was then used to determine the amount of RNA in all samples. A similar amount of RNA was isolated in all WCL samples from $Ribo^{HO}$ littermate mice and $Ribo^{HO}$;$ChAT^{+}$ mice from the various spinal cord regions (***B***). After HA IP, the specificity of the IP is demonstrated in the enrichment of RNA in $Ribo^{HO}$;$ChAT^{+}$ mice. ***D-M,*** $Ribo^{HO}$;$ChAT^{+}$ IP and WCL RNA was examined for region-specific gene expression patterns. For all genes examined, samples were first normalized to actin and then gene expression of the IP is displayed relative to its expression in the corresponding WCL sample. The negative control genes *Calbindin* and *CNPase* illustrate that genes not expressed by motor neurons are de-enriched after HA IP (***D,E***). *Islet1* (*Isl1*) and *Choline acetyltransferase* (*ChAT*) are broadly expressed by motor neurons in motor columns that span the entirety of the spinal column (***F-G***). *Activated leukocyte adhesion molecule* (*ALCAM*), known to be expressed by motor neurons of the SAC, was found to be highly enriched in the SC-C (***H***). *Forkhead Box P1* (*Foxp1*) was expected to be found in LMC motor neurons; however, we did not find enrichment in any of the spinal cord regions (***I***). *Homeobox C9* (*HoxC9*), *ETS variant 1* (*ETV1*), and *Neuronal nitric oxide synthase* (*nNOS*) all showed varying degrees of upregulation in the SC-T (***J-L***). *Paired-like homeodomain transcription factor 2* (*Pitx2*) is known to be expressed by cholinergic pre-motor interneurons that reside near the central canal. In all three regions, an enrichment of *Pitx2* expression was observed, with the highest levels in the SC-T (***M***). Error bars represent the mean ± s.e, *$p \leq 0.05$, ** $p \leq 0.01$, *** $p \leq 0.001$, **** $p \leq 0.0001$.

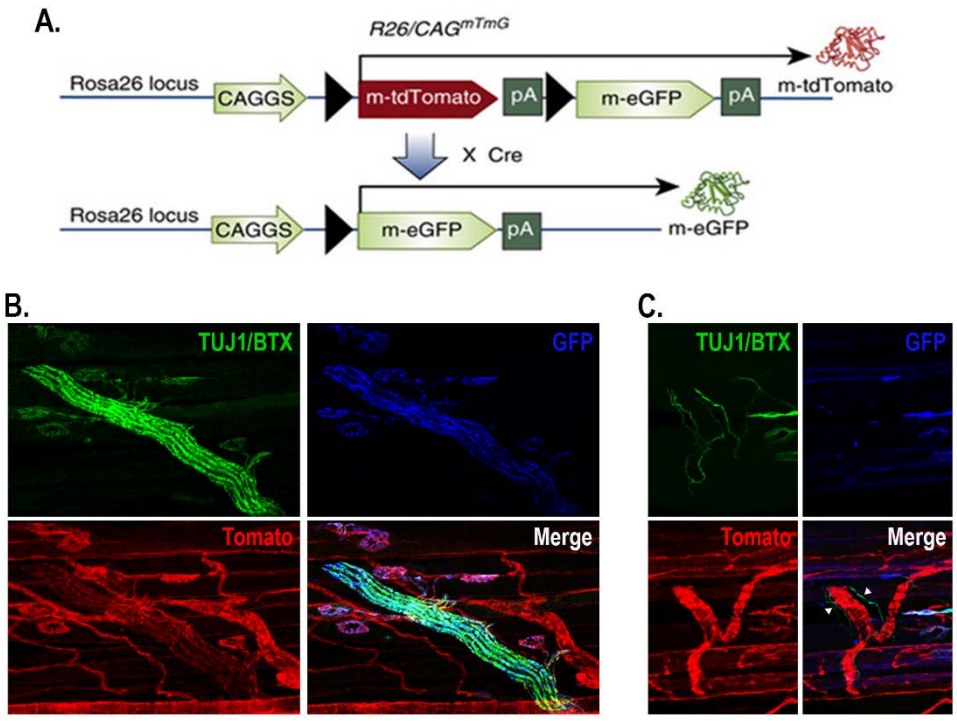

Figure 3.7. The *ChAT* promoter drives Cre expression specifically in cholinergic motor axons in the skeletal muscle.
ChAT-Cre mice were crossed to *R26/CAG*^{mTmG} reporter mice that ubiquitously express tdTomato in all cells in the absence of Cre. However, when Cre is expressed, the tdTomato construct is removed and an enhanced green fluorescent protein (eGFP) construct is produced (**A**). Strong eGFP expression (blue) was observed in the skeletal muscle colocalizing with ßIII-tubulin^{+} nerve fibers that innervate endplates labeled with bungarotoxin (BTX, green) (**B**) No eGFP expression is observed in ßIII-tubulin^{+} nerve fibers that travel along blood vessels (**C, arrowheads**). The diagram depicted in ***A*** was adapted from (Humphreys and DiRocco, 2014).

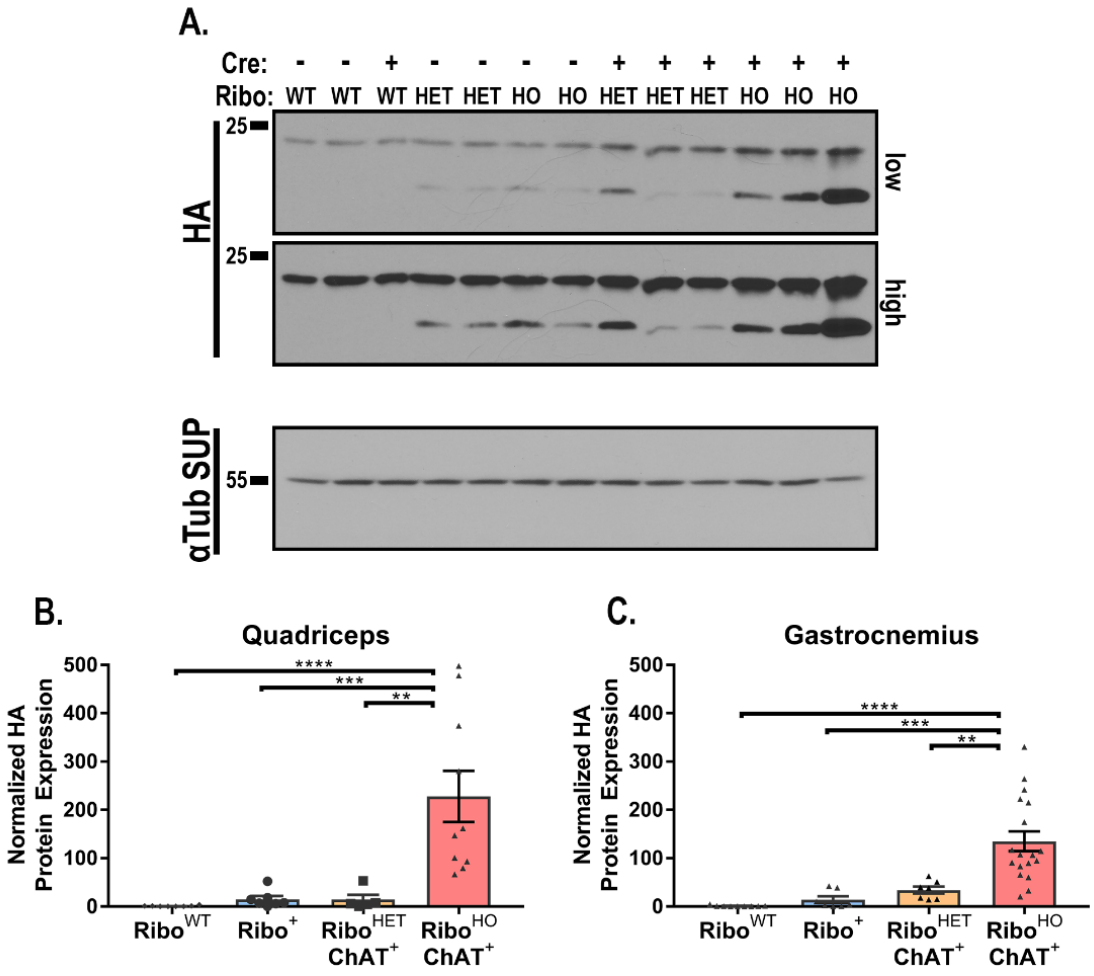

Figure 3.8. RPL22^{HA} Protein can be Immunoprecipitated from Motor Axon Terminals Innervating Skeletal Muscle.

Quadriceps (Quad) or gastrocnemius (GP) muscles were isolated from C57BL/6 or Ribo^{WT}ChAT^{+} mice (Ribo^{WT}, n = 8 [Quad], n = 9 [GP]), Ribo^{Het}ChAT^{WT} or Ribo^{HO}ChAT^{WT} mice (Ribo^{+}, n = 7 [Quad], n = 9 [GP]), Ribo^{Het}ChAT^{+} mice (n = 5 [Quad], n = 7 [GP]), and Ribo^{HO}ChAT^{+} mice (n = 10 [Quad], n = 18 [GP]). HA immunoprecipitation was then performed and the immunoprecipitated product was examined by western blot. ***A,*** The representative western demonstrates HA protein observed after IP from quadriceps muscle. A strong RPL22^{HA} signal is observed at the predicted weight (~23 kDA) in Ribo^{HO}ChAT^{+} mice. Additionally, all mice carrying 1- to 2- copies of RPL22^{HA} (Ribo^{+} and Ribo^{HET};ChAT^{+}) exhibit a low-level HA protein band, while mice that are Ribo^{WT} (C57BL/6 and Ribo^{WT};ChAT^{+}) show no detectable levels of HA protein, even under the longest exposure times. For all samples, supernatants were immunoblotted for αTubulin (αTub) as a loading control. **B-C,** Quantification of all experiments performed in quadriceps (***B***) and gastrocnemius (***C***) muscles is graphed. The amount of HA protein detected in the IP is normalized to αTub in the corresponding supernatant sample. A clear increase of RPL22^{HA} protein is detected in skeletal muscle of Ribo^{HO} mice in a *ChAT-Cre* dependent manner. Error bars represent the mean ± s.e, ** $p \leq 0.01$, **** $p \leq 0.0001$.

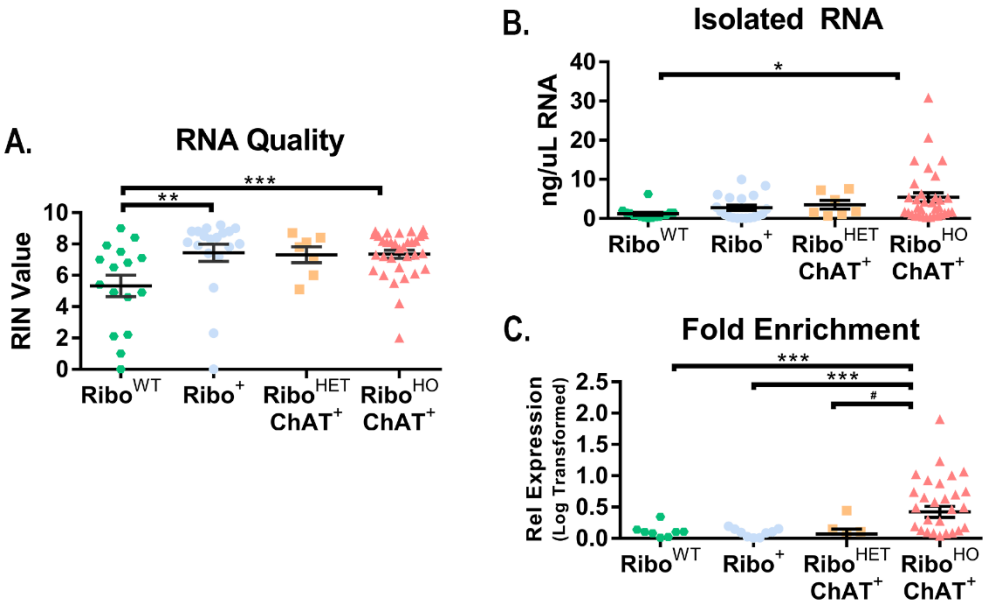

Figure 3.9. Isolation of RNA following RPL22^{HA} Immunoprecipitation from Skeletal Muscle.
RNA was isolated after HA immunoprecipitation and subjected to Bioanalyzer analysis (Ribo^{WT}, n = 16; Ribo^{+}, n = 19, Ribo^{Het};ChAT^{+}, n = 7, Ribo^{HO};ChAT^{+}, n = 33). **A,** RIN values demonstrate that high-quality RNA can routinely be isolated from all sample types, with slightly more degraded RNA found after HA IP from Ribo^{WT} mice. ***B-C,*** The enrichment of RNA in Ribo^{HO};ChAT^{+} mice is depicted in two ways: the raw concentration (ng/µl, ***B***) and normalized to the WT samples run in each independent experiment (***C***) followed by log transformation. For all graphs, error bars represent the mean ± s.e. #p ≤ 0.10 *p ≤ 0.05, ***p ≤ 0.001, **** p ≤ 0.0001.

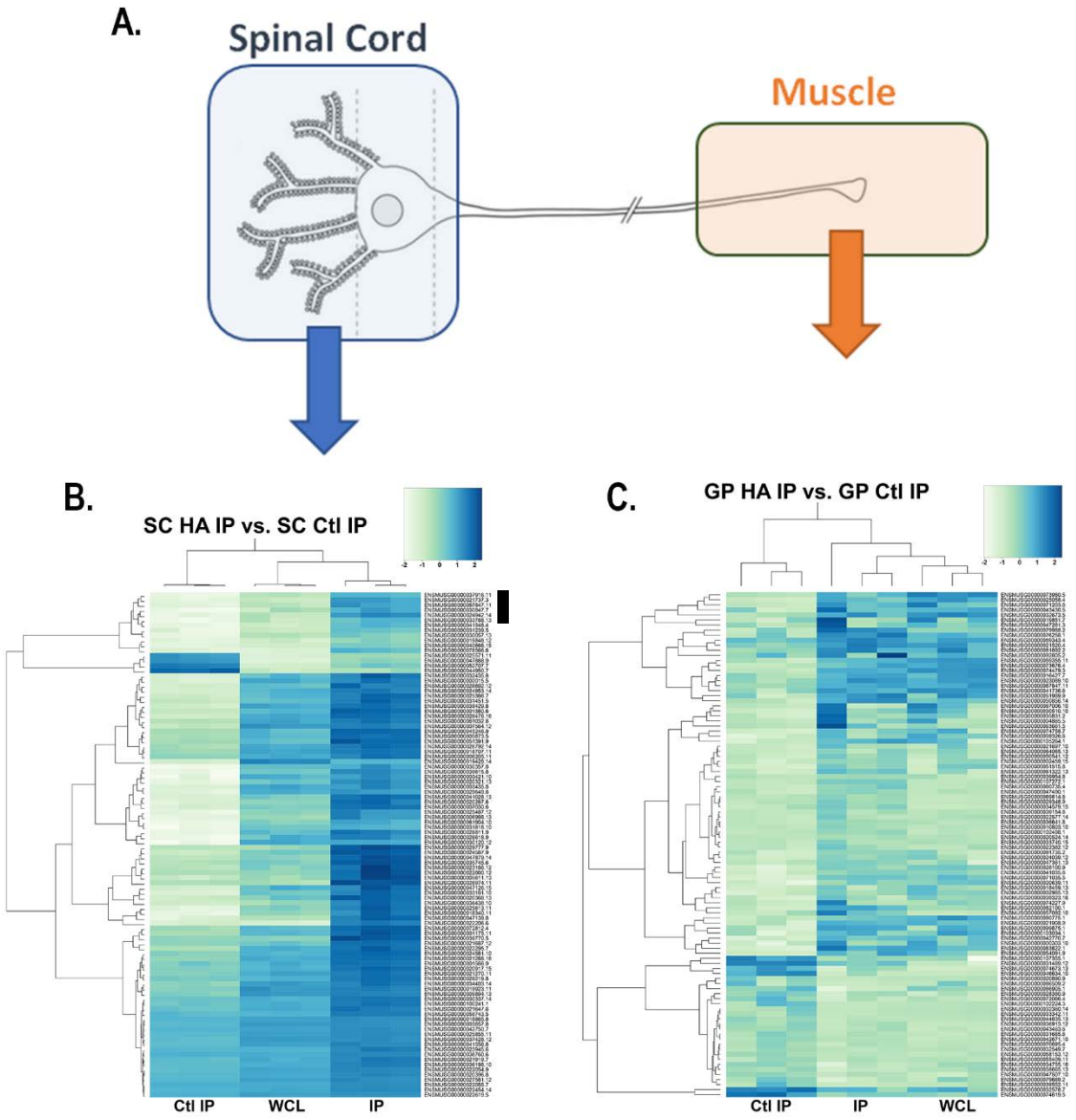

Figure 3.10. Novel Gene Discovery from Motor Cell Bodies and Distal Axon Terminals.
A, Spinal cord tissue (SC) and the gastrocnemius muscle (GP) were isolated from Ribo^{HO} (n = 3) and Ribo^{HO};ChAT^{+} (n = 3). HA IPs were performed on the different tissues independently, followed by RNA isolation and RNA-Seq analysis. ***B-C,*** Differential gene expression was performed to compare transcripts isolated after HA IP from Ribo^{HO};ChAT^{+} mice (IP) to that from Ribo^{HO} mice (Ctl IP). RNA from WCLs before HA IP was also sequenced and compared as an additional control. Heat maps from SC (***B***) and GP (***C***) tissues display the relative gene expression for the 100 most statistically significant genes, where dark blue represents highly expressed genes and light green represents low gene expression. The illustration in ***A*** was adopted from (Willis and Twiss, 2010).

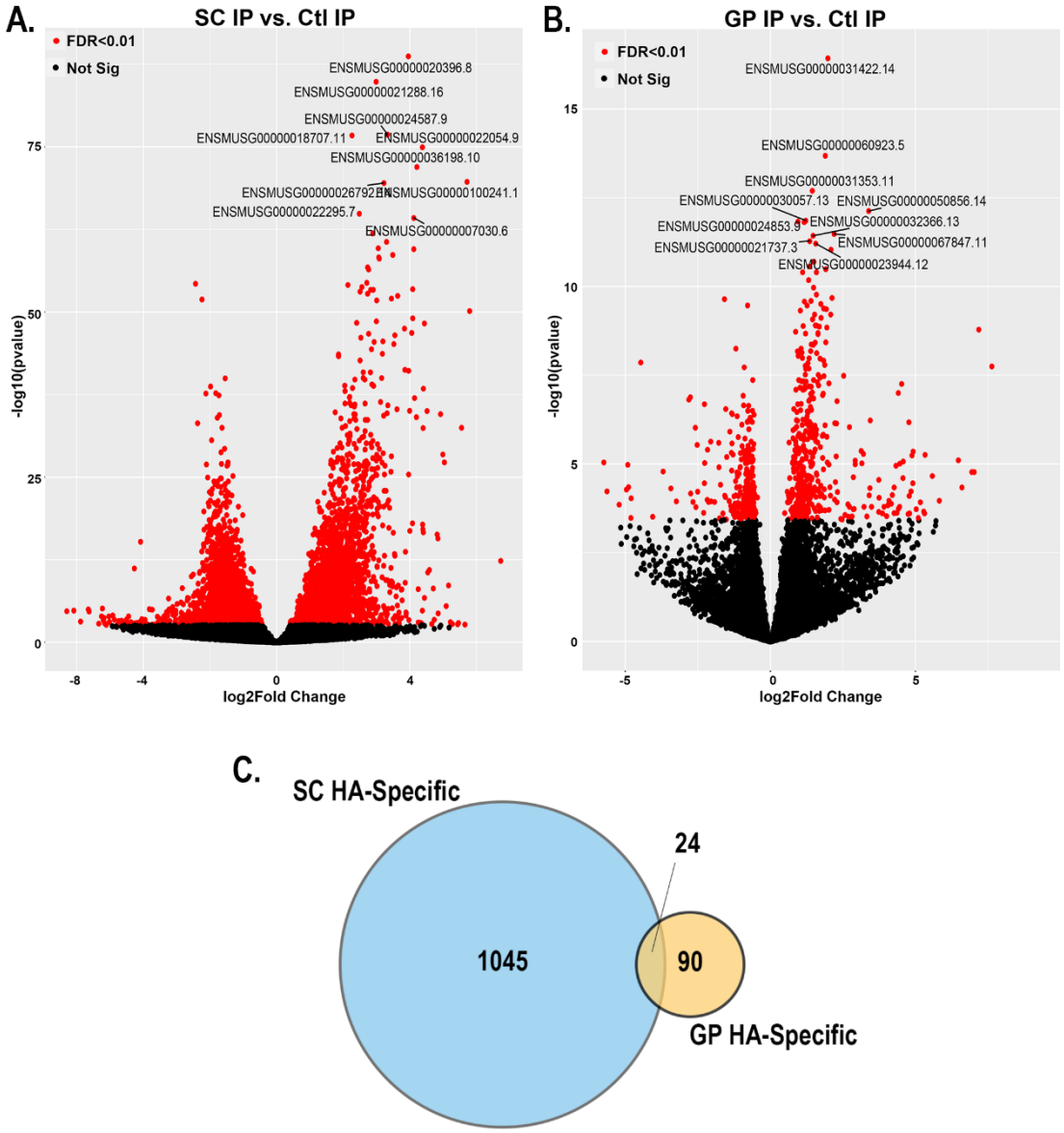

Figure 3.11. Enrichment after RPL22^{HA} Immunoprecipitation.
A-B, Volcano plots showing individual genes enriched in the IP (red dots with a positive log2Fold Change) vs. the Ctl IP (red dots with a negative log2Fold Change) are graphed. For both SC (***A***) and GP (***B***) tissues, transcripts are skewed to the top-right, indicating there is an enrichment after HA IP from Ribo^{HO};ChAT^{+} mice. ***C,*** The venn diagram illustrates the number of transcripts identified as enriched over the Ctl IP in the spinal cord (1066 transcripts) compared to the GP (114 transcripts), with 24 genes identified in both tissues.

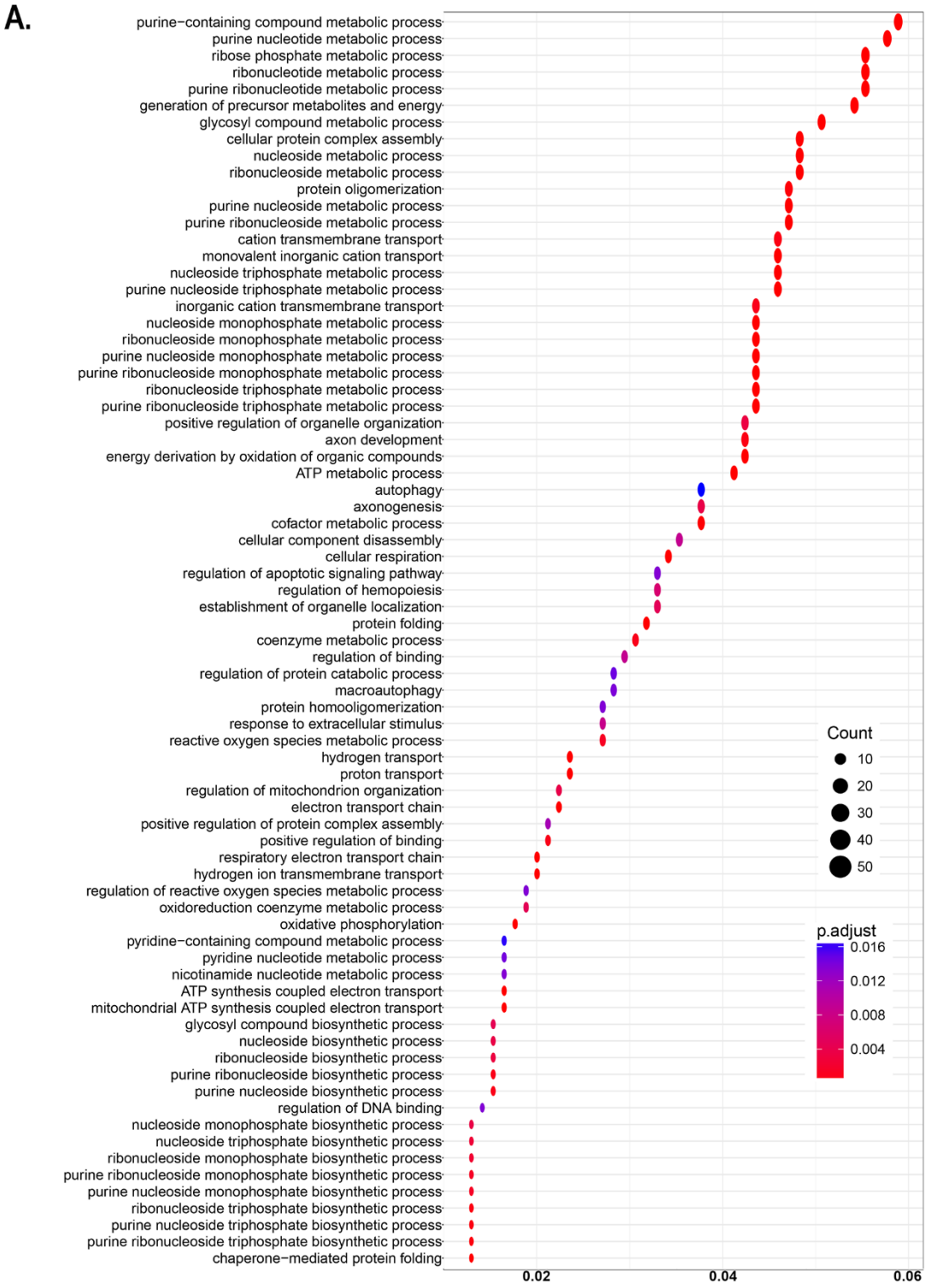

Figure 3.12. GO-Analysis of Transcripts Enriched in Motor Neuron Cell Bodies.
Gene ontology (GO) enrichment analysis was performed on the 1066 transcripts identified as enriched in RPL22^{HA} IP from Ribo^{HO};ChAT^{+} mice over the Ctl IP performed using Ribo^{HO} tissue. Categories with more representation have higher gene ratios (x-axis). The count reflects the number of genes within the GO term that are represented, while significance is denoted with a color scale. High p-values are represented by stronger red intensities.

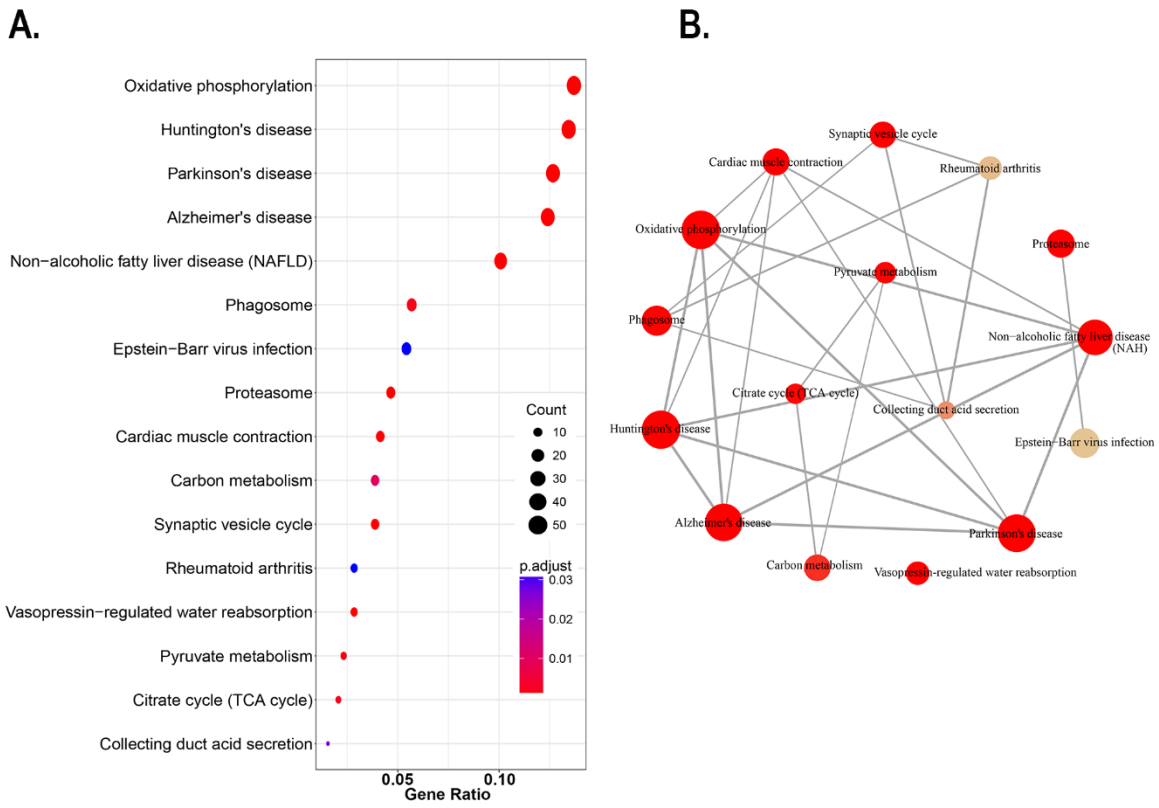

Figure 3.13. KEGG Analysis of Transcripts Enriched in Motor Neuron Cell Bodies.
A-B*,** Kyoto Encyclopedia of Genes and Genomes (KEGG) pathways analysis was performed on transcripts identified as specific to motor neuron cell bodies. Data is displayed as overall enrichment (A***) and relationally (**B**).

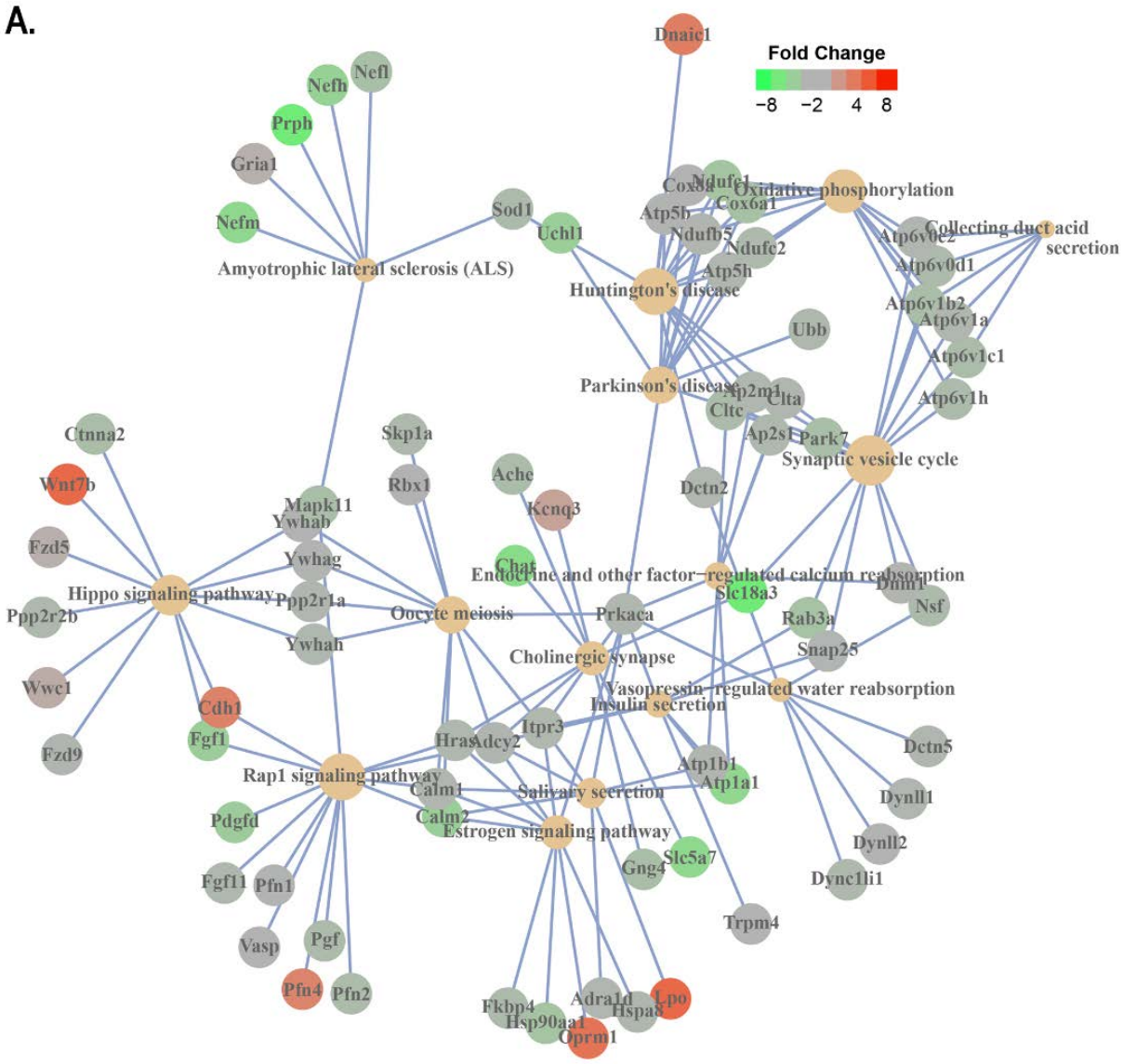

Figure 3.14. KEGG Analysis of Transcripts Identified in Motor Neuron Cell Bodies and Axons.
A-B, KEGG analysis of transcripts identified in motor neuron cell bodies and axons was performed. The relationship between overrepresented categories is illustrated in the diagram with genes enriched in cell bodies displayed in green and genes enriched in axons displayed in red.

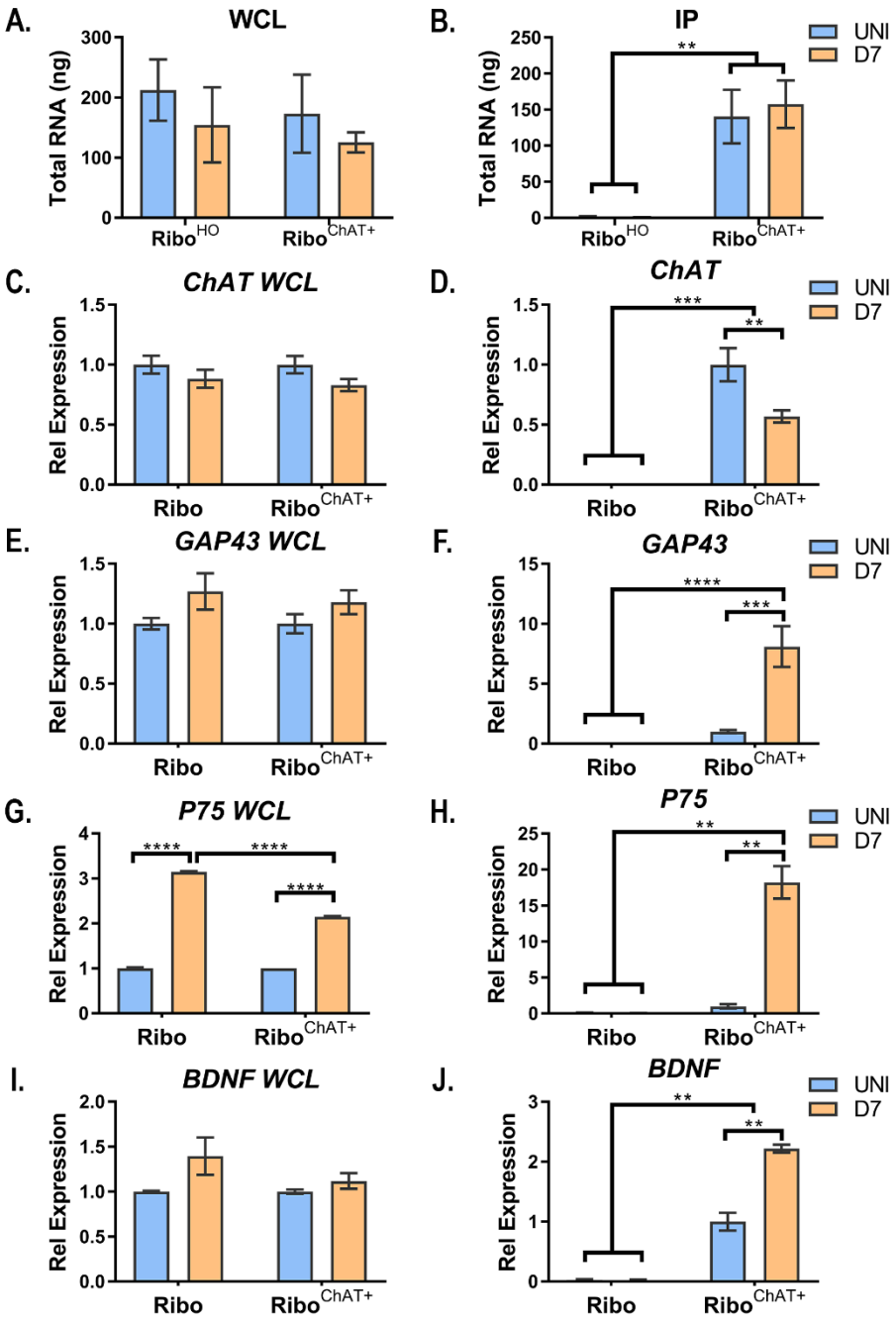

Figure 3.15. Changes in Motor Neuron Gene Expression Following Sciatic Nerve Crush.
The right sciatic nerve of Ribo^{HO} (n = 5) and Ribo^{HO};ChAT^{+} (n = 5) mice were crushed at the level of the mid-thigh. After 7 days, the lower 2/3 of the lumbar spinal cord was isolated. The left uninjured (UNI) and right D7 injured (D7) hemispheres of the spinal cord were separated and processed independently for HA IP. ***A-B,*** Bioanalyzer analysis was performed on all samples and RNA concentrations in WCL (***A***) and IP (***B***) samples is graphed. Similar levels of RNA were observed in all WCL samples, while significantly more RNA was detected in IPs from Ribo^{HO};ChAT^{+} mice compared to Ribo^{HO} controls. ***C-J,*** RT-qPCR was used to examine various genes in WCL (***C, E, G, I)*** and IP (***D, F, H, J***) samples. In most cases (except *P75*, ***G***) similar levels of gene expression were observed in the WCLs and a highly significant enrichment of transcript was observed in Ribo^{HO};ChAT^{+} mice compared to Ribo^{HO} controls. Additionally, there was an injury-dependent decrease of *ChAT* expression (***D***), while *GAP43* (***F***), *p75 neurotrophin receptor* (*P75*, ***H***), and *brain derived neurotrophic factor* (*BDNF*, ***J***) expression significantly increased in response to sciatic nerve crush. For all graphs, error bars represent the mean ± s.e. **p ≤ 0.001, *** p ≤ 0.001, **** p ≤ 0.0001.

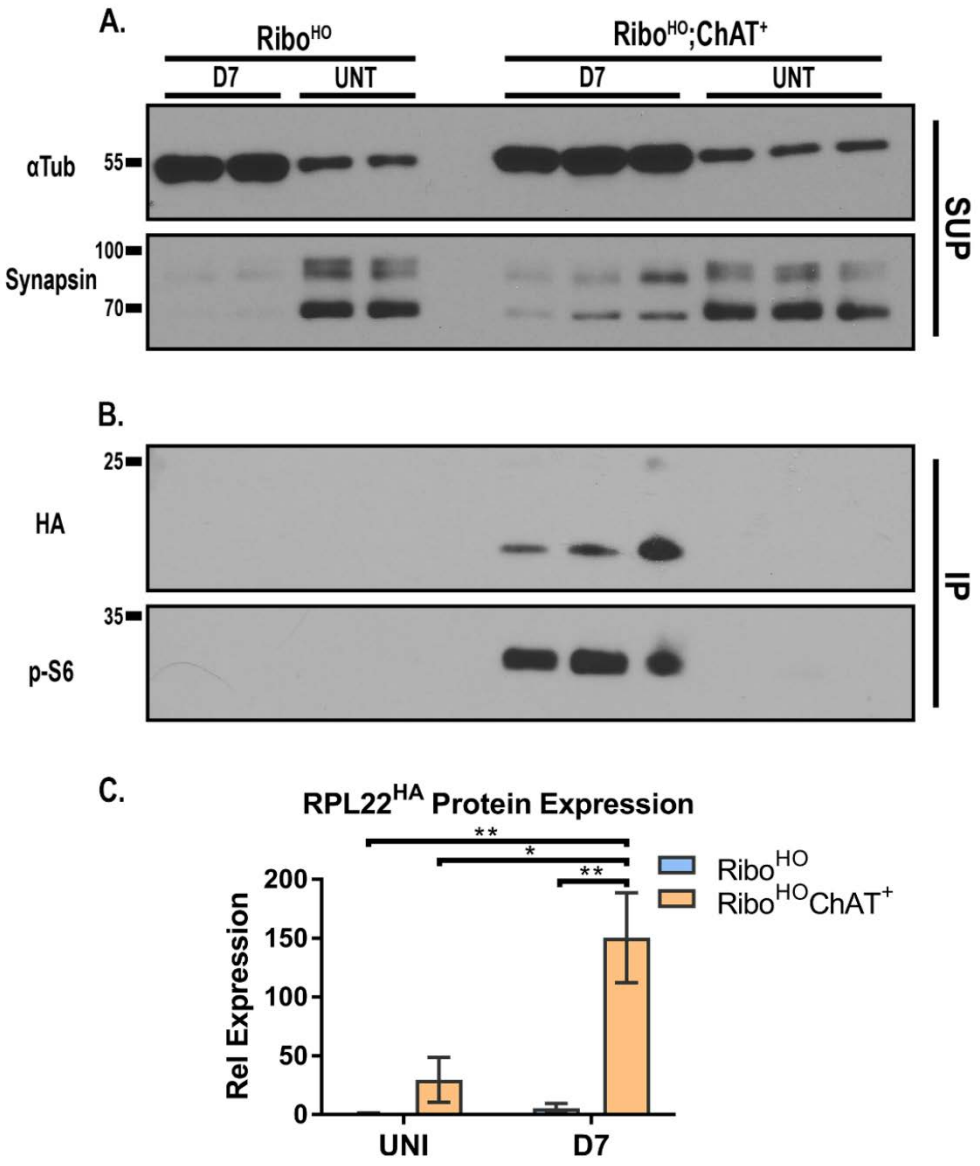

Figure 3.16. RPL22^{HA} is Significantly Enriched in Motor Axons in Response to Nerve Crush.
Ribo^{HO} control littermates (n = 9) and Ribo^{HO};ChAT^{+} (n = 5) mice underwent a common peroneal nerve crush. Injured and uninjured tibialis anterior muscles (TAs) were collected 7 days after injury. ***A,*** Representative western blots from SUP samples demonstrate that nerve crush results in an upregulation of αTub protein, while the presynaptic protein synapsin is downregulated. ***B,*** RPL22^{HA} and phoshpo-S6 Ribosomal protein (p-S6, a marker for increased translational activity) were detected in the IP after injury, while much lower levels were observed in the contralateral uninjured muscle. **C,** The amount of RPL22^{HA} expression in the IP was quantified across experiments.

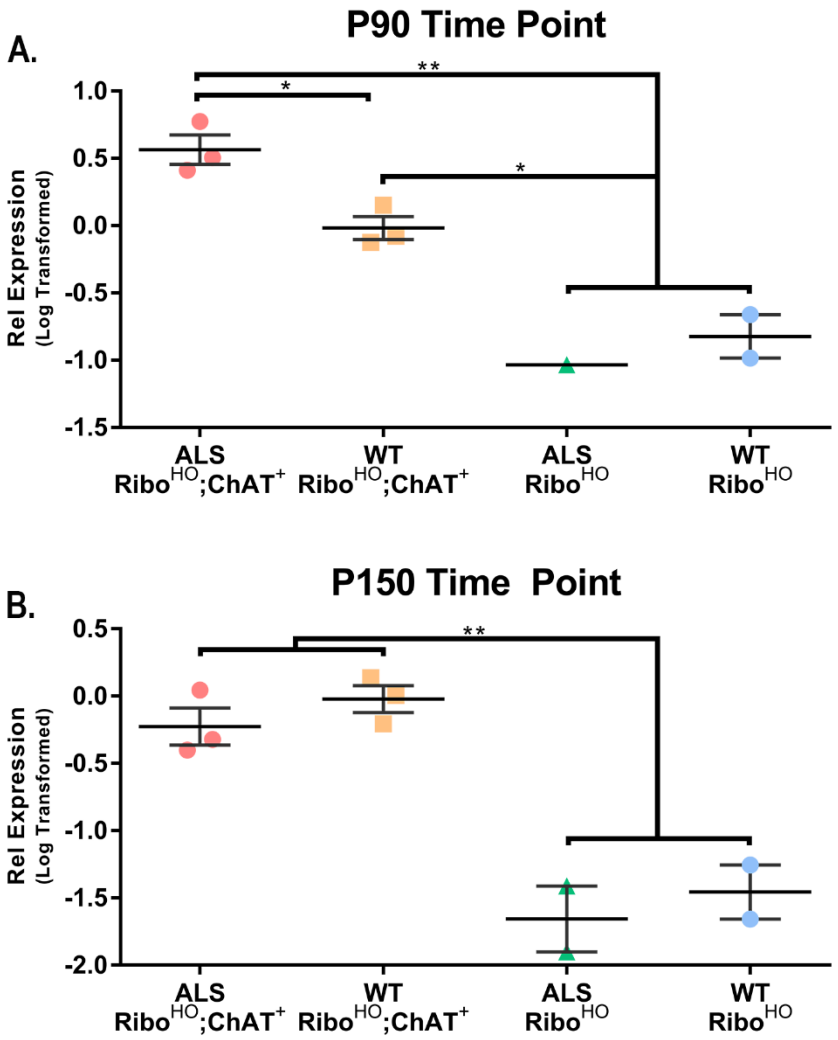

Figure 3.17. Isolation of Motor Neuron Specific Transcripts from ALS Mice.
The RiboTag;ChAT mouse line was crossed into the SOD1^{G93A} amyotrophic lateral sclerosis (ALS) mouse model. ALS Ribo^{HO};*ChAT-Cre*$^{+}$, WT Ribo^{HO};*ChAT-Cre*$^{+}$, ALS Ribo^{HO}, and WT Ribo^{HO} mice were aged to early symptomatic time point at 3 months (P90) or a terminal time point at 5 months (P150). RPL22^{HA} IPs were performed from isolated lumbar spinal cords and isolated RNA concentrations were determined by Bioanalyzer analysis. ***A-B,*** At the P90 time point there is a significant increase in the amount of isolated RNA obtained from ALS Ribo^{HO};ChAT^{+} mice as opposed to WT Ribo^{HO};ChAT^{+} littermates (***A***). ALS Ribo^{HO};ChAT^{+} and WT Ribo^{HO};ChAT^{+} mice had similar amounts of RNA isolated at the later P150 time point (***B***).

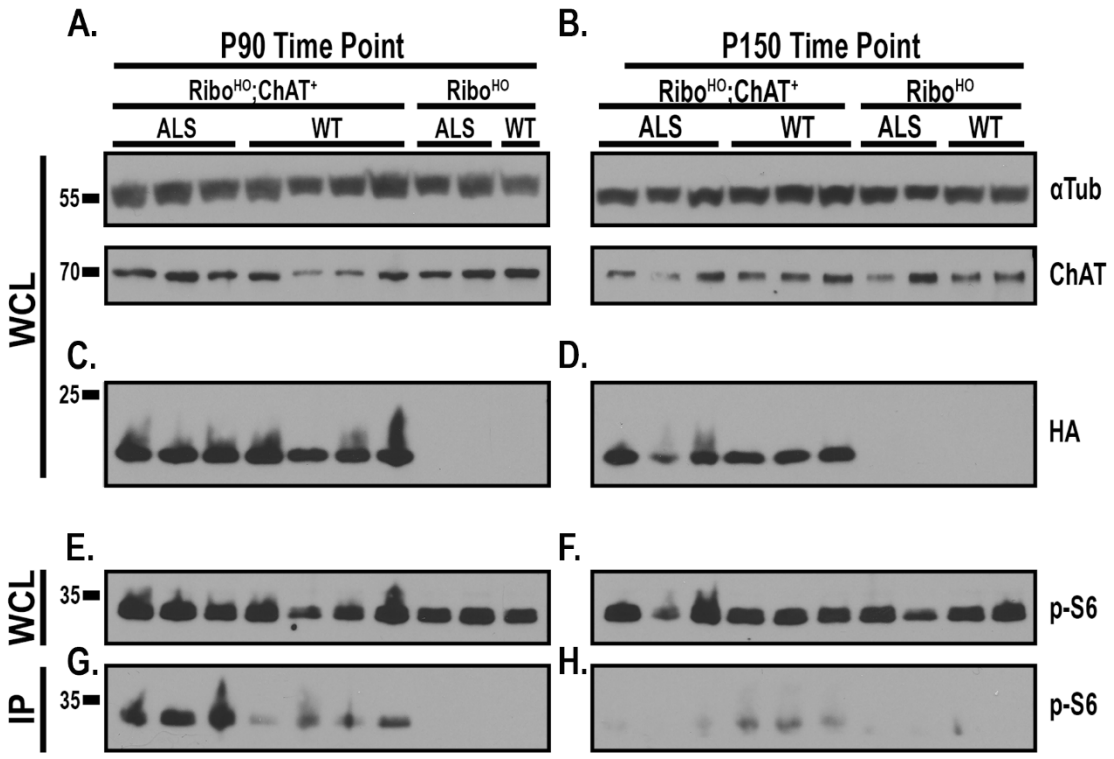

Figure 3.18. p-S6 Co-Immunoprecipitation May Indicate the Translational State of Ribosomal Complexes. ***A-H,*** Representative western blots of WCL and HA IP samples isolated from ALS and WT Ribo^{HO};ChAT^{+} mice and littermate controls at the P90 (***A,C,E,G***) and P150 (***B,D,F,H***) time points. Both αTub and ChAT protein expression in the WCLs are shown as loading controls (***A,B***). RPL22^{HA} protein in WCLs was not detected in Ribo^{HO} controls, but was readily detectable at both time points examined in ALS and WT Ribo^{HO};ChAT^{+} mice (***C,D***). p-S6 in WCLs and co-IPs was then examined as a marker of translational activity. At both time points, p-S6 is observed in WCLs of all mice examined (***E,F***), while in the IP it was only detectable in Ribo^{HO};ChAT^{+} mice (***G,H***). Furthermore, the level of p-S6 in the IP was greatly increased in ALS Ribo^{HO};ChAT^{+} mice compared to WT Ribo^{HO};ChAT^{+} controls at the P90 time point (***G***), while it was barely detectable in ALS Ribo^{HO};ChAT^{+} mice by the terminal P150 time point (***H***).

CHAPTER 4: CONCLUSION

Regulation of Motor Innervation at the Neuromuscular Junction

The mechanisms that govern reinnervation of the neuromuscular junction (NMJ) are complex, but many studies have begun to tease apart the various signaling molecules involved (Schmidt et al., 2009). In the work presented here, we have sought to contribute to that understanding. Specifically, we have established a sciatic nerve crush injury model that allows for the quantitative assessment of NMJ reinnervation, examined the functional significance of Semaphorin3A (Sema3A) signaling at the adult NMJ, and developed an unbiased means for identifying novel pathways that regulate NMJ reinnervation.

Previous work had suggested that Sema3A might establish an inhibitory environment that negatively impacts motor axon regeneration and NMJ reinnervation. Therefore, it was proposed that specifically reducing Sema3A at the NMJ might have a therapeutic potential for treating sciatic nerve crush injury and neurodegenerative disease. To directly test this hypothesis, we developed a common peroneal sciatic nerve crush model and used histological methods to carefully interrogate different phases of NMJ reinnervation. We then used that model in conjunction with conditional knockout mice to examine how NMJ reinnervation is impacted in the absence Sema3A signaling. However, loss of Sema3a or of its high-affinity receptor Neuropilin1 (Npn1) did not disrupt the normal maintenance or improve regeneration of the NMJ.

Next, to identify novel mediators of NMJ innervation, we developed a rapid and unbiased method to isolate motor neuron specific transcripts from complex tissues *in vivo*. This was achieved by using RiboTag technology to incorporate an HA tag on Ribosomal Protein RPL22 ($RPL22^{HA}$) in cholinergic neurons. We then demonstrate that this model can be used to study motor neuron specific gene expression and local translation in motor axons.

Taken together, we believe the work presented here will lead to future studies that will continue to uncover the molecular mechanisms employed by motor neurons during times of health, injury, and disease. In the following sections, we consider outstanding questions and important future directions for the field.

Outstanding Questions and Future Directions

Semaphorin 3A Signaling at the Neuromuscular Junction

Although our study found that Sema3A signaling was not required for adult NMJ maintenance or regeneration after injury, there are still outstanding questions that need to be addressed. First, we still have a poor understanding of the different cell type(s) that express the various components necessary for Sema3A signaling in adult muscle. Motor neurons have been described to express Npn1 mRNA (De Winter et al., 2006; Molofsky et al., 2014; Venkova et al., 2014) and using the RiboTag;*ChAT-Cre* model we were able to demonstrate that as well [data not shown]. Additionally, mRNA for *PlexinA1-A4* (*PlexA1-A4*) has been demonstrated in motor neurons by *in situ* hybridization (De Winter et al., 2006). Therefore, although the components for Sema3A signaling are present, where those receptors localize to and how they are regulated in

response to different stimuli is unclear. There is some evidence that Npn1 protein is expressed at motor axon terminals at the NMJ (Venkova et al., 2014). We have also attempted to characterize Npn1 protein expression at the NMJ, but non-specificity of the antibody made that analysis difficult to interpret. Despite this limitation, by using synaptic and extra-synaptic preparations from skeletal muscle, we have been able to show Npn1 protein is more concentrated synaptically than extrasynaptically [data not shown]. Furthermore, while some studies have tried to address Npn1 localization, the PlexA family member expression at the NMJ has yet to be described in detail.

The cellular source of Sema3A also remains somewhat elusive. In previous studies, two different research groups have pinpointed Sema3A expression to two different cell types. Using *in situ* hybridization, one group localized *Sema3A* mRNA expression to regions surrounding the NMJ. Histological evaluation identified Terminal Schwann Cells as the cellular source of Sema3A (De Winter et al., 2006). Conversely, through the use of a variety of *in vitro* and *ex vivo* models, another group has found that muscle stem cells can produce Sema3A in response to injury (Tatsumi et al., 2009). We have also tried to determine which cell type is responsible for *Sema3A* production using a variety of methods (generation of Sema3A-BAC-GFP mouse line, immunostaining, and immunoblotting), but we have not been able to successfully address this question.

Interestingly, our RT-qPCR data raises questions about what cell type(s) express the various Sema3A signaling molecules. After sciatic nerve crush we found a specific reduction of both *Sema3A* and *Npn1* mRNA in muscle tissue after injury. Furthermore, *Npn1* expression was found to return to normal by day 30 after injury, but *Sema3A* mRNA levels remained diminished even at the latest time point examined. While the

reduction in *Sema3A* may indeed be explained by the fact that it is secreted by Terminal Schwann cells, our data suggests that some other population of cells in the muscle other than the motor axon must express Npn1 and be responsive to nerve crush. Furthermore, it is interesting that *Sema3A* mRNA levels did not return to baseline. This might reflect the fact that *Sema3A* levels do not normalize until the NMJ is fully remodeled, taking longer than 50 days for this to occur. Future studies to extend the analysis to later time points may help to address this question.

Lastly, it is interesting that we could observe gene expression changes in *Sema3A* and *Npn1* after nerve crush, but did not detect a functional consequence to altering Sema3A-Npn1 signaling. This might reflect the complexity and functional redundancy of mechanisms that underlie neuromuscular junction maintenance and regeneration. As discussed previously, many growth factors, morphogens, neurotrophins, and axon guidance molecules have been prescribed different roles at the NMJ during development and disease. Therefore, we cannot rule out the possibility that another mechanism is able to compensate for the loss of Sema3A-Npn1 signaling at the NMJ. Future studies to begin to address the role compensation plays at the NMJ may be useful in the identification of combinatorial strategies to improve regeneration and function. As the cost of RNA-sequencing (RNA-Seq) reduces, one strategy to identify compensatory pathways might entail examining transcriptional changes in motor neurons in the presence or absence of particular signaling molecules (i.e. Sema3A). Another strategy could include using CRISPR/Cas technology to alter multiple genes throughout the mouse genome at one time (Wang et al., 2013). By targeting multiple members within a family of signaling molecules (like Sema3A and Sema3F) or multiple

signaling pathways simultaneously (like Sema3s and EphrinAs), we might be able to identify synergistic ways to improve regeneration of the NMJ.

Direct Targeting of Somatic Motor Neurons

To develop an unbiased means to assess motor neuron gene expression, we combined RiboTag technology (Sanz et al., 2009) with the *choline-acetyltransferase* (*ChAT*) promoter. Importantly, we characterized the methodology and demonstrated that it indeed allows for the specific isolation of motor neuron transcripts from the spinal cord. However, there is a minor limitation associated with the *ChAT* promoter because it labels cholinergic neurons other than somatic motor neurons. Therefore, new methods to limit analysis specifically to somatic motor neurons would improve the interpretation of future gene expression studies.

One such strategy to directly target somatic motor neurons would be through the use of retrograde viruses. For example, the adeno-associated virus 6 (AAV6) has been used to retrogradely drive gene expression in motor neurons (Kaplan et al., 2014). Therefore, performing intramuscular injections of an AAV6-Cre virus would specifically drive $RPL22^{HA}$ expression in motor neurons from discrete motor pools. Furthermore, driving Cre-mediated recombination in this manner would not only directly target somatic motor neurons, but would also provide the following advantages: 1) injecting virus only into one hindlimb would allow the contralateral limb to serve as an internal control; 2) it would eliminate the need to generate complex triple transgenic mouse lines to assess motor neuron gene expression with different genetic models; and 3) the

function of genes that are developmentally lethal could be examined in adult motor neurons by restricting the analysis to a small motor pool.

In addition to the targeted use of viruses to drive more specific Cre expression, our bioinformatics data from adult motor neurons may provide a strategy to discover novel genes restricted to somatic motor neurons. Examination of the heatmap comparing the most significantly enriched transcripts after $RPL22^{HA}$ immunoprecipitation (IP) to control IPs and whole cell lysates demonstrates that some genes are specifically enriched in the $RPL22^{HA}$ IP. Future characterization of those transcripts through *in situ* hybridization may lead to the identification of a new gene marker for somatic motor neurons. That information could then be used to derive a *Cre*-recombinase line. Importantly, this could be useful for both the RiboTag technology and it would generate a way to alter motor neuron gene expression with fewer off-target effects.

Defining a Local Translatome for Motor Axons

There are currently two main models that allow for Translating Ribosome Affinity Purification (TRAP). First, BAC-TRAP mice were developed such that a tissue-specific promoter could drive the expression of an exogenous GFP-L10a ribosomal transgene (Heiman et al., 2008). Subsequently, the RiboTag model was developed to directly target the endogenous RPL22 protein (Sanz et al., 2009). Importantly, the key difference between the two models is how the epitope tagged ribosomal protein is produced. In the BAC-TRAP methodology, exogenous GFP-L10a must compete with its endogenous counterpart, which reduces the efficiency of incorporation into the

ribosome. Conversely, that problem is eliminated in the RiboTag model because it directly targets the endogenous *RPL22* locus (Jung and Jung, 2016).

Despite the enhanced efficiency, here we report observations that there is a small degree of leaky $RPL22^{HA}$ expression in the absence of Cre. Although this does not impact the enrichment of tissue specific transcripts from populations that have abundant levels of translating RNA, it makes the analysis more challenging when the transcript abundance in the population under investigation is minute. As such, in our study of local translation of axons, we were not able to completely purify the axonal mRNAs from those associated with leaky $RPL22^{HA}$. Despite this limitation, we were able to provide evidence that some axonal transcripts are indeed enriched in motor axons. Importantly, future analysis using *in situ* hybridization will be required to assess whether putative transcripts are truly locally translated in motor axons.

Finally, it is interesting to note that in a recent paper, the RiboTag Technology was successfully applied to study local translation in retinal ganglion cells (Shigeoka et al., 2016). In this report, the authors similarly observed that nonspecific RNAs associate with the HA IP in *Cre*-negative controls. However, the signal they captured after HA IP from Cre^{+} mice was much more enriched over the control compared to what we have observed in motor axons. While any number of things might account for these differences, age at isolation and tissue type may be crucial factors. Although local translation is involved in the normal maintenance of adult tissues, studies have generally found that it is more active at developmental stages and in response to injury (Willis and Twiss, 2006). Accordingly, Shigeoka et al., found that significantly more RNA was isolated from retinal ganglion cell axons during developmental axon pathfinding and

synaptogenesis than in the adult. Furthermore, tissue type might have also contributed to differences in the isolation efficiency because, compared to nervous system tissue, skeletal muscle contains a significant amount of connective and fibrous tissue that is challenging to homogenize. Together, these factors may help explain why it was more difficult to detect motor axon transcripts at adult NMJs.

In the future, studies of local translation in specialized compartments such as axons would benefit from the development of additional tools that avoid problems associated with leaky expression. In the meantime, given the methods currently at our disposal, it might be possible to improve the purification of transcripts from motor axons by focusing on injury models or development.

Applicability to Models of Motor Nerve Injury and Neurodegeneration

Using the RiboTag;*ChAT-Cre* model we demonstrated that this technology can be applied to examine how motor neuron gene expression changes in response to both injury and neurodegeneration. Importantly, this opens the door to a broad array of exciting possibilities. Comparing how motor neurons respond to nerve crush, nerve cut, and neurodegeneration would be particularly illuminating. By understanding how these processes are similar and where they diverge may reveal novel strategies that can be used for the therapeutic treatment of peripheral nerve injury and neurodegenerative disease, such as amyotrophic lateral sclerosis (ALS).

In addition to comparing different injury paradigms, this strategy is well suited to dramatically expand our knowledge about how different forms of motor neuron disease (MND) affect motor neuron function. Although *Superoxide dismutase 1* (*SOD1*) was the

first gene identified to cause ALS, work since has uncovered that mutations in many other genes can also result in ALS (Renton et al., 2014). Perhaps most importantly, the discovery that *TARDBP*, *FUS*, and *C9ORF72* mutations lead to ALS has transformed our understanding of the molecular processes that lead to pathogenesis in MND. While *SOD1* mutations initially highlighted oxidative stress and metabolic dysfunction as important pathways that result in MND (Sas et al., 2007; Johri and Beal, 2012; Ngo and Steyn, 2015), *TARDBP*, *FUS*, and *C9ORF72* all encode proteins that are involved with RNA biogenesis and trafficking (Yasuda and Mili, 2016). Given disparate molecular etiologies, the degree to which these MNDs should be painted with the same brush has lately come into question (Mackenzie et al., 2007; Renton et al., 2014). Therefore, although we have initially crossed the $SOD1^{G93A}$ model to the RiboTag;*ChAT-Cre* mouse line, future experiments incorporating other forms of MND may help to uncover key differences in pathogenesis. Given that *TARDBP*, *FUS*, and *C9ORF72* have all been linked to RNA metabolism and processing, exploring how local translation is affected in motor axons in those models will be particularly interesting.

Finally, in addition to examining transcripts that are associated with ribosomes in motor neurons, we also demonstrated that the RiboTag technique can be applied to examine other translational proteins that associate with the IP. We have initially done this through the examination of phosphorylated-S6 ribosomal protein (pS6). Importantly, association of p-S6 in the ribosomal complex has been used as marker of translationally active ribosomes (Kalinski et al., 2015). Examination of p-S6 in the co-IP revealed that it was indeed associated with $RPL22^{HA}$ after injury in motor axons. Furthermore, we also found an increase in p-S6 association at an early symptomatic time point in $SOD1^{G93A}$

mice, while it was undetectable at the terminal time point. Future studies into the association of p-S6 and other translational proteins may be applied to reveal how the process of translation itself is altered in injury and disease. In line with this, the idea that ribosomal complexes are not homogeneous has given rise to the idea of a “ribocode” in which specification of ribosomes may tune them to translate specific mRNAs under different contexts (Xue and Barna, 2012; Holt and Schuman, 2013). Therefore, examining the proteins that associate with the $RPL22^{HA}$ IP in different conditions may reveal new levels of regulation that are necessary for motor neuron survival and regeneration.

Concluding Thoughts

Through the work presented here we highlighted just some of the molecular mechanisms that regulate motor neuron innervation at the NMJ. Our examination of Sema3A signaling suggests that it has more limited therapeutic potential than previous studies suggested. Additionally, the development of a model to quantitatively assess NMJ reinnervation and a method to assess motor neuron specific gene expression will be valuable tools for future research. Applying these methods to better understand how motor neurons respond to injury and neurodegeneration could lead to promising therapeutic strategies to combat peripheral nerve injuries and neurodegeneration.

REFERENCES

Acevedo-Arozena A, Kalmar B, Essa S, Ricketts T, Joyce P, Kent R, Rowe C, Parker A, Gray A, Hafezparast M, Thorpe JR, Greensmith L, Fisher EM (2011) A comprehensive assessment of the SOD1G93A low-copy transgenic mouse, which models human amyotrophic lateral sclerosis. Dis Model Mech 4:686-700.

Agbulut O, Noirez P, Beaumont F, Butler-Browne G (2003) Myosin heavy chain isoforms in postnatal muscle development of mice. Biology of the Cell 95:399-406.

Apel PJ, Ma J, Callahan M, Northam CN, Alton TB, Sonntag WE, Li Z (2010) Effect of locally delivered IGF-1 on nerve regeneration during aging: an experimental study in rats. Muscle Nerve 41:335-341.

Ara J, Bannerman P, Hahn A, Ramirez S, Pleasure D (2004) Modulation of sciatic nerve expression of class 3 semaphorins by nerve injury. Neurochemical research 29:1153-1159.

Arber S, Han B, Mendelsohn M, Smith M, Jessell TM, Sockanathan S (1999) Requirement for the homeobox gene Hb9 in the consolidation of motor neuron identity. Neuron 23:659-674.

Armstrong DM, Brady R, Hersh LB, Hayes RC, Wiley RG (1991) Expression of choline acetyltransferase and nerve growth factor receptor within hypoglossal motoneurons following nerve injury. The Journal of comparative neurology 304:596-607.

Arthur-Farraj PJ, Latouche M, Wilton DK, Quintes S, Chabrol E, Banerjee A, Woodhoo A, Jenkins B, Rahman M, Turmaine M, Wicher GK, Mitter R, Greensmith L, Behrens A, Raivich G, Mirsky R, Jessen KR (2012) c-Jun reprograms Schwann cells of injured nerves to generate a repair cell essential for regeneration. Neuron 75:633-647.

Bagri A, Cheng HJ, Yaron A, Pleasure SJ, Tessier-Lavigne M (2003) Stereotyped pruning of long hippocampal axon branches triggered by retraction inducers of the semaphorin family. Cell 113:285-299.

Balice-Gordon RJ, Thompson WJ (1988) The organization and development of compartmentalized innervation in rat extensor digitorum longus muscle. The Journal of physiology 398:211-231.

Balice-Gordon RJ, Lichtman JW (1990) In vivo visualization of the growth of pre- and postsynaptic elements of neuromuscular junctions in the mouse. J Neurosci 10:894-908.

Balice-Gordon RJ, Lichtman JW (1993) In vivo observations of pre- and postsynaptic changes during the transition from multiple to single innervation at developing neuromuscular junctions. J Neurosci 13:834-855.

Barik A, Li L, Sathyamurthy A, Xiong WC, Mei L (2016) Schwann Cells in Neuromuscular Junction Formation and Maintenance. J Neurosci 36:9770-9781.
Barik A, Lu Y, Sathyamurthy A, Bowman A, Shen C, Li L, Xiong WC, Mei L (2014) LRP4 is critical for neuromuscular junction maintenance. J Neurosci 34:13892-13905.
Bauder AR, Ferguson TA (2012) Reproducible mouse sciatic nerve crush and subsequent assessment of regeneration by whole mount muscle analysis. J Vis Exp.
Behar O, Golden JA, Mashimo H, Schoen FJ, Fishman MC (1996) Semaphorin III is needed for normal patterning and growth of nerves, bones and heart. Nature 383:525-528.
Bonanomi D, Pfaff SL (2010) Motor axon pathfinding. Cold Spring Harb Perspect Biol 2:a001735.
Bowen DC, Park JS, Bodine S, Stark JL, Valenzuela DM, Stitt TN, Yancopoulos GD, Lindsay RM, Glass DJ, DiStefano PS (1998) Localization and regulation of MuSK at the neuromuscular junction. Dev Biol 199:309-319.
Bozzoni V, Pansarasa O, Diamanti L, Nosari G, Cereda C, Ceroni M (2016) Amyotrophic lateral sclerosis and environmental factors. Functional neurology 31:7-19.
Briese M, Saal L, Appenzeller S, Moradi M, Baluapuri A, Sendtner M (2016) Whole transcriptome profiling reveals the RNA content of motor axons. Nucleic Acids Res 44:e33.
Brill MS, Kleele T, Ruschkies L, Wang M, Marahori NA, Reuter MS, Hausrat TJ, Weigand E, Fisher M, Ahles A, Engelhardt S, Bishop DL, Kneussel M, Misgeld T (2016) Branch-Specific Microtubule Destabilization Mediates Axon Branch Loss during Neuromuscular Synapse Elimination. Neuron 92:845-856.
Brown MC, Jansen JK, Van Essen D (1976) Polyneuronal innervation of skeletal muscle in new-born rats and its elimination during maturation. The Journal of physiology 261:387-422.
Burden SJ, Yumoto N, Zhang W (2013) The role of MuSK in synapse formation and neuromuscular disease. Cold Spring Harb Perspect Biol 5:a009167.
Burnett MG, Zager EL (2004) Pathophysiology of peripheral nerve injury: a brief review. Neurosurgical focus 16:E1.
Caldeira V, Dougherty KJ, Borgius L, Kiehn O (2017) Spinal Hb9::Cre-derived excitatory interneurons contribute to rhythm generation in the mouse. Sci Rep 7:41369.
Campbell DS, Holt CE (2001) Chemotropic responses of retinal growth cones mediated by rapid local protein synthesis and degradation. Neuron 32:1013-1026.
Cheadle L, Biederer T (2014) Activity-dependent regulation of dendritic complexity by semaphorin 3A through Farp1. J Neurosci 34:7999-8009.
Chen X, Zhang J, Wang X, Bi J (2016) Functional recovery from sciatic nerve crush injury is delayed because of increased distal atrophy in mice lacking the p75 receptor. Neuroreport 27:940-947.
Chong MS, Fitzgerald M, Winter J, Hu-Tsai M, Emson PC, Wiese U, Woolf CJ (1992) GAP-43 mRNA in Rat Spinal Cord and Dorsal Root Ganglia Neurons: Developmental Changes and Re-expression Following Peripheral Nerve Injury. Eur J Neurosci 4:883-895.

Christ B, Brand-Saberi B (2002) Limb muscle development. The International journal of developmental biology 46:905-914.
Dadon-Nachum M, Melamed E, Offen D (2011) The "dying-back" phenomenon of motor neurons in ALS. Journal of molecular neuroscience : MN 43:470-477.
Dalkin W, Taetzsch T, Valdez G (2016) The Fibular Nerve Injury Method: A Reliable Assay to Identify and Test Factors That Repair Neuromuscular Junctions. J Vis Exp.
Dasen JS, Liu JP, Jessell TM (2003) Motor neuron columnar fate imposed by sequential phases of Hox-c activity. Nature 425:926-933.
Dasen JS, De Camilli A, Wang B, Tucker PW, Jessell TM (2008) Hox repertoires for motor neuron diversity and connectivity gated by a single accessory factor, FoxP1. Cell 134:304-316.
De Winter F, Vo T, Stam FJ, Wisman LA, Bar PR, Niclou SP, van Muiswinkel FL, Verhaagen J (2006) The expression of the chemorepellent Semaphorin 3A is selectively induced in terminal Schwann cells of a subset of neuromuscular synapses that display limited anatomical plasticity and enhanced vulnerability in motor neuron disease. Mol Cell Neurosci 32:102-117.
Deglincerti A, Jaffrey SR (2012) Insights into the roles of local translation from the axonal transcriptome. Open Biol 2:120079.
Dent EW, Barnes AM, Tang F, Kalil K (2004) Netrin-1 and semaphorin 3A promote or inhibit cortical axon branching, respectively, by reorganization of the cytoskeleton. J Neurosci 24:3002-3012.
Dillon AK, Fujita SC, Matise MP, Jarjour AA, Kennedy TE, Kollmus H, Arnold HH, Weiner JA, Sanes JR, Kaprielian Z (2005) Molecular control of spinal accessory motor neuron/axon development in the mouse spinal cord. J Neurosci 25:10119-10130.
Dobrowolny G, Giacinti C, Pelosi L, Nicoletti C, Winn N, Barberi L, Molinaro M, Rosenthal N, Musaro A (2005) Muscle expression of a local Igf-1 isoform protects motor neurons in an ALS mouse model. J Cell Biol 168:193-199.
Droppelmann CA, Campos-Melo D, Ishtiaq M, Volkening K, Strong MJ (2014) RNA metabolism in ALS: when normal processes become pathological. Amyotroph Lateral Scler Frontotemporal Degener 15:321-336.
Duchen LW (1970) Changes in motor innervation and cholinesterase localization induced by botulinum toxin in skeletal muscle of the mouse: differences between fast and slow muscles. Journal of neurology, neurosurgery, and psychiatry 33:40-54.
Dufner A, Thomas G (1999) Ribosomal S6 kinase signaling and the control of translation. Experimental cell research 253:100-109.
Fallini C, Donlin-Asp PG, Rouanet JP, Bassell GJ, Rossoll W (2016) Deficiency of the Survival of Motor Neuron Protein Impairs mRNA Localization and Local Translation in the Growth Cone of Motor Neurons. J Neurosci 36:3811-3820.
Feinstein B, Lindegard B, Nyman E, Wohlfart G (1955) Morphologic studies of motor units in normal human muscles. Acta anatomica 23:127-142.
Figley MD, Bieri G, Kolaitis RM, Taylor JP, Gitler AD (2014) Profilin 1 associates with stress granules and ALS-linked mutations alter stress granule dynamics. J Neurosci 34:8083-8097.

Fiore R, Puschel AW (2003) The function of semaphorins during nervous system development. Frontiers in bioscience : a journal and virtual library 8:s484-499.
Frey D, Schneider C, Xu L, Borg J, Spooren W, Caroni P (2000) Early and selective loss of neuromuscular synapse subtypes with low sprouting competence in motoneuron diseases. J Neurosci 20:2534-2542.
Friese A, Kaltschmidt JA, Ladle DR, Sigrist M, Jessell TM, Arber S (2009) Gamma and alpha motor neurons distinguished by expression of transcription factor Err3. Proceedings of the National Academy of Sciences of the United States of America 106:13588-13593.
Fujisawa H, Kitsukawa T, Kawakami A, Takagi S, Shimizu M, Hirata T (1997) Roles of a neuronal cell-surface molecule, neuropilin, in nerve fiber fasciculation and guidance. Cell and tissue research 290:465-470.
Gallarda BW, Bonanomi D, Muller D, Brown A, Alaynick WA, Andrews SE, Lemke G, Pfaff SL, Marquardt T (2008) Segregation of axial motor and sensory pathways via heterotypic trans-axonal signaling. Science (New York, NY) 320:233-236.
Gaudet AD, Popovich PG, Ramer MS (2011) Wallerian degeneration: gaining perspective on inflammatory events after peripheral nerve injury. J Neuroinflammation 8:110.
Giger RJ, Hollis ER, 2nd, Tuszynski MH (2010) Guidance molecules in axon regeneration. Cold Spring Harb Perspect Biol 2:a001867.
Gonzalez C, Canovas J, Fresno J, Couve E, Court FA, Couve A (2016) Axons provide the secretory machinery for trafficking of voltage-gated sodium channels in peripheral nerve. Proceedings of the National Academy of Sciences of the United States of America 113:1823-1828.
Griffin JW, Thompson WJ (2008) Biology and pathology of nonmyelinating Schwann cells. Glia 56:1518-1531.
Grinsell D, Keating CP (2014) Peripheral nerve reconstruction after injury: a review of clinical and experimental therapies. Biomed Res Int 2014:698256.
Gu C, Rodriguez ER, Reimert DV, Shu T, Fritzsch B, Richards LJ, Kolodkin AL, Ginty DD (2003) Neuropilin-1 conveys semaphorin and VEGF signaling during neural and cardiovascular development. Developmental cell 5:45-57.
Gupta SK, Poduslo JF, Mezei C (1988) Temporal changes in PO and MBP gene expression after crush-injury of the adult peripheral nerve. Brain research 464:133-141.
Hayes RC, Wiley RG, Armstrong DM (1992) Induction of nerve growth factor receptor (p75NGFr) mRNA within hypoglossal motoneurons following axonal injury. Brain research Molecular brain research 15:291-297.
He Z, Tessier-Lavigne M (1997) Neuropilin is a receptor for the axonal chemorepellent Semaphorin III. Cell 90:739-751.
Hegedus J, Putman CT, Gordon T (2007) Time course of preferential motor unit loss in the SOD1 G93A mouse model of amyotrophic lateral sclerosis. Neurobiol Dis 28:154-164.
Heiman M, Schaefer A, Gong S, Peterson JD, Day M, Ramsey KE, Suarez-Farinas M, Schwarz C, Stephan DA, Surmeier DJ, Greengard P, Heintz N (2008) A translational profiling approach for the molecular characterization of CNS cell types. Cell 135:738-748.

Helmbrecht MS, Soellner H, Truckenbrodt AM, Sundermeier J, Cohrs C, Hans W, de Angelis MH, Feuchtinger A, Aichler M, Fouad K, Huber AB (2015) Loss of Npn1 from motor neurons causes postnatal deficits independent from Sema3A signaling. Dev Biol 399:2-14.
Hinckley CA, Hartley R, Wu L, Todd A, Ziskind-Conhaim L (2005) Locomotor-like rhythms in a genetically distinct cluster of interneurons in the mammalian spinal cord. J Neurophysiol 93:1439-1449.
Holt CE, Schuman EM (2013) The central dogma decentralized: new perspectives on RNA function and local translation in neurons. Neuron 80:648-657.
Huber AB, Kania A, Tran TS, Gu C, De Marco Garcia N, Lieberam I, Johnson D, Jessell TM, Ginty DD, Kolodkin AL (2005) Distinct roles for secreted semaphorin signaling in spinal motor axon guidance. Neuron 48:949-964.
Hulliger M (1984) The mammalian muscle spindle and its central control. Reviews of physiology, biochemistry and pharmacology 101:1-110.
Humphreys BD, DiRocco DP (2014) Lineage-tracing methods and the kidney. Kidney international 86:481-488.
Ikeda K, Klinkosz B, Greene T, Cedarbaum JM, Wong V, Lindsay RM, Mitsumoto H (1995) Effects of brain-derived neurotrophic factor on motor dysfunction in wobbler mouse motor neuron disease. Ann Neurol 37:505-511.
Ikeda O, Murakami M, Ino H, Yamazaki M, Nemoto T, Koda M, Nakayama C, Moriya H (2001) Acute up-regulation of brain-derived neurotrophic factor expression resulting from experimentally induced injury in the rat spinal cord. Acta neuropathologica 102:239-245.
Islamov RR, Chintalgattu V, Pak ES, Katwa LC, Murashov AK (2004) Induction of VEGF and its Flt-1 receptor after sciatic nerve crush injury. Neuroreport 15:2117-2121.
Janssen BJ, Malinauskas T, Weir GA, Cader MZ, Siebold C, Jones EY (2012) Neuropilins lock secreted semaphorins onto plexins in a ternary signaling complex. Nat Struct Mol Biol 19:1293-1299.
Jespersen NZ, Larsen TJ, Peijs L, Daugaard S, Homoe P, Loft A, de Jong J, Mathur N, Cannon B, Nedergaard J, Pedersen BK, Moller K, Scheele C (2013) A classical brown adipose tissue mRNA signature partly overlaps with brite in the supraclavicular region of adult humans. Cell Metab 17:798-805.
Jing L, Lefebvre JL, Gordon LR, Granato M (2009) Wnt signals organize synaptic prepattern and axon guidance through the zebrafish unplugged/MuSK receptor. Neuron 61:721-733.
Johri A, Beal MF (2012) Mitochondrial dysfunction in neurodegenerative diseases. J Pharmacol Exp Ther 342:619-630.
Jung J, Jung H (2016) Methods to analyze cell type-specific gene expression profiles from heterogeneous cell populations. Animal Cells and Systems 20:113-117.
Kahr PC, Piccini I, Fabritz L, Greber B, Scholer H, Scheld HH, Hoffmeier A, Brown NA, Kirchhof P (2011) Systematic analysis of gene expression differences between left and right atria in different mouse strains and in human atrial tissue. PLoS One 6:e26389.
Kalinski AL, Sachdeva R, Gomes C, Lee SJ, Shah Z, Houle JD, Twiss JL (2015) mRNAs and Protein Synthetic Machinery Localize into Regenerating Spinal Cord

Axons When They Are Provided a Substrate That Supports Growth. J Neurosci 35:10357-10370.
Kang H, Lichtman JW (2013) Motor axon regeneration and muscle reinnervation in young adult and aged animals. J Neurosci 33:19480-19491.
Kang H, Tian L, Thompson W (2003) Terminal Schwann cells guide the reinnervation of muscle after nerve injury. Journal of neurocytology 32:975-985.
Kania A, Jessell TM (2003) Topographic motor projections in the limb imposed by LIM homeodomain protein regulation of ephrin-A:EphA interactions. Neuron 38:581-596.
Kania A, Johnson RL, Jessell TM (2000) Coordinate roles for LIM homeobox genes in directing the dorsoventral trajectory of motor axons in the vertebrate limb. Cell 102:161-173.
Kanning KC, Kaplan A, Henderson CE (2010) Motor neuron diversity in development and disease. Annu Rev Neurosci 33:409-440.
Kaplan A, Spiller KJ, Towne C, Kanning KC, Choe GT, Geber A, Akay T, Aebischer P, Henderson CE (2014) Neuronal matrix metalloproteinase-9 is a determinant of selective neurodegeneration. Neuron 81:333-348.
Kar AN, Lee SJ, Twiss JL (2017) Expanding Axonal Transcriptome Brings New Functions for Axonally Synthesized Proteins in Health and Disease. Neuroscientist:1073858417712668.
Kaspar BK, Llado J, Sherkat N, Rothstein JD, Gage FH (2003) Retrograde viral delivery of IGF-1 prolongs survival in a mouse ALS model. Science (New York, NY) 301:839-842.
Kawabuchi M, Tan H, Wang S (2011) Age affects reciprocal cellular interactions in neuromuscular synapses following peripheral nerve injury. Ageing Res Rev 10:43-53.
Kennedy JM, Zochodne DW (2000) The regenerative deficit of peripheral nerves in experimental diabetes: its extent, timing and possible mechanisms. Brain : a journal of neurology 123 (Pt 10):2118-2129.
Kim N, Burden SJ (2008) MuSK controls where motor axons grow and form synapses. Nature neuroscience 11:19-27.
Kim N, Stiegler AL, Cameron TO, Hallock PT, Gomez AM, Huang JH, Hubbard SR, Dustin ML, Burden SJ (2008) Lrp4 is a receptor for Agrin and forms a complex with MuSK. Cell 135:334-342.
Kitsukawa T, Shimizu M, Sanbo M, Hirata T, Taniguchi M, Bekku Y, Yagi T, Fujisawa H (1997) Neuropilin-semaphorin III/D-mediated chemorepulsive signals play a crucial role in peripheral nerve projection in mice. Neuron 19:995-1005.
Kolodkin AL, Levengood DV, Rowe EG, Tai YT, Giger RJ, Ginty DD (1997) Neuropilin is a semaphorin III receptor. Cell 90:753-762.
Kramer ER, Knott L, Su F, Dessaud E, Krull CE, Helmbacher F, Klein R (2006) Cooperation between GDNF/Ret and ephrinA/EphA4 signals for motor-axon pathway selection in the limb. Neuron 50:35-47.
Lallemend F, Ernfors P (2012) Molecular interactions underlying the specification of sensory neurons. Trends Neurosci 35:373-381.

Lance-Jones C, Landmesser L (1980) Motoneurone projection patterns in embryonic chick limbs following partial deletions of the spinal cord. The Journal of physiology 302:559-580.
Lappe-Siefke C, Goebbels S, Gravel M, Nicksch E, Lee J, Braun PE, Griffiths IR, Nave KA (2003) Disruption of Cnp1 uncouples oligodendroglial functions in axonal support and myelination. Nat Genet 33:366-374.
Li FQ, Fowler KA, Neil JE, Colton CA, Vitek MP (2010) An apolipoprotein E-mimetic stimulates axonal regeneration and remyelination after peripheral nerve injury. J Pharmacol Exp Ther 334:106-115.
Lichtman JW, Magrassi L, Purves D (1987) Visualization of neuromuscular junctions over periods of several months in living mice. J Neurosci 7:1215-1222.
Lieberam I, Agalliu D, Nagasawa T, Ericson J, Jessell TM (2005) A Cxcl12-CXCR4 chemokine signaling pathway defines the initial trajectory of mammalian motor axons. Neuron 47:667-679.
Loring RH, Salpeter MM (1980) Denervation increases turnover rate of junctional acetylcholine receptors. Proceedings of the National Academy of Sciences of the United States of America 77:2293-2297.
Lowrie MB, Krishnan S, Vrbova G (1982) Recovery of slow and fast muscles following nerve injury during early post-natal development in the rat. The Journal of physiology 331:51-66.
Luo Y, Raible D, Raper JA (1993) Collapsin: a protein in brain that induces the collapse and paralysis of neuronal growth cones. Cell 75:217-227.
Luria V, Krawchuk D, Jessell TM, Laufer E, Kania A (2008) Specification of motor axon trajectory by ephrin-B:EphB signaling: symmetrical control of axonal patterning in the developing limb. Neuron 60:1039-1053.
Ma CH, Omura T, Cobos EJ, Latremoliere A, Ghasemlou N, Brenner GJ, van Veen E, Barrett L, Sawada T, Gao F, Coppola G, Gertler F, Costigan M, Geschwind D, Woolf CJ (2011) Accelerating axonal growth promotes motor recovery after peripheral nerve injury in mice. J Clin Invest 121:4332-4347.
MacIntosh BR, Gardiner PF, McComas AJ (2006) Skeletal muscle: form and function: Human Kinetics.
Mackenzie IR, Bigio EH, Ince PG, Geser F, Neumann M, Cairns NJ, Kwong LK, Forman MS, Ravits J, Stewart H, Eisen A, McClusky L, Kretzschmar HA, Monoranu CM, Highley JR, Kirby J, Siddique T, Shaw PJ, Lee VM, Trojanowski JQ (2007) Pathological TDP-43 distinguishes sporadic amyotrophic lateral sclerosis from amyotrophic lateral sclerosis with SOD1 mutations. Ann Neurol 61:427-434.
Magill CK, Tong A, Kawamura D, Hayashi A, Hunter DA, Parsadanian A, Mackinnon SE, Myckatyn TM (2007) Reinnervation of the tibialis anterior following sciatic nerve crush injury: a confocal microscopic study in transgenic mice. Exp Neurol 207:64-74.
Magill CK, Moore AM, Yan Y, Tong AY, MacEwan MR, Yee A, Hayashi A, Hunter DA, Ray WZ, Johnson PJ, Parsadanian A, Myckatyn TM, Mackinnon SE (2010) The differential effects of pathway- versus target-derived glial cell line-derived neurotrophic factor on peripheral nerve regeneration. J Neurosurg 113:102-109.

Martinez-Pena y Valenzuela I, Mouslim C, Pires-Oliveira M, Adams ME, Froehner SC, Akaaboune M (2011) Nicotinic acetylcholine receptor stability at the NMJ deficient in alpha-syntrophin in vivo. J Neurosci 31:15586-15596.
Martinez-Pena YVI, Aittaleb M, Chen PJ, Akaaboune M (2015) The knockdown of alphakap alters the postsynaptic apparatus of neuromuscular junctions in living mice. J Neurosci 35:5118-5127.
Masahira N, Takebayashi H, Ono K, Watanabe K, Ding L, Furusho M, Ogawa Y, Nabeshima Y, Alvarez-Buylla A, Shimizu K, Ikenaka K (2006) Olig2-positive progenitors in the embryonic spinal cord give rise not only to motoneurons and oligodendrocytes, but also to a subset of astrocytes and ependymal cells. Dev Biol 293:358-369.
Maximino JR, de Oliveira GP, Alves CJ, Chadi G (2014) Deregulated expression of cytoskeleton related genes in the spinal cord and sciatic nerve of presymptomatic SOD1(G93A) Amyotrophic Lateral Sclerosis mouse model. Front Cell Neurosci 8:148.
Meeker R, Williams K (2014) Dynamic nature of the p75 neurotrophin receptor in response to injury and disease. J Neuroimmune Pharmacol 9:615-628.
Merkulyeva N, Veshchitskii A, Makarov F, Gerasimenko Y, Musienko P (2015) Distribution of 28 kDa Calbindin-Immunopositive Neurons in the Cat Spinal Cord. Front Neuroanat 9:166.
Messersmith EK, Leonardo ED, Shatz CJ, Tessier-Lavigne M, Goodman CS, Kolodkin AL (1995) Semaphorin III can function as a selective chemorepellent to pattern sensory projections in the spinal cord. Neuron 14:949-959.
Misawa H, Nakata K, Toda K, Matsuura J, Oda Y, Inoue H, Tateno M, Takahashi R (2003) VAChT-Cre. Fast and VAChT-Cre.Slow: postnatal expression of Cre recombinase in somatomotor neurons with different onset. Genesis 37:44-50.
Mitchell LS, Griffiths IR, Morrison S, Barrie JA, Kirkham D, McPhilemy K (1990) Expression of myelin protein gene transcripts by Schwann cells of regenerating nerve. Journal of neuroscience research 27:125-135.
Molofsky AV, Kelley KW, Tsai HH, Redmond SA, Chang SM, Madireddy L, Chan JR, Baranzini SE, Ullian EM, Rowitch DH (2014) Astrocyte-encoded positional cues maintain sensorimotor circuit integrity. Nature 509:189-194.
Moloney EB, de Winter F, Verhaagen J (2014) ALS as a distal axonopathy: molecular mechanisms affecting neuromuscular junction stability in the presymptomatic stages of the disease. Front Neurosci 8:252.
Moloney EB, Hobo B, De Winter F, Verhaagen J (2017) Expression of a Mutant SEMA3A Protein with Diminished Signalling Capacity Does Not Alter ALS-Related Motor Decline, or Confer Changes in NMJ Plasticity after BotoxA-Induced Paralysis of Male Gastrocnemic Muscle. PLoS One 12:e0170314.
Nagata Y, Okuya M, Watanabe R, Honda M (1982) Regional distribution of cholinergic neurons in human spinal cord transections in the patients with and without motor neuron disease. Brain research 244:223-229.
Nakamura F, Goshima Y (2002) Structural and functional relation of neuropilins. Advances in experimental medicine and biology 515:55-69.

Ngo ST, Steyn FJ (2015) The interplay between metabolic homeostasis and neurodegeneration: insights into the neurometabolic nature of amyotrophic lateral sclerosis. Cell Regen (Lond) 4:5.
Nitkin RM, Smith MA, Magill C, Fallon JR, Yao YM, Wallace BG, McMahan UJ (1987) Identification of agrin, a synaptic organizing protein from Torpedo electric organ. J Cell Biol 105:2471-2478.
Novitch BG, Chen AI, Jessell TM (2001) Coordinate regulation of motor neuron subtype identity and pan-neuronal properties by the bHLH repressor Olig2. Neuron 31:773-789.
Raven JF, Koromilas AE (2008) PERK and PKR: old kinases learn new tricks. Cell Cycle 7:1146-1150.
Renton AE, Chio A, Traynor BJ (2014) State of play in amyotrophic lateral sclerosis genetics. Nature neuroscience 17:17-23.
Reynolds ML, Woolf CJ (1992) Terminal Schwann cells elaborate extensive processes following denervation of the motor endplate. Journal of neurocytology 21:50-66.
Rossi J, Balthasar N, Olson D, Scott M, Berglund E, Lee CE, Choi MJ, Lauzon D, Lowell BB, Elmquist JK (2011) Melanocortin-4 receptors expressed by cholinergic neurons regulate energy balance and glucose homeostasis. Cell Metab 13:195-204.
Saito S, Kidd GJ, Trapp BD, Dawson TM, Bredt DS, Wilson DA, Traystman RJ, Snyder SH, Hanley DF (1994) Rat spinal cord neurons contain nitric oxide synthase. Neuroscience 59:447-456.
Sakuma M, Gorski G, Sheu SH, Lee S, Barrett LB, Singh B, Omura T, Latremoliere A, Woolf CJ (2016) Lack of motor recovery after prolonged denervation of the neuromuscular junction is not due to regenerative failure. Eur J Neurosci 43:451-462.
Saller MM, Huettl RE, Hanuschick P, Amend AL, Alberton P, Aszodi A, Huber AB (2016) The role of Sema3-Npn-1 signaling during diaphragm innervation and muscle development. J Cell Sci 129:3295-3308.
Sanes JR, Lichtman JW (1999) Development of the vertebrate neuromuscular junction. Annu Rev Neurosci 22:389-442.
Sanes JR, Lichtman JW (2001) Induction, assembly, maturation and maintenance of a postsynaptic apparatus. Nature reviews Neuroscience 2:791-805.
Sanz E, Yang L, Su T, Morris DR, McKnight GS, Amieux PS (2009) Cell-type-specific isolation of ribosome-associated mRNA from complex tissues. Proceedings of the National Academy of Sciences of the United States of America 106:13939-13944.
Sas K, Robotka H, Toldi J, Vecsei L (2007) Mitochondria, metabolic disturbances, oxidative stress and the kynurenine system, with focus on neurodegenerative disorders. J Neurol Sci 257:221-239.
Scarlato M (2003) Induction of neuropilins-1 and -2 and their ligands, Sema3A, Sema3F, and VEGF, during Wallerian degeneration in the peripheral nervous system. Experimental Neurology 183:489-498.
Schmidt ER, Pasterkamp RJ, van den Berg LH (2009) Axon guidance proteins: novel therapeutic targets for ALS? Prog Neurobiol 88:286-301.

Sharma K, Sheng HZ, Lettieri K, Li H, Karavanov A, Potter S, Westphal H, Pfaff SL (1998) LIM homeodomain factors Lhx3 and Lhx4 assign subtype identities for motor neurons. Cell 95:817-828.
Shelly M, Cancedda L, Lim BK, Popescu AT, Cheng PL, Gao H, Poo MM (2011) Semaphorin3A regulates neuronal polarization by suppressing axon formation and promoting dendrite growth. Neuron 71:433-446.
Shigeoka T, Jung H, Jung J, Turner-Bridger B, Ohk J, Lin JQ, Amieux PS, Holt CE (2016) Dynamic Axonal Translation in Developing and Mature Visual Circuits. Cell 166:181-192.
Shirasaki R, Pfaff SL (2002) Transcriptional codes and the control of neuronal identity. Annu Rev Neurosci 25:251-281.
Shirasaki R, Lewcock JW, Lettieri K, Pfaff SL (2006) FGF as a target-derived chemoattractant for developing motor axons genetically programmed by the LIM code. Neuron 50:841-853.
Smith IW, Mikesh M, Lee Y, Thompson WJ (2013) Terminal Schwann cells participate in the competition underlying neuromuscular synapse elimination. J Neurosci 33:17724-17736.
Soker S, Takashima S, Miao HQ, Neufeld G, Klagsbrun M (1998) Neuropilin-1 is expressed by endothelial and tumor cells as an isoform-specific receptor for vascular endothelial growth factor. Cell 92:735-745.
Steward O, Levy WB (1982) Preferential localization of polyribosomes under the base of dendritic spines in granule cells of the dentate gyrus. J Neurosci 2:284-291.
Stifani N (2014) Motor neurons and the generation of spinal motor neuron diversity. Front Cell Neurosci 8:293.
Storkebaum E et al. (2005) Treatment of motoneuron degeneration by intracerebroventricular delivery of VEGF in a rat model of ALS. Nature neuroscience 8:85-92.
Sugiura Y, Lin W (2011) Neuron-glia interactions: the roles of Schwann cells in neuromuscular synapse formation and function. Biosci Rep 31:295-302.
Sun S, Sun Y, Ling SC, Ferraiuolo L, McAlonis-Downes M, Zou Y, Drenner K, Wang Y, Ditsworth D, Tokunaga S, Kopelevich A, Kaspar BK, Lagier-Tourenne C, Cleveland DW (2015) Translational profiling identifies a cascade of damage initiated in motor neurons and spreading to glia in mutant SOD1-mediated ALS. Proceedings of the National Academy of Sciences of the United States of America 112:E6993-7002.
Sutton MA, Schuman EM (2006) Dendritic protein synthesis, synaptic plasticity, and memory. Cell 127:49-58.
Takahashi T, Fournier A, Nakamura F, Wang LH, Murakami Y, Kalb RG, Fujisawa H, Strittmatter SM (1999) Plexin-neuropilin-1 complexes form functional semaphorin-3A receptors. Cell 99:59-69.
Tanabe Y, William C, Jessell TM (1998) Specification of motor neuron identity by the MNR2 homeodomain protein. Cell 95:67-80.
Taniguchi M, Yuasa S, Fujisawa H, Naruse I, Saga S, Mishina M, Yagi T (1997) Disruption of semaphorin III/D gene causes severe abnormality in peripheral nerve projection. Neuron 19:519-530.

Tapia JC, Wylie JD, Kasthuri N, Hayworth KJ, Schalek R, Berger DR, Guatimosim C, Seung HS, Lichtman JW (2012) Pervasive synaptic branch removal in the mammalian neuromuscular system at birth. Neuron 74:816-829.
Tatsumi R, Sankoda Y, Anderson JE, Sato Y, Mizunoya W, Shimizu N, Suzuki T, Yamada M, Rhoads RP, Jr., Ikeuchi Y, Allen RE (2009) Possible implication of satellite cells in regenerative motoneuritogenesis: HGF upregulates neural chemorepellent Sema3A during myogenic differentiation. Am J Physiol Cell Physiol 297:C238-252.
Tomas J, Garcia N, Lanuza MA, Santafe MM, Tomas M, Nadal L, Hurtado E, Simo A, Cilleros V (2017) Presynaptic Membrane Receptors Modulate ACh Release, Axonal Competition and Synapse Elimination during Neuromuscular Junction Development. Front Mol Neurosci 10:132.
Tsuchida T, Ensini M, Morton SB, Baldassare M, Edlund T, Jessell TM, Pfaff SL (1994) Topographic organization of embryonic motor neurons defined by expression of LIM homeobox genes. Cell 79:957-970.
Twiss JL, Shooter EM (1995) Nerve growth factor promotes neurite regeneration in PC12 cells by translational control. Journal of neurochemistry 64:550-557.
Vallstedt A, Muhr J, Pattyn A, Pierani A, Mendelsohn M, Sander M, Jessell TM, Ericson J (2001) Different levels of repressor activity assign redundant and specific roles to Nkx6 genes in motor neuron and interneuron specification. Neuron 31:743-755.
Van Hoecke A et al. (2012) EPHA4 is a disease modifier of amyotrophic lateral sclerosis in animal models and in humans. Nat Med 18:1418-1422.
Venkova K, Christov A, Kamaluddin Z, Kobalka P, Siddiqui S, Hensley K (2014) Semaphorin 3A signaling through neuropilin-1 is an early trigger for distal axonopathy in the SOD1G93A mouse model of amyotrophic lateral sclerosis. Journal of neuropathology and experimental neurology 73:702-713.
Verma P, Chierzi S, Codd AM, Campbell DS, Meyer RL, Holt CE, Fawcett JW (2005) Axonal protein synthesis and degradation are necessary for efficient growth cone regeneration. J Neurosci 25:331-342.
Wang H, Yang H, Shivalila CS, Dawlaty MM, Cheng AW, Zhang F, Jaenisch R (2013) One-step generation of mice carrying mutations in multiple genes by CRISPR/Cas-mediated genome engineering. Cell 153:910-918.
Weatherbee SD, Anderson KV, Niswander LA (2006) LDL-receptor-related protein 4 is crucial for formation of the neuromuscular junction. Development 133:4993-5000.
Williamson TL, Cleveland DW (1999) Slowing of axonal transport is a very early event in the toxicity of ALS-linked SOD1 mutants to motor neurons. Nature neuroscience 2:50-56.
Willis DE, Twiss JL (2006) The evolving roles of axonally synthesized proteins in regeneration. Curr Opin Neurobiol 16:111-118.
Willis DE, Twiss JL (2010) Regulation of protein levels in subcellular domains through mRNA transport and localized translation. Molecular & cellular proteomics : MCP 9:952-962.
Wu CH et al. (2012) Mutations in the profilin 1 gene cause familial amyotrophic lateral sclerosis. Nature 488:499-503.

Wu KY, Hengst U, Cox LJ, Macosko EZ, Jeromin A, Urquhart ER, Jaffrey SR (2005) Local translation of RhoA regulates growth cone collapse. Nature 436:1020-1024.
Xu QG, Midha R, Martinez JA, Guo GF, Zochodne DW (2008) Facilitated sprouting in a peripheral nerve injury. Neuroscience 152:877-887.
Xue S, Barna M (2012) Specialized ribosomes: a new frontier in gene regulation and organismal biology. Nat Rev Mol Cell Biol 13:355-369.
Yao J, Sasaki Y, Wen Z, Bassell GJ, Zheng JQ (2006) An essential role for beta-actin mRNA localization and translation in Ca2+-dependent growth cone guidance. Nature neuroscience 9:1265-1273.
Yao M, Moir MS, Wang MZ, To MP, Terris DJ (1999) Peripheral nerve regeneration in CNTF knockout mice. The Laryngoscope 109:1263-1268.
Yaron A, Zheng B (2007) Navigating their way to the clinic: emerging roles for axon guidance molecules in neurological disorders and injury. Dev Neurobiol 67:1216-1231.
Yaron A, Huang PH, Cheng HJ, Tessier-Lavigne M (2005) Differential requirement for Plexin-A3 and -A4 in mediating responses of sensory and sympathetic neurons to distinct class 3 Semaphorins. Neuron 45:513-523.
Yasuda K, Mili S (2016) Dysregulated axonal RNA translation in amyotrophic lateral sclerosis. Wiley Interdiscip Rev RNA 7:589-603.
Yasuda K, Zhang H, Loiselle D, Haystead T, Macara IG, Mili S (2013) The RNA-binding protein Fus directs translation of localized mRNAs in APC-RNP granules. J Cell Biol 203:737-746.
Yumoto N, Kim N, Burden SJ (2012) Lrp4 is a retrograde signal for presynaptic differentiation at neuromuscular synapses. Nature 489:438-442.
Zagoraiou L, Akay T, Martin JF, Brownstone RM, Jessell TM, Miles GB (2009) A cluster of cholinergic premotor interneurons modulates mouse locomotor activity. Neuron 64:645-662.
Zheng C, Skold MK, Li J, Nennesmo I, Fadeel B, Henter JI (2007) VEGF reduces astrogliosis and preserves neuromuscular junctions in ALS transgenic mice. Biochemical and biophysical research communications 363:989-993.
Zheng J, Sun J, Lu X, Zhao P, Li K, Li L (2016) BDNF promotes the axonal regrowth after sciatic nerve crush through intrinsic neuronal capability upregulation and distal portion protection. Neurosci Lett 621:1-8.